

**Metalloproteins and protein-protein complexes investigated by
CW and pulsed EPR spectroscopy**

Dissertation
zur Erlangung des Doktorgrades
der Naturwissenschaften

vorgelegt beim Fachbereich Chemische und Pharmazeutische Wissenschaften
der Johann Wolfgang Goethe-Universität
in Frankfurt am Main

von
Sevdalina Lyubenova
aus Veliko Tarnovo, Bulgarien

Frankfurt am Main 2006
D30

vom Fachbereich Chemische und Pharmazeutische Wissenschaften
der Johann Wolfgang Goethe-Universität Frankfurt als Dissertation angenommen.

Dekan: Prof. Dr. Harald Schwalbe

Gutachter: Prof. Dr. Thomas Prisner
Prof. Dr. Bernd Ludwig

Datum der Disputation: 27. 06. 2006

На Мама и Мима

Zusammenfassung

Eines der zentralen Forschungsziele in der biophysikalischen Chemie ist die Aufklärung der Struktur und Funktion von Membranproteinen, die in Energieübertragungswegen eine Rolle spielen. Sowohl die aerobe als auch die anaerobe Atmung beinhalten Elektronentransfer und Protonentranslokation durch die mitochondrialen und bakteriellen Membranen. Die Elektronentransferprozesse führen zu Änderungen im Oxidationszustand der beteiligten Kofaktoren, wodurch paramagnetische Spezies entstehen können. Aus diesem Grund ist die elektronenparamagnetische Resonanzspektroskopie (EPR-Spektroskopie) die Methode der Wahl, um Informationen über die elektronische und molekulare Struktur der paramagnetischen Intermediate zu erhalten. Diese strukturellen Informationen sind wiederum direkt verknüpft mit Erkenntnissen über die Funktion der Proteine der Atmungskette.

In dieser Arbeit wurden Multifrequenz-Continuous-Wave- (CW) und Puls-EPR-Spektroskopie verwendet, um die Molybdänbindungsstelle in Polysulfidreduktase (Psr) aus dem anaeroben Bakterium *Wolinella succinogenes* sowie den Protein-Protein-Komplex zwischen Cytochrom *c*-Oxidase (CcO) und Cytochrom *c* aus dem aeroben Bakterium *Paracoccus denitrificans* zu charakterisieren.

Molybdän in Psr

Psr ist ein essentielles Enzym für die Schwefelatmung von *Wolinella succinogenes*. Biochemische Studien deuten darauf hin, dass das aktive Zentrum dieses Enzyms ein mononukleares Molybdänzentrum enthält, das die Reduktion des Polysulfidsubstrats zu Sulfid katalysiert. Da keine Kristallstruktur von Psr existiert, müssen biochemische und spektroskopische Methoden angewandt werden, um strukturelle Informationen über dieses Enzym zu gewinnen. In der vorliegenden Arbeit wurden daher CW- und moderne Puls-EPR-Techniken verwendet, um das katalytisch aktive Zentrum zu untersuchen.

Im ersten Teil dieser Dissertation wurden verschiedene Reduktionsmittel eingesetzt, um paramagnetische Zustände von Psr zu generieren. Anschließend wurde Multifrequenz-EPR-Spektroskopie zur Identifikation der Mo(V)-Spezies verwendet. Mit Hilfe von

Simulationen der experimentellen Spektren konnten – basierend auf Molybdän-Hyperfeinkopplungs- und g-Tensorwerten – drei verschiedene Zustände identifiziert werden. Auf Grund eines Vergleichs dieser EPR-Parameter mit denen verwandter und gut charakterisierter Enzyme konnte gefolgert werden, dass je nach Zustand fünf oder sechs Schwefelliganden an das Molybdänzentrum koordiniert sind. Derjenige Zustand, der durch Zugabe von Polysulfid entsteht, wurde als katalytisch aktive Form vorgeschlagen. In diesem aktiven Zustand sollte als sechster Ligand ein Schwefelatom der Polysulfidkette an das Molybdän gebunden sein. Um die postulierte Nähe des Polysulfids zum Molybdänzentrum über Hyperfeinwechselwirkungen nachzuweisen, wurde ^{33}S -markiertes Polysulfid synthetisiert und als Substrat eingesetzt. Im Anschluss daran wurden 1D-ESEEM- und 2D-HYSCORE-Spektroskopie zur Detektion der ^{33}S -Hyperfein- und ^{33}S -Quadrupolwechselwirkungen verwendet, da diese Wechselwirkungen zu klein waren, um in konventionellen CW-EPR-Spektren beobachtet werden zu können. Bis heute existiert nur eine einzige Puls-EPR-Studie, die ^{33}S -Wechselwirkungen behandelt, da der ^{33}S -Kern einen Kernspin $I = 3/2$, ein großes Kernquadrupolmoment und eine niedrige Larmorfrequenz aufweist. All diese Eigenschaften machen es schwer, ^{33}S zu detektieren und aus den ^{33}S -Spektren strukturelle Informationen zu gewinnen. In dieser Arbeit war es jedoch mittels Analyse der 2D-Daten möglich, den Mo(V)- ^{33}S -Abstand auf einen Bereich von 2 bis 2.5 Å einzugrenzen. Bekannte Mo-S-Abstände für Molybdänenzyme der gleichen Familie liegen zwischen 1.8 und 2.8 Å, was den Schluss nahe legt, dass ^{33}S aus Polysulfid tatsächlich der sechste Ligand des Mo(V)-Zentrums. Damit konnte demonstriert werden, dass Polysulfid das Substrat von Psr ist. Die präsentierte Untersuchung unterstreicht, dass HYSCORE-Experimente eine wirkungsvolle Methode darstellen, um detaillierte Einblicke in die Strukturen von aktiven Zentren von Molybdänenzymen und den Reaktionsweg von Substratomen während der Katalyse zu gewinnen. Dichtefunktionaltheorie-Rechnungen (DFT-Rechnungen) und quantitative numerische Simulationen der 2D-Daten können in diesem Zusammenhang helfen, weitere strukturelle Details über die Molybdänbindungsstelle in Psr aus den experimentellen Daten zu extrahieren.

CcO: Cytochrom c-Komplex

Die Bildung von Protein-Protein-Komplexen ist ein wichtiger Schritt in biologischen Prozessen der Energieumwandlung wie z.B. der Atmung oder der Photosynthese. Solche relativ kurzlebigen Protein-Protein-Komplexe sind an langreichweitigen Elektronentransferreaktionen beteiligt. In den Elektronentransportketten der bakteriellen und mitochondrialen Atmung findet die Bildung eines Komplexes zwischen CcO und Cytochrom *c* statt. Nach der Komplexbildung werden die Elektronen, die CcO zur Reduktion von O_2 zu H_2O benötigt, von Cytochrom *c* auf CcO übertragen. In dieser Arbeit wurde die Komplexbildung zwischen CcO und Cytochrom *c* aus *Paracoccus denitrificans* mit Hilfe gepulster EPR-Spektroskopie untersucht. Hierbei sollte der Einfluss der abstands- und orientierungsabhängigen Elektronenspin-Dipol-Dipol-Wechselwirkung zwischen verschiedenen paramagnetischen Zentren auf die Elektronenspin-Relaxation („relaxation enhancement“) ausgenutzt werden, um verschiedene CcO-Cytochrom-Komplexe zu charakterisieren.

Daher wurden Zweipuls-Elektronenspin-echo-Experimente auf Mischungen aus der löslichen Untereinheit II von CcO, die das Cu_A -Zentrum enthält, bzw. der kompletten CcO mit Cytochrom c_{552} , dem physiologischen Partner, oder Cytochrom *c* aus Pferdeherzen angewandt. In allen vier Fällen konnte eine deutlich verstärkte Relaxation des Cu_A , die durch die Bildung spezifischer Protein-Protein-Komplexe verursacht wurde, beobachtet werden. Im Gegensatz dazu zeigte sich in Experimenten mit dem nichtbindenden Cytochrom c_1 nur eine sehr geringe Verstärkung der Relaxation auf Grund von unspezifischen Protein-Protein-Wechselwirkungen. Ein Vergleich der Echozerfälle des langsam relaxierenden Beobachter-Spins (Cu_A in CcO) in An- bzw. Abwesenheit des schnell relaxierenden Elektronenspins (Fe(III) im Cytochrom) erlaubte es, die rein dipolaren Relaxationsbeiträge für die verschiedenen Komplexe zu separieren und getrennt zu untersuchen. Durch temperaturabhängige Messungen war es möglich, den dipolaren Charakter der beobachteten Verstärkung der Relaxation zu beweisen. Schließlich wurde in dieser Arbeit gezeigt, dass die verwendete experimentelle Herangehensweise auch für den CcO-Cytochrom *c*-Komplex mit der kompletten CcO, die insgesamt vier paramagnetische Zentren enthält, funktioniert.

Quantitative Simulationen der erhaltenen Daten für die verschiedenen Komplexe ergaben eine breite Abstands- (2-4 nm) und Orientierungsverteilung für die relative Anordnung der Cu_A- und Fe(III)-Zentren. Um die Strukturen der Komplexe noch detaillierter zu analysieren und die bisherigen Ergebnisse zu untermauern, werden Hochfeld-EPR-Experimente durchgeführt werden.

Zusammengefasst konnte in der vorliegenden Arbeit gezeigt werden, dass der Einfluss dipolarer Relaxation auf die Ergebnisse gepulste EPR-Experimente dazu verwendet werden kann, Abstände zwischen und relative Orientierungen von paramagnetischen Metallzentren zu untersuchen. Weiterhin wurde auf einem qualitativen Niveau demonstriert, dass diese – zu anderen biophysikalischen Techniken komplementäre – Methode geeignet ist, um kurzlebige Elektronentransfer-Protein-Protein-Komplexe zu studieren. Schließlich konnte in dieser Arbeit experimentell belegt werden, dass die beschriebene Methode auf biologische Systeme mit mehr als zwei paramagnetischen Zentren angewandt werden kann. Dieses Resultat ist insbesondere von Interesse für zukünftige Charakterisierungen von Membranprotein-Superkomplexen.

Contents

Abbreviation and symbols

Introduction	1
A) Molybdenum active site of Psr	
A.1 Goals	5
A.2 Introduction	7
A.2.1 Mononuclear molybdenum enzymes	7
A.2.1.1 Reactions catalyzed by molybdenum containing enzymes	7
A.2.1.2 Structure and function of the molybdopterin cofactor	9
A.2.1.3 Classification of mononuclear molybdenum enzymes	10
A.2.2 Anaerobic respiration	15
A.2.2.1 Sulfur respiration	15
A.2.2.2 Polysulfide respiration	16
A.2.2.3 Electron transport chain in <i>Wolinella succinogenes</i>	17
A.2.2.4 Structure and function of polysulfide reductase	18
A.2.2.5 The function of the Sud protein	19
A.3 EPR spectroscopical background	21
A.3.1 Spin Hamilton operator	21
A.3.2 Basic theoretical principles of ESEEM and HYSCORE	24
A.3.3 The three-pulse ESEEM and HYSCORE experiments	28
A.3.4 Analysis of HYSCORE S=1/2, I=1/2 spin system	33
A.3.5 Analysis of HYSCORE for S=1/2, I>1/2 spin system	35
A.3.6 EPR spectroscopy on the Mo(V) state of molybdenum enzymes	37
A.4 Results and discussion	41
A.4.1 CW-EPR	41
A.4.1.1 Identification of Mo(V) in Psr	41
A.4.1.2 Different Mo(V) states in Psr	42
A.4.1.3 Comparison with other enzymes and model compounds	44
A.4.1.4 Effect of Sud	47
A.4.1.5 ³³ S labeled Polysulfide	49
A.4.2 Pulsed EPR experiments	49
A.4.2.1 Three-pulse ESEEM	50
A.4.2.2 HYSCORE	52

A.4.2.2.1 Orientation dependence	55
A.4.2.2.2 Pulse separation time τ dependence	58
A.4.2.2.3 Quantitative analysis	60
A.5 Summary and Outlook	63
B) Dipolar Relaxation Measurement on the CcO: Cytochrome <i>c</i> Protein complexes	
B.1 Goals	67
B.2 Introduction	69
B.2.1 The respiratory chain	69
B.2.1.1 Components of the respiratory chain	70
B.2.2 Structure and function of the CcO	71
B.2.2.1 Structure of the CcO	71
B.2.2.2 Function of the CcO	72
B.2.3 Structure and function of cytochrome <i>c</i>	74
B.2.4 Electron transfer protein-protein complexes	76
B.2.4.1 Nature and structures of protein-protein complexes	76
B.2.4.2 Model for protein-protein complex formation	78
B.2.4.3 Electron transfer complex between CcO and cytochrome <i>c</i>	78
B.2.4.3.1 CcO binding domain	79
B.2.4.3.2 Cytochrome <i>c</i> binding domain	80
B.2.4.3.3 Kinetics and ionic strength dependence	80
B.2.4.3.4 NMR and MD studies	82
B.2.5 EPR characteristics of CcO and cytochrome <i>c</i>	84
B.2.5.1 EPR characteristics of the redox active metal centers in CcO	84
B.2.5.2 EPR characteristics of cytochrome <i>c</i>	86
B.3 Distance determination by EPR techniques	89
B.3.1 Electron-electron dipole-dipole interaction	90
B.3.2 Pulsed techniques to measure dipole-dipole coupling	92
B.3.3 Relaxation	96
B.4 Results and Discussion	99
B.4.1 Relaxation enhancement: indication for complex formation	100
B.4.2 Specific complex formation	102
B.4.3 Temperature dependence	103
B.4.4 Concentration dependence	108
B.4.5 Orientation dependence	109
B.4.6 Influence of ionic strength	111

B.4.7 Full-size CcO:cytochrome <i>c</i> complex	112
B.4.8 Dipolar relaxation within the CcO	115
B.4.9 Quantitative analysis	116
B.5 Summary and Outlook	119
Summary	121
List of publications and poster presentations	125
Methods and Materials	129
References	133
Acknowledgements	
Curriculum Vitae	

Abbreviations and symbols

a	low spin heme
a_3	high spin heme
A_{iso}	isotropic hyperfine coupling
c_1	cytochrome c_1
c_{552}	cytochrome c_{552}
Cu_A	binuclear mixed valance copper
Cu_B	mononuclear copper
c_{hh}	horse heart cytochrome c
CW	continuous wave
CcO	cytochrome c oxidase
CcO_{II}	soluble subunit II of cytochrome c oxidase
1D	one-dimensional
2D	two-dimensional
DFT	density functional theory
DMSO	dimethyl sulfoxide
dq	double quantum
DQC	double quantum coherence
ENDOR	electron nuclear double resonance
EPR	electron paramagnetic resonance
ESEEM	electron spin echo envelope modulation
EXAFS	extended X-ray absorption fine structure
FeS	iron-sulfur center
g_e	free electron g-factor
g_n	free nuclear g-factor
G	Gauss
HYSCORE	hyperfine sublevel correlation spectroscopy
MGD	molybdopterin guanosine dinucleotide
mw	microwave
NMR	nuclear magnetic resonance

<i>Paracoccus denitrificans</i>	<i>P. denitrificans</i>
PELDOR	pulse electron electron double resonance
Psr	polysulfide reductase
sq	single quantum
Sud	sulfur transferase
tq	triple quantum
ω_I	nuclear Larmor frequency
<i>Wolinella succinogenes</i>	<i>W. succinogenes</i>

Introduction

Modern EPR spectroscopy is a well-established method to investigate paramagnetic centers in biological systems. Two major types of interactions lead to structural information for spin $S = 1/2$ systems:

- the magnetic dipole-dipole interaction to close by nuclei with a nuclear spin I , which can be observed by *Hyperfine Spectroscopy* in a distance range up to 0.8 nm.
- the magnetic dipole-dipole interaction to other paramagnetic centers, which can be investigated by pulse electron electron double resonance (*ELDOR Spectroscopy*) for distances between 1 – 8 nm.

Both methods have been applied most successfully for organic radicals in proteins and nitroxide spin labels covalently attached to biological macromolecules [1-3]. However, the application of these methods is more demanding for paramagnetic metal centers as found in metalloenzymes due to the extremely broad spectral line widths and very short relaxation times. In the present work the applicability of both methods to metal centers is successfully demonstrated:

- A) In the first part of this work the coordination sphere of the catalytically active molybdenum site in polysulfide reductase (Psr), an enzyme from the bacterium *Wolinella succinogenes*, which performs anaerobic respiration with polysulfide was investigated in detail using pulsed hyperfine spectroscopy techniques such as electron spin echo envelope modulation (ESEEM) and hyperfine sublevel correlation spectroscopy (HYSCORE).
- B) The second part of the present work is focused on cytochrome *c* oxidase (CcO) from the gram-negative soil bacterium *Paracoccus denitrificans*. CcO is the terminal enzyme of the respiratory chain and forms an electron transfer complex with cytochrome *c*, which is an important step of the aerobic respiration. This complex formation is studied by pulsed EPR relaxation methods. Relaxation enhancement upon protein-protein binding was observed due to the dipolar coupling between the binuclear Cu_A center of CcO and the heme of cytochrome *c*, which could be used to obtain information about the complex structure.

Each part contains a detailed introduction into the biological systems under study (Chapters A.2 and B.2). Afterwards, a brief introduction into the physical description of the dipole-dipole interaction is given, followed by a short description of the two basic methods used for the two investigations (Chapters A.3 and B.3). Then the experimental results, a discussion of the obtained results and the conclusions are given, both from a method related point of view and in terms of the functional aspects of the investigated membrane proteins (Chapters A.4 and B.4).

Both parts begin with the motivation and goals of the work (Chapter A.1 and A.2).

A) Molybdenum Active Site in Psr

A.1 Goals

Polysulfide reductase (Psr) is a molybdenum containing enzyme which catalyzes the sulfur respiration of the bacterium *W. succinogenes*. The proposed catalytic cycle implies molybdenum in different oxidation states as the active site. The goal of this work was to prove the involvement of the molybdenum center in the catalytic cycle and to show that polysulfide is the substrate using CW and modern pulsed EPR methods at different microwave frequencies. This main goal is divided into the following steps:

1. To generate paramagnetic Mo(V) states using different redox agents and to record the corresponding CW EPR signals.
2. To separate and identify the different Mo(V) states.
3. To determine the number of sulfur ligands in these states.
4. To prove that the sulfur transferase (Sud) protein binds closely to the molybdenum and effects the binding site.
5. To use ^{33}S labeled polysulfide in combination with ESEEM and HYSCORE spectroscopy to prove that the polysulfide is the substrate and structurally characterize the active molybdenum site.

A.2 Introduction

A.2.1 Mononuclear molybdenum enzymes

Molybdenum is widely available to biological systems due to the solubility of its high-valent oxides in water and is an essential trace element for most living systems, including microorganisms, plants and animals. Molybdenum is found associated with a diverse range of redox active enzymes that catalyze basic reactions in the metabolism of nitrogen, sulfur, and carbon. With the exception of nitrogenases that contain an iron-molybdenum-sulfur cluster, molybdenum is incorporated into proteins as the molybdenum cofactor which contains a mononuclear Mo atom coordinated to one or two equivalents of a unique organic cofactor named molybdopterin [4, 5].

A.2.1.1 Reactions catalyzed by molybdenum containing enzymes

The mononuclear molybdenum enzymes may be generally divided into two categories depending on the types of redox reactions being catalyzed. The first category consists of quite large number of enzymes which catalyze oxidative hydroxylation of aldehydes and aromatic heterocyclic compounds in reactions that necessarily involve the cleavage of a C-H bond, formally involving the removal of hydride and replacement with hydroxide. In humans for example, xanthine oxidoreductase catalyses the final two steps in purine metabolism i.e. sequential hydroxylation of hypoxanthine to xanthine and then uric acid. In addition the closely related mammalian aldehyde oxidoreductases are important in the metabolism of a variety of aldehyde compounds and have been implicated specifically in the biosynthesis of retinoic acid, both in the retina and in the developing nervous system. The second class contains enzymes such as dimethyl sulfoxide (DMSO) reductase, nitrate reductase and sulfite oxidase that catalyze oxygen atom transfer reactions to (for oxidases) or from (for reductases) an available electron lone pair of substrate and can itself be subdivided in into two distinct families as shown by sequences comparison and spectroscopic observations i.e. mainly depending whether the source organism is prokaryotic or eukaryotic.

The first of these categories includes for example the sulfite oxidase and the assimilatory nitrate reductases. The former of which is responsible for the final step of sulfur metabolism in humans: oxidation of sulfite to sulfate and the physiological

function of the latter, for example in higher plants is to reduce nitrate to nitrite in the first step in the assimilation of nitrate from the soil.

The second family consists of bacterial periplasmic or membrane associated enzymes such as DMSO reductase and dissimilatory (or respiratory) nitrate reductases which function as the terminal respiratory oxidases [4, 5]. However, it has to be noted that the above generalizations is not applicable to the entire second major class of enzymes as a growing number of prokaryotic molybdenum enzymes catalyze reaction other than oxygen atom transfers. For example polysulfide reductase, selenate reductase and formate dehydrogenase H catalyze dehydrogenation reactions, the reductive cleavage of sulfide from polysulfide, the reduction of selenate to selenite, and the oxidation of formate to carbonate, respectively [6, 7].

Common of all the above described catalytic reactions is the cycling between oxidized Mo(VI) and the reduced Mo(IV) states of the enzyme. The overall reaction mechanism could be considered as consisting of a coupled pair of reductive and oxidative half reactions, characterized by the reduction of Mo(VI) and the oxidation of Mo(IV), respectively. Because the mononuclear molybdenum enzymes catalyze a two electron redox reactions to or from the substrate, it is likely that the Mo also directly undergoes a two electron change in oxidation state during the appropriate half reaction. The return to the resting state of the enzyme must involve either addition or removal of electrons at the Mo, by means of electron transfer between the Mo and a second redox center. Since the second center is typically a one electron redox group, such as iron-sulfur cluster or a heme, the Mo is restored to the resting state through a sequence of one electron transfers that will first generate the intermediate Mo(V) state. For example, the resting state of DMSO reductase is the Mo(IV) state that binds DMSO, followed by reduction of the substrate to produce dimethylsulfoxide (DMS) and the Mo(VI) state of the enzyme. The subsequent one electron transfer reactions regenerate the Mo(IV) state after passing through the Mo(V) state [8-10]. The intermediate Mo(V) state of this enzyme as well as in other mononuclear molybdenum enzymes is paramagnetic analog of the true Michaelis complex and as such represents a sensitive probe of the Mo environment in the active site. Therefore the intermediate Mo(V) state of many molybdenum enzymes has been a target of a number of EPR spectroscopic investigations, focused on the details of the Mo active site geometry and the implication of these structural knowledges for the catalytic mechanisms of the enzymes [4, 11].

A.2.1.2 Structure and function of the molybdopterin cofactor

The pyranopterin cofactor common to all mononuclear molybdenum enzymes has the basis structure shown in Figure 1a. It coordinates the Mo via the sulfur atoms of the dithiolene side chain. The ligation is usually accompanied by significant displacement of Mo from the plane of the dithiolene group. The binding of Mo can result in a 1:1 or 2:1 pyranopterin to Mo ratio. The pyranopterin cofactor is distinctly nonplanar in its pyran and central pyrazine ring. The pterin and pyran rings in the tricycle enclose an angle of approx. 40°, the pyrazine ring is twisted.

In eukaryotes, the pterin cofactor possesses the structure as shown in Figure 1a. In bacteria additional variability is achieved since the cofactor is conjugated to nucleosides, usually guanosine or cytosine and occasionally adenosine [12, 13].

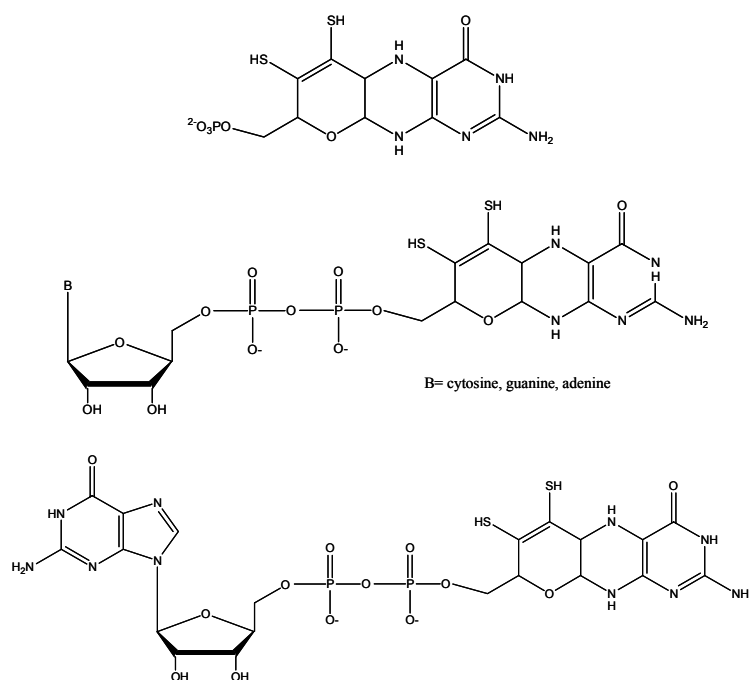


Fig. 1: Structure of the molybdopterin cofactor: the organic component of all enzymes that contain a molybdopterin cofactor, in eukaryotes (a) and (b) in prokaryotes as a dinucleotide of guanosine, cytosine or adenosine. Structure of the pterin guanosine dinucleotide cofactor as present in the enzymes of DMSO reductase family (c).

The molybdopterin cofactor represents an integral component of the molybdenum centers of the mononuclear molybdenum enzymes, but does not participate directly in catalysis. Hydrogen bonding interactions with the polypeptide are typically extensive. In addition, the pyranopterin appears to be involved in electron transfer, because of its structure the cofactor represents the path of electron transfer out of the molybdenum center once it has been reduced by the substrate. For example for the xanthine

oxidase, a specific mechanism by which the conformation of the pyranopterin modulates electron transfer out of the molybdenum center has been proposed, involving alternate conformations of the Mo center as observed in the crystal structure and by EPR on the “vary-rapid” catalytic Mo(V) intermediate [11].

Additional function of the molybdopterin cofactor involves modulating the electronic structure of the molybdenum center, in particular the reduction potential. It has been shown that the greater the covalency in the Mo-S bond, the lower the effective charge on the metal and the more difficult to formally reduce the molybdenum from Mo(VI) to Mo(IV) oxidation state. Therefore changes in covalency from one protein to the next clearly contribute significantly to differences in reduction potential [4, 5].

A.2.1.3 Classification of mononuclear molybdenum enzymes

The molybdenum containing enzymes can be distinguished according to their amino acid sequences, spectroscopic properties, active site structures and catalyzed reactions. However, based on the rapidly growing number of X-ray crystal structures a classification based on structural homology of the active sites became appropriate. Considering this the molybdopterin containing enzymes can be grouped into three distinct families, represented by DMSO reductase, xanthine oxidase and sulfite oxidase [4, 5]. The active sites of these enzymes are shown in Figure 2.

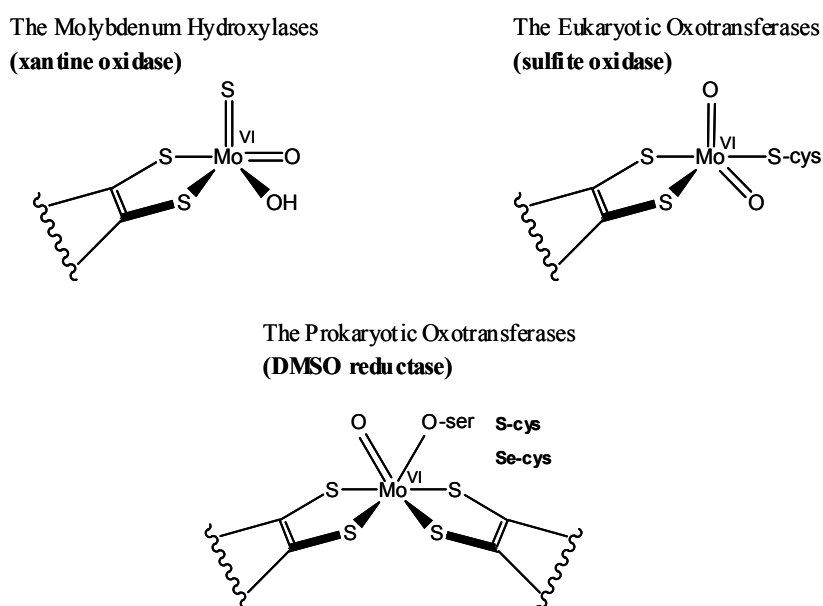
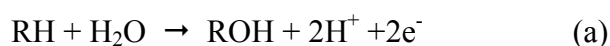


Fig. 2: Structures of the active sites of the three principal families of molybdenum enzymes.

The xanthine oxidase family

These enzymes range from the well characterized xanthine and aldehyde oxidoreductases from higher organisms to bacterial enzymes responsible for the oxidative hydroxylation of wide range of aromatic heterocycles and aldehydes. The catalyzed reaction follows the general reaction scheme (a).

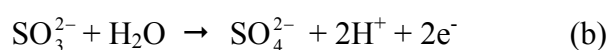


This stoichiometry is unique among biological systems catalyzing hydroxylation reactions in that reducing equivalent are generated rather than consumed in the course of the reaction. The source of oxygen incorporated into the substrate by the molybdenum hydroxylases, as exemplified by xanthine oxidase, is derived from water rather than dioxygen. The overall reaction mechanism of these enzymes is typically broken down into reductive and oxidative half reactions of the catalytic cycle. It is the reductive half reaction in which the Mo center participates with the metal becoming reduced from Mo(VI) to Mo(IV) in the course of chemistry leading to hydroxylation. Xanthine oxidase and xanthine dehydrogenase are two different forms of the same enzyme and they catalyze the conversion of xanthine to uric acid in the catabolic metabolism of purine bases and the distinction between them is based on the substrate specificity in the oxidative half reaction of the catalytic cycle.

The crystal structures of the bovine milk xanthine oxidase as well as of other members of this family have been determined and the active site of this group of enzymes consists of a single equivalent of the molybdopterin cofactor and three additional oxygen ligands are bound to the molybdenum, two of them are interpreted as a water and a oxogroup and the third was modeled as an oxogroup [14, 15].

The sulfite oxidase family

Sulfite oxidase is located in the mitochondrial intermembrane space where it catalyzes the oxidation of sulfite to sulfate, with cytochrome *c* as physiological oxidizing substrate, according to the overall reaction shown in scheme (b). This is the terminal reaction in the oxidative degradation of the sulfur containing amino acids cysteine and methionine.



The Mo center of sulfite oxidase is reduced from Mo(VI) to Mo(IV) oxidation state in the reductive half reaction of the catalytic cycle i.e. the reaction of the enzyme with sulfite and the reducing equivalents are transferred individually to the hem center and then passed to cyt *c* in the oxidative half reaction.

The only known till now oxotransferases from eukaryotic sources are sulfite oxidases and assimilatory nitrate reductases from algae and higher plants. The structure of chicken liver sulfite oxidase has been determined and this enzyme contains a single molybdopterin cofactor binding the molybdenum ion. Molybdenum is coordinated by five ligands: three sulfur ligands, one water/hydroxo ligand and an oxo group. Two of the sulfur ligands originate from the dithiolene sulfurs while the third sulfur is from a cysteine amino acid [16].

The DMSO reductase family

The prokaryotic oxotransferases represent the most structurally diverse family of molybdenum enzymes. Members of the DMSO reductase family are exclusively found in eubacteria and include, among the other enzymes, the dissimilatory nitrate reductases, formate dehydrogenases and sulfoxide reductases.

A number of enzymes from different sources have been characterized by X-ray crystallography [17-24]. The Mo(VI) active site in the enzymes of the DMSO reductase family has many common features, as revealed by their crystal structure. All these enzymes contain a *bis* molybdopterin guanosine dinucleotide (MGD) form of the molybdopterin cofactor, the two MGDs each providing two thiolate sulfur ligands to the Mo. The fifth ligand to the Mo is provided by an amino acid side chain of the surrounding polypeptide. In DMSO reductase from *R. sphaeroides* and *R. capsulatus* this additional ligand is a serine [17-20]. In the NAP dissimilatory nitrate reductase from *D. desulfuricans* the serine is replaced by a cysteine [21]. In the *E. coli* formate dehydrogenase this fifth ligand is found to be a selenocysteine [22]. A labile oxo(=O), hydroxo (-OH), or water (-OH₂) group provides the sixth ligand to the molybdenum, in the oxidized form of the metal, which is exchanged during catalysis. Structures for the representatives of each subgroup of this family are shown in Figure 3.

This family of enzymes also displays considerable variation in the number and organization of additional redox active centers in the enzyme. Prosthetic groups found in members of this enzyme family are iron-sulfur [2Fe-2S], [4Fe-4S] and [4Fe-4S], clusters respectively, b-type heme groups and flavin groups.

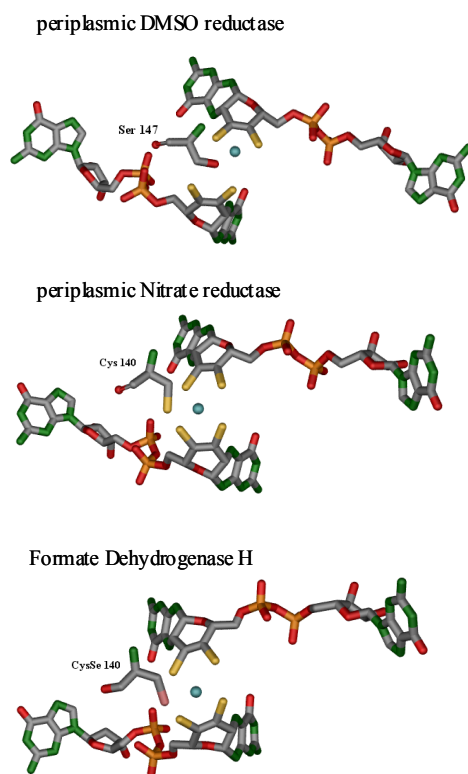
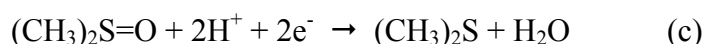


Fig. 3: The arrangement of ligands surrounding the Mo atom in the active sites of *R. sphaeroides* and *R. capsulatus* DMSO reductase (PDB codes 1EU1 and 1DMS), *D. desulfuricans* nitrate reductase (PDB code 1NAP), *E. coli* formate dehydrogenase H (PDB code 1AA6), as determined by X-ray crystallography.

Members of the DMSO reductase family typically catalyze oxygen atom transfer reaction to or from an available electron pair on the substrate. Generalizations regarding the reaction mechanism for this family of enzymes are difficult because of the wide range of reactions catalyzed. Nevertheless, some examples of the reaction mechanism for the main representatives of this family of enzymes are described below.

Periplasmic DMSO reductase located in the periplasmic space of bacteria catalyzes the reductive deoxygenation of dimethyl sulfoxide to dimethyl sulfide according to scheme (c).



DMSO appears to cycle between monooxo Mo(VI) and desoxo Mo(IV) states in the course of catalysis.

In the oxidative half cycle of the reaction catalyzed by DMSO reductase, the reduced Mo(IV) form of the enzyme binds the substrate, and two electrons are transferred

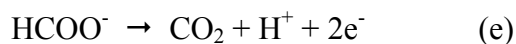
from Mo to the substrate yielding the reaction product DMS and the oxygen atom of the substrate bound to the metal as an oxo-ligand. In the second reductive half reaction, two protons and two electrons are transferred to the metal center yielding H₂O and regenerating the Mo(IV) state i.e. two cycles of binding of the physiological electron donor to the oxidized enzyme are required, in each of them a single electron is transferred to the active site restoring finally the Mo(IV) state of the enzyme.

Bacterial dissimilatory Nitrate reductase: periplasmic (NAP) or respiratory membrane bound (NAR) nitrate reductases catalyze the two electron reduction of nitrate to nitrite (reaction scheme d).



NAR couples the reduction at the expense of mannaquinol to generate transmembrane proton gradient used for ATP synthesis. NAP enzymes as consequences of their location do not contribute to the generation of proton motive force. It is assumed they are used for redox balancing, which can become important for optimal growth depending on the physiological conditions.

Formate dehydrogenase H (FDH) is membrane associated protein and functional in the anaerobic metabolism of bacteria. It catalyzes the oxidation of formate to carbon dioxide concomitant with the release of a proton and two electrons. The reaction catalyzed by FDH is unusual as it does not involve oxygen atom transfer, at least formally. It rather represents the cleavage of a C-H bond with concomitant formation of a C=O bond from C-OH, as it is indicated in scheme (e).



Polysulfide reductase (Psr) from *W. succinogenes* is also molybdenum containing protein closely related to the mention above members of the DMSO reductase family of enzymes. It is a membrane bound protein and together with formate dehydrogenase catalyzes the overall reaction shown in scheme (f), proton gradient is generated across the membrane which drives the ATP synthesis in *W. succinogenes* [4-6].



Since there is no three dimensional structure available of Psr and only a little is known for the reaction mechanism, this enzyme is of particular interest in this work as EPR spectroscopy could be applied for identification of the ligands at its catalytically active molybdenum site, eventually leading to better understanding of the catalytic mechanism as intermediate paramagnetic Mo(V) state might be part of the overall catalytic reaction.

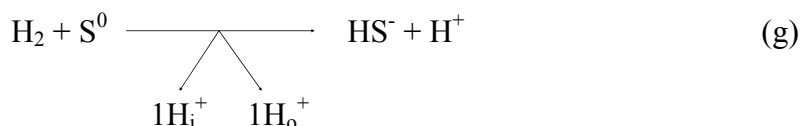
A more detailed description of polysulfide reductase isolated from the bovine rumen bacterium *W. succinogenes* is given in the following chapter.

A.2.2 Anaerobic respiration

Certain anaerobic prokaryotes perform “oxidative phosphorylation” without oxygen. Depending on the species and metabolic conditions, these bacteria use a large variety of inorganic (e.g. nitrate, nitrite, sulfate, elemental sulfur) or organic (e.g. fumarate, dimethylsulfoxide) compounds as terminal electron acceptors instead of oxygen. The redox reactions are catalyzed by membrane integrated enzymes, forming electron transport chains and are coupled to the generation of electrochemical proton potential across the membrane which drives the ATP synthesis. Oxidative phosphorylation in absence of oxygen is termed anaerobic respiration.

A.2.2.1 Sulfur respiration

The Gram-negative bacterium *Wolinella succinogenes* isolated from cattle rumen uses elemental sulfur as terminal electron acceptor i.e. it performs anaerobic respiration with elemental sulfur or sulfur respiration. The bacterium uses hydrogen or formate as the electron donors in the sulfur respiration. *W. succinogenes* grow with hydrogen and elemental sulfur as the sole metabolic substrates therefore it is likely that the reaction (g) is coupled to consumption of protons from the inside (H_i^+) and to a proton release on the outside (H_o^+) of the membrane [25-27].



A.2.2.2 Polysulfide respiration

The elemental sulfur is not well suited as a substrate of bacterial sulfur respiration because of its low solubility in water. However, elemental sulfur readily dissolves in aqueous solutions containing sulfide (HS^-) which is the product of sulfur respiration and as a result polysulfide is formed abiotically according to reaction (h) and appears to be the soluble intermediate in the sulfur reduction catalyzed by *W. succinogenes*.

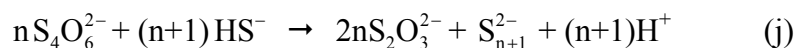


The S_8 ring is cleaved by nucleophilic attack of HS^- . The amount of elemental sulfur dissolved is a function of the sulfide concentration and the pH. The amount of sulfur that can maximally be dissolved in a sulfide solution at pH 8 and 37 °C is nearly equivalent to the sulfide content. Much less polysulfide is formed at pH values below the pK of H_2S (7.0).

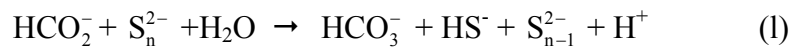
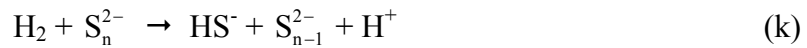
Tetrasulfide (S_4^{2-}) and pentasulfide (S_5^{2-}) are the predominant species of polysulfide at pH values above 6. The two species dismutate rapidly according to reaction (i).



As a consequence of reaction (i) it is not known whether S_4^{2-} or S_5^{2-} is preferred substrate of Psr. For the same reason, the product of polysulfide reduction is not known. It is assumed that only one sulfur atom is cleaved from the polysulfide chain during catalysis. It has been determined from the equilibrium constant of this reaction that the concentration of S_4^{2-} is twice that of S_5^{2-} in a solution (pH 8.5 and 37 °C) containing 1mM polysulfide sulfur and 2mM HS^- . With the simplification that only S_4^{2-} is formed upon dissolution of sulfur it has been determined that the redox potential of the polysulfide is only slightly more positive than that of elemental sulfur. The activity of polysulfide reduction with hydrogen has been measured. In these experiments polysulfide solutions were flushed with hydrogen and the reaction was started by addition of the enzyme. The polysulfide used in these experiments was formed from tetrathionate and sulfide, according to reaction (j).



The apparent K_M measured with polysulfide respiration of *W. succinogenes* is close to the concentration of polysulfide sulfur ($10\mu\text{M}$) that has been found to be required for polysulfide respiration to occur in other bacteria. Therefore, it has been suggested that polysulfide may be the soluble intermediate, formed from sulfur in bacterial sulfur respiration. It has been also suggested that *W. succinogenes* uses polysulfide as the actual substrate of sulfur respiration. Additionally, the comparison of the enzymatic properties of the bacteria grown under various conditions supported the suggestion that polysulfide reduction is an essential step in the sulfur respiration of *W. succinogenes* and that in fact the actual electron acceptor is polysulfide with either hydrogen (k) or formate (l) as electron donors [27-29].



A.2.2.3 Electron transport chain in *W. succinogenes*

The electron transport chain catalyzing polysulfide reduction by hydrogen or formate consists of polysulfide reductase, methyl-menaquinine and either hydrogenase or formate dehydrogenase (Figure 4).

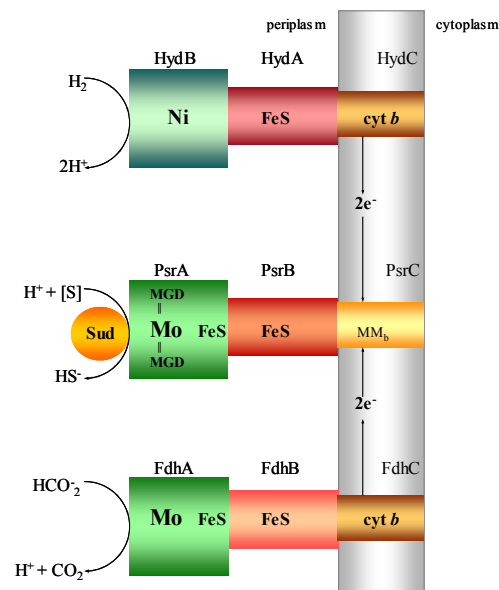


Fig. 4: The electron transport chain catalyzing polysulfide respiration with H_2 or formate in *W. succinogenes*. HydA,B,C, hydrogenase; PsrA,B,C, polysulfide reductase, FdhA,B,C, formate dehydrogenase.

The enzymes are integrated in the cytoplasmic membrane with catalytic subunits exposed to the periplasm. Each enzyme consists of two hydrophilic and one hydrophobic subunit, anchoring the enzyme in the membrane. The hydrophobic subunits of hydrogenase and formate dehydrogenase are similar di-heme cytochromes *b* which carries the site of quinone reduction. The hydrophobic subunit of polysulfide reductase probably carries methyl-menaquinone, which is thought to accept electrons from the cytochromes *b* of the dehydrogenases. The larger hydrophilic catalytic subunits of the enzymes carry the substrate sites. The smaller hydrophilic subunits carry different number of iron-sulfur centers which probably mediate the electron transfer from the catalytic to the membrane integrated subunit [6, 25-29].

A.2.2.4 Structure and function of polysulfide reductase

Polysulfide reductase consists of three subunit (psrA, B, C) predicted from the nucleotide sequence of the *psrABC* operon. The enzyme contains a molybdenum and molybdopterin guanine dinucleotide (MGD) [25]. These cofactors are likely to be bound to the subunit PsrA together with a [4Fe-4S] iron-sulfur cluster which is predicted by the amino acid sequence of PsrA. The catalytic subunit PsrA of polysulfide reductase belongs to the DMSO reductase family of molybdo-oxidoreductases as indicated by its amino acid sequence. Therefore, PsrA is likely the catalytic subunit of Psr, and likely carries the molybdenum ion coordinated by two MGD molecules.

It is predicted, based on the nucleotide sequence of *psrB* that the subunit PsrB carries four additional [4Fe-4S] iron-sulfur centers. Each of these four iron-sulfur centers appears to be required for the electron transport. This is suggested by mutagenesis studies where each cysteine residue in the four iron-sulfur centers was replaced and the corresponding mutants did not catalyze the electron transport reactions from hydrogen or formate to polysulfide. The methyl-menaquinone is predicted to be bound to the membrane anchor PsrC of the enzyme.

With the assumption that PsrA resembles the enzymes of the DMSO family, the molybdenum ion, coordinated by two MGD appears to be the electron donor to or acceptor from the substrates. It is likely that the substrates, polysulfide and protons reach the active site near the molybdenum through a cavity extending from the surface of the protein to the molybdenum, close to the protein center. Here a sulfur

atom is reductively cleaved from the end of the polysulfide chain according to reaction (m) and the products are released through the cavity (Figure 5).



Since PsrA is orientated towards the periplasmic side of the membrane, the substrates are taken from the periplasm and the products are released to the same side. The electrons required for the redox reaction are thought to be provided by the molybdenum ion in the reduced state (Mo^{4+}). In the oxidized (Mo^{6+}) state, molybdenum is thought to be reduced via the iron-sulfur centers of PsrA and PsrB by reduced methyl-menaquinone of PsrC.

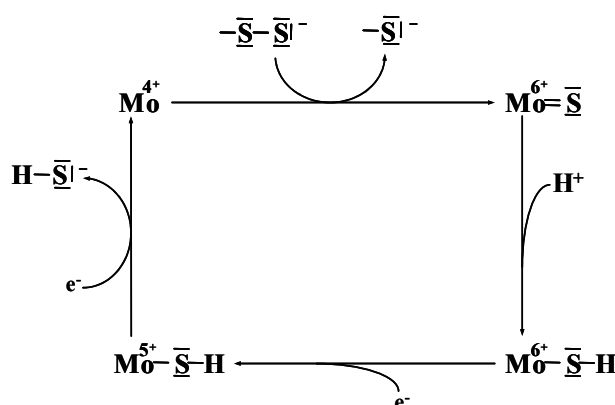


Fig. 5: Hypothetical mechanism of polysulfide reduction at the substrate site of Psr. A sulfur atom is cleaved from the end of the polysulfide chain and bound to the Mo ion which is thereby oxidized. After the uptake of a proton and two electrons, HS^- is released and Mo ion returns to the reduced state again.

A.2.2.5 The function of the Sud protein

Growth and survival by polysulfide respiration may be critical for bacteria living at low pH and or low sulfide concentration. Therefore, it is not surprising that sulfur reducers synthesize a binding protein for polysulfide which is designed to allow rapid polysulfide respiration even at low polysulfide concentrations. The periplasmic polysulfide-sulfur transferase (Sud) protein of *W. succinogenes* appears to serve as such a binding protein. Sud consists of two identical subunits and does not contain heavy metal ions or other prosthetic groups. It appears that Sud function as a polysulfide binding protein and probably binds polysulfide sulfur to a cysteine residue and transfers it to the active site of the membrane embedded Psr, allowing rapid polysulfide reduction at low substrate concentrations [31-33].

Indeed it has been demonstrated that Sud contains a single cysteine residue (Cys109) which is essential for sulfurtransferase activity and sulfur binding. Polysulfide appears to be covalently bound to the catalytic cysteine residue of Sud as Sud incubated with polysulfide was found to carry one or two sulfur atoms per monomer. Additionally, it has been shown that the activity of electron transport from hydrogen to polysulfide at low polysulfide concentration (below 0.1 mM) is significantly increased by the presence of Sud. A stimulating effect of Sud was not observed at higher concentrations of polysulfide. The increased activity in presence of Sud was taken as an indication that sulfur is transferred from Sud to the substrate site of Psr. It is likely that Psr reacts faster with the polysulfide sulfur bound to Sud than with free polysulfide, and binding of polysulfide to Sud appears to be faster than direct binding of polysulfide to Psr at low sulfur concentrations. The transfer of polysulfide from Sud to Psr probably occurs in a complex of the two proteins i.e. Sud is bound to Psr, where it takes up polysulfide and delivers it to the reductase. In the functional complex consisting of Sud and Psr, the end of the polysulfide chain bound to the cysteine residue of Sud may come close to the catalytic molybdenum site where the reduction of polysulfide takes place i.e. a sulfur atom is cleaved.

Additionally, the interaction of Sud with polysulfide reductase was studied by NMR spectroscopy and eight residues of the Sud were found to be affected by presence of polysulfide reductase. These residues, which form a ring around the cysteine residue, are thought to make contact with Psr.

A.3 EPR theoretical background

Electron paramagnetic resonance (EPR) spectroscopy is a well known technique for investigation of the local structure of paramagnetic species, including biomolecules [34-36]. The continuous wave (CW) technique had been the major tool to characterize the metal centers in metalloproteins. It could reveal information about the oxidation state and the ligand geometry, the distance between the metal and nuclei in its close vicinity. If more than one paramagnetic center is present in the molecule it also can give information about the distance between them and their relative orientation. However, in many cases of metalloproteins interaction of the unpaired electron with more distant nuclei or other paramagnetic center with unpaired electron are of interest. In such cases advanced pulsed EPR spectroscopy is the method of choice. Pulsed ESEEM and ENDOR techniques are sensitive to the interaction of the paramagnetic species with nuclei within a distance range of up to 0.8 nm [3, 37-51], while PELDOR and relaxation experiments are sensitive to the dipolar interaction with other paramagnetic center with distances up to approximately 8 nm [1, 2].

A.3 1 Spin Hamilton operator

The basics of determination and interpretation of the EPR parameters of paramagnetic species, which contain the information about their geometrical and electronic structures, lay in the static spin Hamiltonian [36, 52-54].

The EPR spectrum of a paramagnetic center with an single unpaired electron spin ($S = 1/2$) and m nuclei with spin I , in an external magnetic field \mathbf{B}_0 can be described by the static spin Hamiltonian {1}.

$$\begin{aligned}
 H_o &= H_{EZ} + H_{HF} + H_{NZ} + H_{NQ} \\
 &= \beta_e \mathbf{B}_0 \mathbf{g} \mathbf{S} / \hbar + \sum_{k=1}^m \mathbf{S} \mathbf{A}_k \mathbf{I}_k - \beta_n \sum_{k=1}^m g_{n,k} \mathbf{B}_0 \mathbf{I}_k / \hbar + \sum_{k=1}^m \mathbf{I}_k \mathbf{Q}_k \mathbf{I}_k
 \end{aligned} \quad \{1\}$$

The electron Zeeman term H_{EZ} represents the interaction of the unpaired electron spin with the external magnetic field \mathbf{B}_0 via the anisotropic \mathbf{g} tensor. The next two terms, the nuclear Zeeman H_{NZ} term and term H_{HF} describe the interactions of close by nuclear spins I with the external magnetic field \mathbf{B}_0 and with the electron spin via the hyperfine tensor \mathbf{A} , respectively. The last term H_{NQ} describes the nuclear quadrupole interactions \mathbf{Q} for spins with nuclear spin quantum number $I > 1/2$. The parameters β_e

and β_n are the electron and nuclear Bohr magneton, respectively and g_n is the nuclear g factor.

For simplicity further on a system consisting only of a single nucleus interacting with the unpaired electron spin is considered.

The electron Zeeman term is the predominant term in the static spin Hamiltonian

$$H_{EZ} = \beta_e \mathbf{B}_0 \mathbf{gS} / \hbar \quad \{2\}$$

$$\mathbf{g} = \begin{pmatrix} g_{xx} & & \\ & g_{yy} & \\ & & g_{zz} \end{pmatrix} \quad \{3\}$$

\mathbf{g} is the so called g-tensor of the paramagnetic species. It can be formulated as a symmetric tensor with three principal values g_{xx} , g_{yy} , g_{zz} and three Euler angles describing the orientation of the principal axes in a molecular coordinate system. Usually the \mathbf{g} principal axes frame is considered as the molecular frame and all interaction tensors are referred to this frame. For axial symmetry $g_{xx} = g_{yy} = g_{\perp}$ and $g_{zz} = g_{\parallel}$ and for orthorhombic symmetry $g_{xx} \neq g_{yy} \neq g_{zz}$. For powder samples, containing metals as paramagnetic centers is usually possible to resolve the principle values of \mathbf{g} at the standard X-Band frequency and thus leading to their identification.

The hyperfine interaction between the electron and the nuclear spin of a single nucleus is represent then by the Hamiltonian

$$H_{HF} = \mathbf{SAI} \quad \{4\}$$

which comprises on of the most important source of information in EPR spectroscopy as it will be shown later in this work. Equation (2) with the hyperfine tensor \mathbf{A} can be written as the sum of the isotropic interaction (Fermi contact term H_F), which arises from the finite probability of the electron being located at the position of the nucleus, and the anisotropic electron-nuclear dipolar coupling H_{DD} , which includes the interaction between the magnetic moments of the electron and of the nucleus

$$H = H_F + H_{DD} \quad \{5\}$$

The Fermi contact interaction is given by

$$H_F = A_{iso} \mathbf{SI} \quad \{6\}$$

where,

$$A_{iso} = \frac{2}{3} \frac{\mu_0}{\hbar} g_e \beta_e g_n \beta_n |\Psi_0(0)|^2 \quad \{7\}$$

is the isotropic hyperfine coupling constant and $|\Psi_0(0)|^2$ is the electron spin density at the nucleus.

The classical expression for the magnetic coupling between the electron and the nuclear magnetic moments is

$$E_{dd} = \frac{\boldsymbol{\mu}_e \cdot \boldsymbol{\mu}_n}{R^3} - \frac{3(\mathbf{R} \cdot \boldsymbol{\mu}_e)(\mathbf{R} \cdot \boldsymbol{\mu}_n)}{R^5} \quad \{8\}$$

with $\boldsymbol{\mu}_e = -g_e \beta_e \mathbf{S}$ $\boldsymbol{\mu}_n = g_n \beta_n \mathbf{I}$.

The quantum mechanical version of the electron-nuclear dipole-dipole coupling is represented by a Hamiltonian of the form

$$H_{DD} = \frac{\mu_0}{4\pi} g_e \beta_e g_n \beta_n \left[\frac{\mathbf{S} \cdot \mathbf{I}}{R^3} - \frac{3(\mathbf{R} \cdot \mathbf{S})(\mathbf{R} \cdot \mathbf{I})}{R^5} \right] \quad \{9\}$$

where \mathbf{R} is the vector connecting the electron and the nuclear spin and R is the distance between the two spins. Integration over the spatial electron distribution yields the Hamiltonian for the anisotropic dipole-dipole coupling

$$H_{DD} = \mathbf{S} \mathbf{T} \mathbf{I} \quad \{10\}$$

with the dipolar coupling tensor \mathbf{T} . In the hyperfine principle axis system the dipolar interaction is given by the diagonal tensor

$${}^d \mathbf{T} = \frac{\mu_0}{4\pi} \frac{g_e \beta_e g_n \beta_n}{R^3} \begin{pmatrix} -1 & & \\ & -1 & \\ & & 2 \end{pmatrix} = \begin{pmatrix} -T & & \\ & -T & \\ & & 2T \end{pmatrix} \quad \{11\}$$

if the high-field approximation applies.

This expression is strictly valid for an isotropic g tensor. Nevertheless it is often used as an approximation in cases where the g anisotropy is small.

The complete hyperfine tensor \mathbf{A} is given by

$$\mathbf{A} = \begin{pmatrix} A_{xx} & & \\ & A_{yy} & \\ & & A_{zz} \end{pmatrix} = \begin{pmatrix} A_{iso} - T & & \\ & A_{iso} - T & \\ & & A_{iso} + 2T \end{pmatrix} \quad \{12\}$$

For axially symmetry hyperfine tensor $A_{xx}=A_{yy}=A_{\perp}$ and $A_{zz}=A_{\parallel}$. A_{\parallel} is the component with magnetic field parallel to the interspin vector and is the component when the magnetic field is perpendicular to this vector. The isotropic value A_{iso} of the full tensor can be determined from

$$A_{iso} = 1/3(A_{xx} + A_{yy} + A_{zz}) \quad \{13\}$$

Nuclei with spin $I > 1/2$ are distinguished by a non-spherical charge distribution by a nuclear quadrupole moment Q . The interaction of this charge distribution with the electric field gradient, caused by the electrons and the near by nucleus is described by

$$H_{NQ} = \mathbf{IQI} \quad \{14\}$$

where the \mathbf{Q} is the nuclear quadrupole tensor. In its principal axes system, \mathbf{Q} is traceless and the Hamiltonian can be express as

$$H_{QZ} = Q_{xx}I_x^2 + Q_{yy}I_y^2 + Q_{zz}I_z^2 = \frac{e^2qQ}{4I(2I-1)\hbar} \left[(3I_z^2 - I(I+1)^2) + \eta(I_x^2 - I_y^2) \right] \quad \{15\}$$

where eq is the electric field gradient and $\eta = (Q_{xx} - Q_{yy})/Q_{zz}$ is the asymmetry parameter with $|Q_{zz}| \geq |Q_{yy}| \geq |Q_{xx}|$ and $0 \leq \eta \leq 1$. The largest principal value of the quadrupole tensor is given by $Q_{zz} = eqQ/(2I(2I-1)/\hbar)$. The nuclear quadrupole tensor in its principle axis system has the form of

$$\mathbf{Q} = \begin{pmatrix} Q_{xx} & & \\ & Q_{yy} & \\ & & Q_{zz} \end{pmatrix} = \frac{qe^2Q}{4I(2I-1)/\hbar} \begin{pmatrix} -(1-\eta) & & \\ & -(1+\eta) & \\ & & 2 \end{pmatrix} \quad \{16\}$$

The principle axis systems of the tensors \mathbf{g} , \mathbf{A} and \mathbf{Q} are related by appropriate Euler angles.

A.3.2 Basic theoretical principles of ESEEM and HYSCORE

Electron spin echo envelope modulation (ESEEM) spectroscopy enables to investigate paramagnetic species with hyperfine interaction between the unpaired electron spin and the surrounding nuclear spins, similar as Zeeman splitting [55-57]. The ESEEM spectra contain information on the type of nuclei in the vicinity of the unpaired electron (nuclear Zeeman interaction), about the distribution of spin density and the distance between the unpaired electron and the nuclei (hyperfine interaction)

and on the electric field gradient at the nuclei (nuclear quadrupole interaction) [58-68]. All these data can be translated into information about the electronic and geometric structure of the paramagnetic species.

The ESEEM spectroscopy is a pulsed EPR technique where an electron spin echo is created by application of microwave-pulse sequence and the echo intensity then is recorded as a function of one time interval between the microwave pulses. The echo shows periodic amplitude which modulates as function of the pulse separation time. The echo modulation is damped by relaxation. The frequencies of this modulation correspond to the nuclear transition frequencies (often referred to also as ENDOR frequencies) of the surrounding nuclei. They depend on the nuclear Zeeman, and hyperfine and quadrupole interactions.

At present, variety of microwave pulse sequences, that consists of several pulses and time intervals are available. Some of them allow independent variation of more than one time interval between the different pulses which leads to possibility of recording also a multi dimensional ESEEM traces [55]. Details about the particular pulse sequences used in this work will be given later. However, in all cases, the application of series of microwave pulses and the observation of the electron spin echo as a function of one or two time intervals between the different pulses, results in a 1D- or 2D- array of data in the time domain. Fourier transformations of the time-domain echo envelope yield the nuclear transition frequency spectra in one or two dimensions.

A theoretical treatment of the nuclear modulation effect is based on the spin density operator formalism which is given in ref. [55-57] and will be not discussed here.

It can be shown by such a treatment that the nuclear modulation is mostly determined by the eigenvalues and eigenvectors of the static spin Hamiltonian which applies when the microwave pulses are off. The appearance of the echo modulation in the ESEEM experiment can be much easily explained on a four level spin energy diagram for a system consisting of a nuclear spins $S = 1/2$ interacting with an electron spin $S = 1/2$ in a constant magnetic field (Figure 6).

The splitting of the two levels with $m_s = 1/2$, (equal to $h\omega_\alpha$), differs from the splitting $h\omega_\beta$ of the levels with $m_s = -1/2$ due to the hyperfine interaction of nuclear spin with the electron spin. Four EPR transitions are possible between the two electron spin manifolds. Two allowed electron spin-flip transitions in which the nuclear spin does

not flip ($\Delta m_s = \pm 1, \Delta m_l = 0$) and two forbidden electron spin-flip transitions for which the nuclear spin flips simultaneous ($\Delta m_s = \pm 1, \Delta m_l = \pm 1$).

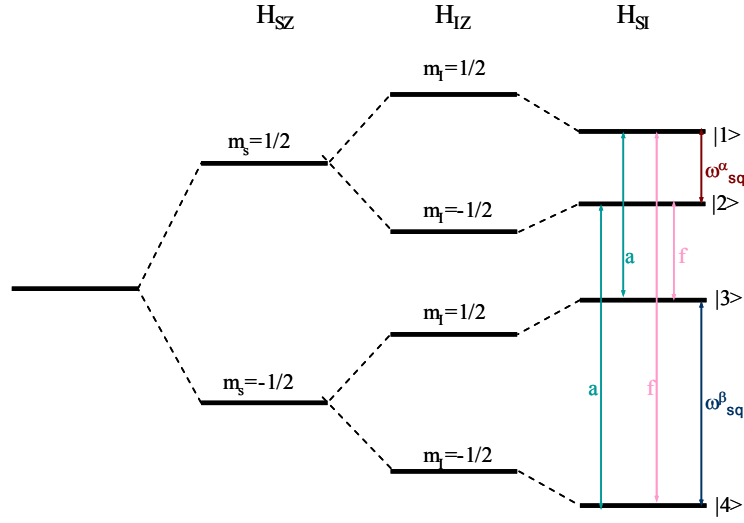


Fig. 6: Energy level diagram for an electron spin $S=1/2$ coupled to a nuclear spin $I=1/2$ at external magnetic field $B_0=0$. The symbols (a) and (f) denote the allowed and the forbidden EPR transition respectively. The single quantum nuclear transitions are denoted as ω_{sq}^α and ω_{sq}^β .

The two transitions between the levels with the same magnetic quantum number m_s ($\Delta m_s = 0, \Delta m_l = \pm 1$) are the NMR transitions. These two nuclear transitions with transition frequencies ω_α and ω_β respectively are excited differently in the electron nuclear double resonance (ENDOR) experiment where an additional radiofrequency field is applied, and are thus called also the ENDOR frequencies.

In the ESEEM experiment the nuclear transitions frequencies are observed due to mixing of the frequencies of the forbidden and allowed EPR transitions. Owing to anisotropic hyperfine interaction the allowed and forbidden transitions between the upper and lower states are both induced. With other words, the eigenfunctions of the spin Hamiltonian α and β , are mixed states because of anisotropic hyperfine interactions. Due to this mixing the forbidden transitions become partially allowed.

The absolute values of the two nuclear transition frequencies ω_α and ω_β associated with the electron spin states $m_s = +1/2$ and $m_s = -1/2$ can be expressed as

$$\omega_\alpha = |\omega_{12}| = \left[\left(\frac{A}{2} - \omega_I \right)^2 + \left(\frac{B}{2} \right)^2 \right]^{1/2} \quad \{17\}$$

$$\omega_\beta = |\omega_{34}| = \left[\left(\frac{A}{2} + \omega_I \right)^2 + \left(\frac{B}{2} \right)^2 \right]^{1/2}$$

The allowed (ω_{13} , ω_{24}) and the forbidden (ω_{23} , ω_{14}) electron transition frequencies are given by

$$\begin{aligned}\omega_{13} &= \omega_s - \frac{\omega_-}{2} \\ \omega_{24} &= \omega_s + \frac{\omega_-}{2}\end{aligned}\tag{18}$$

and

$$\begin{aligned}\omega_{14} &= \omega_s - \frac{\omega_+}{2} \\ \omega_{23} &= \omega_s + \frac{\omega_+}{2}\end{aligned}\tag{19}$$

in which $\omega_+ = \omega_\alpha + \omega_\beta$, $\omega_- = \omega_\alpha - \omega_\beta$.

The coefficients A and B in equation {13} are proportional to the components of the local magnetic field generated by the electron on the nucleus parallel and perpendicular to the direction of the external magnetic field respectively. For an axially symmetric hyperfine and an isotropic \mathbf{g} tensor, assuming that the magnetic field B_0 is along the z -axis and the nucleus lies in the xz -plane of the laboratory coordinate system A and B are related to the principal values A_{\parallel} and A_{\perp} of the hyperfine tensor by

$$\begin{aligned}A &= A_{\parallel} \cos^2 \theta + A_{\perp} \sin^2 \theta = A_{iso} + T(3 \cos^2 \theta - 1) \\ B &= (A_{\parallel} + A_{\perp}) \sin \theta \cos \theta = 3T \sin \theta \cos \theta\end{aligned}\tag{20}$$

where θ is the angle between the vector connecting the nuclear and electron spins and the external magnetic field, A_{iso} denotes the isotropic hyperfine constant and T represents the hyperfine dipolar coupling constant T .

The transition probabilities for the allowed (I_a) and forbidden (I_f) EPR transitions are represented by

$$I_a = \cos^2 \left[\frac{(\varphi_\alpha + \varphi_\beta)}{2} \right] \quad I_f = \sin^2 \left[\frac{(\varphi_\alpha + \varphi_\beta)}{2} \right]\tag{21}$$

with $\sin \varphi_\alpha = B / \omega_\alpha$ and $\sin \varphi_\beta = B / \omega_\beta$

From these expressions, it follows that the forbidden transition only can take place if the quantity B differs from zero.

Using equation {20} the nuclear transition frequencies ω_α and ω_β can be also expressed as

$$\omega_\alpha = \left[\left(\frac{A_\perp}{2} - \omega_I \right)^2 \sin^2 \theta + \left(\frac{A_\parallel}{2} - \omega_I \right)^2 \cos^2 \theta \right]^{1/2} \quad \{22\}$$

$$\omega_\beta = \left[\left(\frac{A_\perp}{2} + \omega_I \right)^2 \sin^2 \theta + \left(\frac{A_\parallel}{2} + \omega_I \right)^2 \cos^2 \theta \right]^{1/2}$$

A.3.3 The three-pulse ESEEM and HYSCORE experiments

In the following a restriction to the simple $S = 1/2$ and $I = 1/2$ spin system is made in order to describe the pulsed hyperfine spectroscopy.

The three-pulse ESEEM experiment is based on three microwave $\pi/2$ pulses [55-58]. The first two pulses are separated by time interval τ , the third pulse is applied at time T after the second pulse. At time τ after the last pulse a stimulated electron spin echo is observed (Figure 7). In this experiment the amplitude of the stimulated echo is observed as a function of the time T .

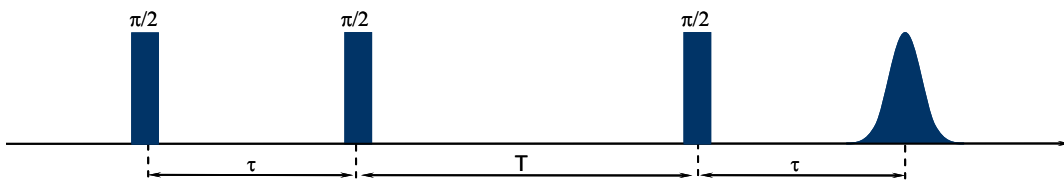


Fig. 7: Pulse sequence for the three-pulse ESEEM experiment.

The nuclear modulation effect in the experiment arises from nuclear coherence. At the start of the experiment the first $\pi/2$ creates electron coherence, after free evolution during the time τ , the second $\pi/2$ pulse creates nuclear coherence. The nuclear coherence evolves within the time T and then the third $\pi/2$ transfers the nuclear coherence back to observable electron coherence.

The modulation formula {23} of the three-pulse experiment is

$$V_{3p}(\tau, T) = 1 - \frac{k}{4} \left\{ [1 - \cos(\omega_\beta \tau)] [1 - \cos(\omega_\alpha (T + \tau))] + [1 - \cos(\omega_\beta \tau)] [1 - \cos(\omega_\beta (T + \tau))] \right\}$$

The coefficient k , determining the modulation frequency amplitude is given by

$$k = 4 \cos^2 \frac{\varphi^+ - \varphi^-}{2} \sin^2 \frac{\varphi^+ - \varphi^-}{2} = \sin^2(\varphi^+ - \varphi^-) = \left(\frac{B \omega_I}{\omega_\alpha \omega_\beta} \right)^2 \quad \{24\}$$

where φ^+ and φ^- for the $m_s = \pm 1/2$ manifolds respectively, determine the direction of the nuclear spin quantization axis, the values of ω_α and ω_β which are proportional to the local magnetic field strength at the nucleus for different projections of m_s . This means as described above that ESEEM appears only if both allowed and forbidden transitions are induced. The coefficient k involves the parameter B , which depends on the nondiagonal elements of the hyperfine tensor hence the ESEEM can only occur when there is an anisotropic hyperfine interaction between the electron and the nucleus i.e. in solids. For isotropic hyperfine coupling as in liquids where $B=0$, the ESEEM vanishes as the forbidden transitions can not take place. The ESEEM modulation also vanishes for an anisotropic hyperfine coupling, at the canonical orientations of a powder spectrum where B_0 is parallel with one of the principal axes of the hyperfine tensor (A_{\parallel} or A_{\perp} for axially symmetric one).

In addition, the modulation depth k is influenced by the nuclear Zeeman frequency, the change of which could be achieved by performing the ESEEM experiment at variable microwave frequencies i.e. variation of the strength of external magnetic field. For weak hyperfine coupling ($\omega_\alpha \approx \omega_\beta \approx \omega_I \gg B$), where k approaches $(B/\omega_I)^2$, the modulation depth increases at lower microwave frequencies i.e. smaller nuclear Zeeman interaction.

In the three-pulse experiment the echo envelope is modulated only by the two basic frequencies ω_α and ω_β , in contrast to the two-pulse experiment where the sum and difference of these frequencies appear. This is usually an advantage as it results in simplified spectra. Advantage of the three-pulse ESEEM experiment is that the spectral resolution is limited by the phase memory time (T_{2n}) of the nuclear spins, which is longer than the T_{2e} . Consequently the lines are narrower and therefore the resolution is better than in the two pulse ESEEM experiment.

A disadvantage of this experiment is that the three-pulse ESEEM spectra are subject to blind spots caused by the delay time τ between the first two pulses. As it can be seen from the modulation formula, the suppression effect on the modulation is due to the dependence of the amplitudes of the nuclear frequencies ω_α and ω_β on $\omega_\alpha\tau$ and $\omega_\beta\tau$ respectively. The blind spots occur at $\tau=2\pi n/\omega_\alpha$ and $\tau=2\pi n/\omega_\beta$ ($n=0,1,\dots$). On the other hand, in some cases the blind spot behavior can be used as an advantage, and use to suppress strong matrix peaks for example ($\tau=2\pi n/|\omega_I|$, $n=0,1,\dots$).

In the three-pulse ESEEM experiment three Hahn echoes and one refocused echo are generated in addition to the stimulated echo. For short τ and T values these additional echoes cross the stimulated echo leading to distortions of the signal. Therefore a proper phase cycle is required to avoid this problem [55,69].

The hyperfine sublevel correlation (HYSCORE) experiment is a four-pulse 2D-version of the ESEEM experiment [70-75]. In this experiment the first two $\pi/2$ pulses are again separated by a time interval τ . At a time t_1 after the second pulse, a π pulse is applied. The subsequent time t_2 is followed by another $\pi/2$ pulse and an electron spin echo is again observed at time τ after the last pulse (Figure 8). The time intervals t_1 and t_2 are varied independently, which results in two dimensional time-domain dataset.

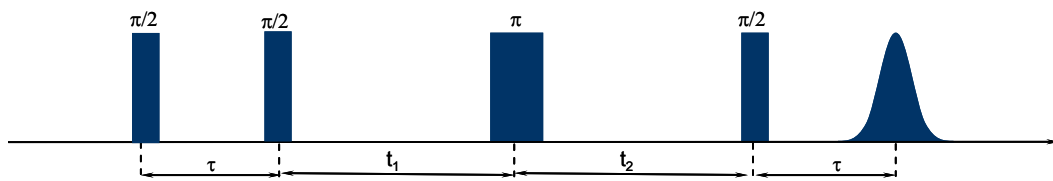


Fig. 8: Pulse sequence for the HYSCORE experiment.

In this experiment nuclear coherence created by the first two pulses evolves firstly within the time t_1 , then the mixing π pulse interchanges the nuclear coherence between the α and β electron spin manifolds, followed by a second free evolution for the time t_2 , and finally the nuclear coherence is transferred to electron coherence by the last $\pi/2$ pulse. Since the HYSCORE experiment is based on an evolution of nuclear coherence in two dimensions the spectral resolution is enhanced.

The modulation formula for the HYSORE experiment is

$$V_{4p}(\tau, t_1, t_2) = \frac{1}{2}[V^\alpha(\tau, t_1, t_2) + V^\beta(\tau, t_1, t_2)] \quad \{25\}$$

$$V^\alpha(\tau, t_1, t_2) = 1 - \frac{k}{2} \left[\frac{C_0}{2} + C_\alpha \cos\left(\omega_\alpha \left(t_1 + \frac{\tau}{2}\right)\right) + C_\beta \cos\left(\omega_\beta \left(t_2 + \frac{\tau}{2}\right)\right) + C_c \left(c^2 \cos\left(\omega_\alpha t_1 + \omega_\beta t_2 + \omega_+ \frac{\tau}{2}\right) - s^2 \cos\left(\omega_\alpha t_1 + \omega_\beta t_2 + \omega_- \frac{\tau}{2}\right) \right) \right]$$

$$V^\beta(\tau, t_1, t_2) = 1 - \frac{k}{2} \left[\frac{C_0}{2} + C_\alpha \cos\left(\omega_\alpha \left(t_2 + \frac{\tau}{2}\right)\right) + C_\beta \cos\left(\omega_\beta \left(t_1 + \frac{\tau}{2}\right)\right) + C_c \left(c^2 \cos\left(\omega_\alpha t_2 + \omega_\beta t_1 + \omega_+ \frac{\tau}{2}\right) - s^2 \cos\left(\omega_\beta t_1 + \omega_\alpha t_2 - \omega_- \frac{\tau}{2}\right) \right) \right]$$

$$C_0 = 3 - \cos(\omega_\beta \tau) - \cos(\omega_\alpha \tau) - s^2 \cos(\omega_+ \tau) - c^2 \cos(\omega_- \tau)$$

$$C_\alpha = c^2 \cos\left(\omega_\beta \tau - \omega_\alpha \frac{\tau}{2}\right) + s^2 \cos\left(\omega_\beta \tau + \omega_\alpha \frac{\tau}{2}\right) - \cos\left(\omega_\alpha \frac{\tau}{2}\right)$$

$$C_\beta = c^2 \cos\left(\omega_\alpha \tau - \omega_\beta \frac{\tau}{2}\right) + s^2 \cos\left(\omega_\alpha \tau + \omega_\beta \frac{\tau}{2}\right) - \cos\left(\omega_\beta \frac{\tau}{2}\right)$$

$$C_c = -2 \sin\left(\omega_\alpha \frac{\tau}{2}\right) \sin\left(\omega_\beta \frac{\tau}{2}\right)$$

with $\omega_+ = \omega_\alpha + \omega_\beta$, $\omega_- = \omega_\alpha - \omega_\beta$ and $k=4s^2c^2$.

The factors s^2 and c^2 ($s^2 = I_f = \sin^2(\delta/2)$ and $c^2 = I_a = \cos^2(\delta/2)$) are the forbidden and allowed transition probabilities for the system, and are given by

$$s^2 = \frac{|\omega_I^2 - 1/4(\omega_\alpha - \omega_\beta)^2|}{\omega_\alpha \omega_\beta}, \quad c^2 = \frac{|\omega_I^2 - 1/4(\omega_\alpha + \omega_\beta)^2|}{\omega_\alpha \omega_\beta} \quad \{26\}$$

where δ is the angle between the two effective magnetic field of the two $m_s = \pm 1/2$ states at the nucleus.

A Fourier transformation of the 2D time-domain HYSORE dataset result in cross peaks at frequencies $(\omega_{12}, \omega_{34})$ and $(\omega_{21}, \omega_{43})$ because nuclear coherence, which had evolved with frequencies ω_{12} or ω_{34} during time t_1 , evolves with frequencies ω_{21} or ω_{43} during time t_2 .

In case of weak hyperfine coupling $|A| < 2|\omega_I|$, a pair of cross peaks $(\omega_\alpha, \omega_\beta)$, $(\omega_\beta, \omega_\alpha)$ is observed in the first quadrant ($++$). For the strong coupling case $|A| > 2|\omega_I|$, the cross peaks $(\omega_\alpha, -\omega_\beta)$, $(\omega_\beta, -\omega_\alpha)$ are predominantly in the second quadrant ($-+$). For the intermediate case of “exact cancellation condition” i.e. the hyperfine interaction is in the magnitude of the nuclear Zeeman splitting $|A| = 2|\omega_I|$, the cross peaks may appear in both quadrants with similar intensity. The first two cases are schematically represented in Figure 9.

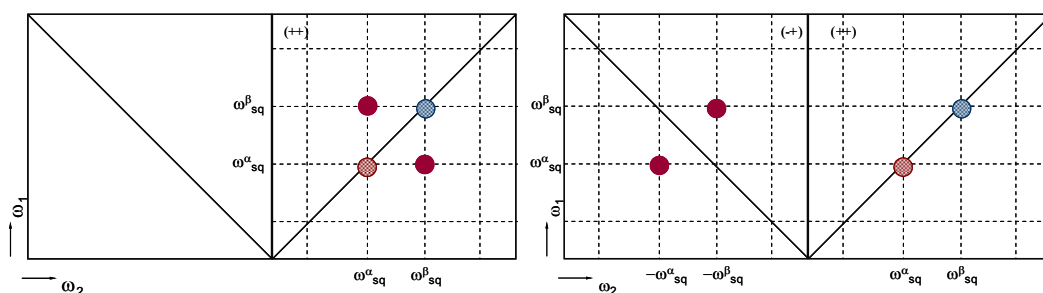


Fig. 9: Schematic representation of the HYSORE spectra ($\omega = 2\pi\nu$). In the weak coupling regime (left) and in the strong coupling regime (right). Full circles correspond to the off-diagonal cross correlation peak pairs. The peaks on the diagonal are due to incomplete inversion of the electron spin echo by the π pulse.

The appearance of the cross correlation peaks with different intensity, in different quadrants as dependant on the hyperfine interaction introduces additional spectral information and reduces spectral overlap between strongly coupled nuclei with small gyromagnetic ratios and weakly coupled nuclei with large gyromagnetic ratios. The main advantage of the HYSORE experiment in comparison with the three-pulse ESEEM is the correlation of the nuclear frequencies of the α and β electron spin manifolds. The HYSORE experiment could be very helpful in unraveling complicated spectra with overlapping lines even from nuclei with similar gyromagnetic ratios and comparable hyperfine coupling as the cross peak correlate the nuclear transition frequencies associated with electron spin manifolds which belong to the same nucleus.

It also has some disadvantages, for example in practice the π pulse might be not strong enough and could not always achieve complete inversion, thus the nuclear coherence evolves at the same transition during both evolution periods. As a result a diagonal peaks $(\omega_\alpha, \omega_\alpha)$, and $(\omega_\beta, \omega_\beta)$ appear in the HYSORE spectrum and especially

for small hyperfine couplings these peaks are very close to the off diagonal cross peaks and thus may disturb the analysis. The HYSCORE also suffers from blind spots and the experiments have to be performed with different τ values to recover all nuclear transition frequencies and as it is a 2D- experiment it becomes more time consuming in comparison to the three-pulse ESEEM [70-75].

Appropriate phase cycle is also required in the HYSCORE experiment in order to remove the contribution of the unwanted echoes as in the three-pulse ESEEM [55, 69].

A.3.4 Analysis of HYSCORE $S = 1/2, I = 1/2$ spin system

Analysis of the off-diagonal cross correlation peak pair at $(\omega_\alpha, \omega_\beta), (\omega_\beta, \omega_\alpha)$ in the HYSCORE spectrum leads to determination of the hyperfine parameters of the paramagnetic species [76-84].

For an axially symmetric spin system the principal values of the hyperfine tensor \mathbf{A} are $(A_\perp, A_\perp, A_\parallel)$ where $A_\perp = A_{iso} - T$ and $A_\parallel = A_{iso} + 2T$. The nuclear transition frequencies are given by

$$\begin{aligned}\omega_{\parallel\alpha(\beta)} &= -\omega_I \pm \frac{(A_{iso} + 2T)}{2} \\ \omega_{\perp\alpha(\beta)} &= -\omega_I \pm \frac{(A_{iso} - T)}{2}\end{aligned}\tag{27}$$

as follows from eq. {17}.

In the case weak hyperfine interaction the cross peaks in the spectrum are centered near the Larmor frequency of the nucleus such that $(\omega_\alpha + \omega_\beta)/2 \approx \omega_I$ can be used to identify the nucleus. The hyperfine coupling constant of the nucleus can be estimated using the relation $(\omega_\alpha - \omega_\beta) \approx A$. Peaks that appear along the diagonal are due to weakly coupled nuclei with $A \approx 0$.

In disordered paramagnetic samples the cross correlation peaks in the HYSCORE spectrum became ridged. The powder line shape is a narrow, curved arc extending from $(\omega_{\parallel\alpha}, \omega_{\parallel\beta})$ to $(\omega_{\perp\alpha}, \omega_{\perp\beta})$ and $(\omega_{\parallel\beta}, \omega_{\parallel\alpha})$ to $(\omega_{\perp\beta}, \omega_{\perp\alpha})$ respectively (Figure 10).

The hyperfine parameters can be determined from the extensions of the ridges perpendicular to the diagonal. However, this is only rough estimation and in many cases may be not really accurate as the ridges might be not fully resolved i.e. the end

points of the arcs correspond to a depth parameter $k=0$, and only a single orientation ($B_0 \parallel A_{\parallel}$) contributes to the outer end points. Presence of blind spots in the spectrum could be an additional problem for the precise determination.

In such cases the maximum frequency shift from the anti-diagonal at $|\omega_I|$ given by

$$(\Delta\omega_s)_{\max} = \frac{9T^2}{32|\omega_I|} \quad \{28\}$$

could be used to determine precisely the anisotropic hyperfine coupling constant T .

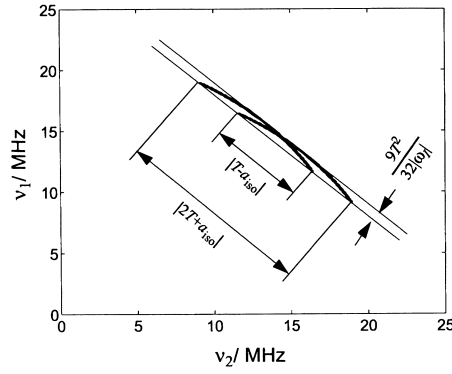


Fig. 10: Schematic representation of HYSCORE powder patter for S=1/2, I=1/2 spin system. The intensity varies throughout the correlation ridges.

The frequency axis along the diagonal is stretched by factor of $\sqrt{2}$ with respect to the ω_α and ω_β axis. In this method of analysis, one has to take in account the effects of orientation selection. Accurate value of $(\Delta\omega_s)_{\max}$ is only obtained when orientation with $\theta=45^\circ$ contribute to the HYSCORE spectrum [77].

Another alternative way of analysis of the HYSCORE spectra had been proposed in ref. [78]. The analytical expression for the contour line form of the HYSCORE pattern is

$$\omega_{\alpha(\beta)}^2 = Q_{\alpha(\beta)\alpha} \omega_{\beta 0}^2 + G_{\alpha(\beta)} \quad \{29\}$$

where

$$Q_{\alpha(\beta)} = \frac{T + 2A_{iso} \mp 4\omega_I}{T + 2A_{iso} \pm 4\omega_I}$$

$$G_{\alpha(\beta)} = \pm 2\omega_I \frac{4\omega_I^2 - 2A_{iso}^2 + 2T^2 - A_{iso}T}{T + 2A_{iso} \pm 4\omega_I}$$

The equation above shows that when $\omega_{\alpha(\beta)}^2$ is plotted versus $\omega_{\beta(\alpha)}^2$ a straight line results with slope of Q_α and the intercept of G_α (or Q_β and G_β) respectively, which can be used to determine A_{iso} and T . Alternatively, the frequencies at the principle values of the hyperfine tensor which occur where the straight line crosses the parabola defined by $(\omega_\alpha + \omega_\beta = 2\omega_I)$ can be used as well. The advantage in this way of analysis is that, in principle the slope and the intercept can be determine in spectra with blind spots and in cases where due to orientation selection only part of the correlation pattern is observed. On the other hand, it could be problematic to use it for systems with more than one nucleus with the same Larmor frequency present as several ridges with similar slopes will be present.

Additionally, precise determination of the hyperfine parameters can be achieved by performing the HYSCORE experiment at different field positions on the EPR spectrum due to orientation selectivity. Especially, experiments performed near the canonical orientations of the g-tensor i. e. single crystal like positions and if the corresponding HYSCORE spectra have enough resolution can be very helpful as the determination of A_{iso} and T there is straight forward. Orientation selective HYSCORE experiments can gain also information about the orientation of the hyperfine tensor in respect to the \mathbf{g} tensor thus providing useful geometrical information about the coordination environment of the paramagnetic species.

A.3.5 Analysis of HYSCORE for $S = 1/2, I > 1/2$ spin system

In the HYSCORE experiment for paramagnetic species where the unpaired electron interacts with nucleus with nuclear spin $I > 1/2$, correlations can arise between any nuclear spin transition of the α electron spin manifold and any nuclear transition of the β electron spin manifold, including nuclear transitions with $\Delta m_I > 1$.

For a nucleolus with $I = 3/2$ three multiquantum nuclear transitions two double-quantum with $\Delta m_I = 2$ and one triple-quantum ($\Delta m_I = 3$), in addition to the three single quantum transitions ($\Delta m_I = 1$) in each electron spin manifold will arise. These transitions are indicated in the corresponding energy level diagram (Figure 11).

This could leads in principle to a complicated HYSCORE spectrum with 36 cross peaks, corresponding to all possible combination of the six nuclear transition frequencies between the two electron spin manifolds.

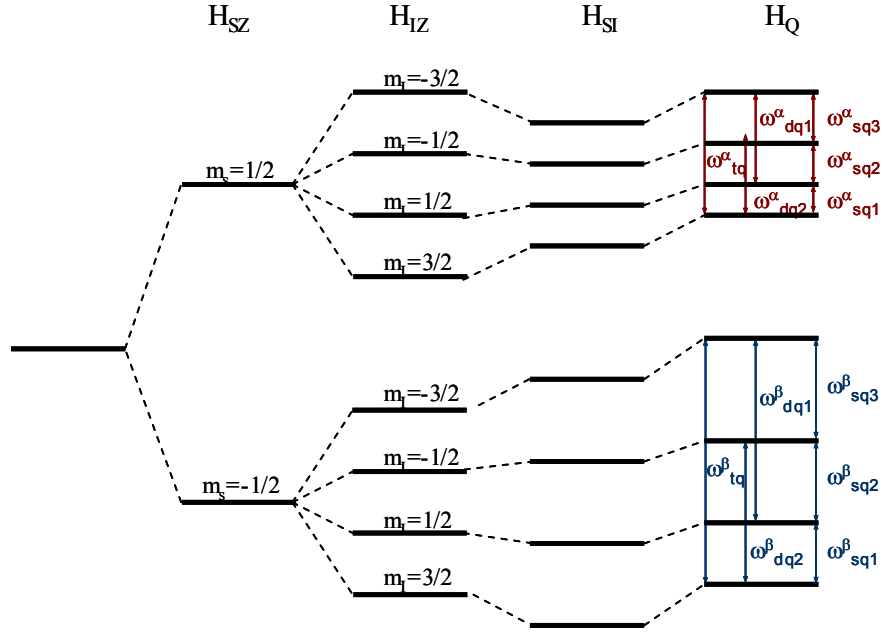


Fig. 11: Energy level diagram for an electron spin $S=1/2$ coupled to a nuclear spin $I=3/2$ in case of $Q < A < \omega_I$, at external magnetic field $B_0=0$. The three single quantum nuclear transitions in each manifold are denoted as $\omega_{sq1,2,3}^\alpha$ and $\omega_{sq1,2,3}^\beta$. The double quantum and triple quantum nuclear transitions in each manifold are denoted as $\omega_{dq1,2}^\alpha$ and $\omega_{dq1,2}^\beta$ and ω_{tq}^α and ω_{tq}^β respectively.

Generally, in practice only few of the possible 36 cross peaks are observed as it had been shown that the larger modulation amplitude belongs to the $\Delta m_I = 1$ and the modulation depth decreases with increasing Δm_I [76, 85-89].

The frequencies of the most pronounced six single quantum transitions at a single orientation, for a magnetic field along one of the principle axes are given by

$$\omega_{sq} = \left[\omega_I \pm \frac{A_i}{2} + \frac{3}{2} Q_i (2m_I + 1) \right] \quad \{30\}$$

where A_i denotes the principle hyperfine tensor values and Q_i denotes the principle values of the \mathbf{Q} tensor along the principle axis, and $m_I = -3/2, -1/2, 1/2$ [55].

The frequencies of the two sq ($m_I = -1/2, m_I = 1/2$) transitions do not depend to first order on the nuclear quadrupole coupling, the same is true for any $(-m_I, m_I)$ transition, however the other transitions with this properties are usually weaker. If the sq ($m_I = -1/2, m_I = 1/2$) dominate the HYSORE spectra, the corresponding analysis is similar to the one for systems with $I=1/2$ [84,88,89]. It has to be noted that this does not hold

for sizeable quadrupole coupling, since second order quadrupole effects distort the line shape and thus the analysis could be not successful.

It had been demonstrated that in the limiting case $|Q_{zz}| < |A_{zz}| < |\omega_I|$ the maximum frequency shift $(\Delta\omega_s)_{\max}$ from the anti-diagonal at $|\omega_I|$, applicable for $I = 1/2$ could be used to extract the hyperfine parameters from the HYSORE spectra of systems with nuclear spin $I = 3/2$ [76, 86,87].

The ^{33}S hyperfine splitting has been determined from the HYSORE spectrum obtained for coenzyme M reductase. This splitting is in the strong coupling regime ($|A| > 2|\omega_I|$) and the quadrupole interaction is negligible compare to it. Therefore, the hyperfine tensor principal values have been extracted from the frequencies corresponding to the triple quantum transition which are thus to first order independent of the nuclear quadrupole interaction [90].

In cases where the nuclear quadrupole, the hyperfine and the nuclear Zeeman interactions are of the same order of magnitude, as it could be in a case for weakly coupled nuclei only a numerical computation of the full spin Hamiltonian can reproduce the HYSORE spectrum.

A.3.6 EPR spectroscopy on the Mo(V) state of molybdenum enzymes

Variety of biophysical techniques have been applied on the molybdenum enzymes providing information on the structures of molybdenum center and the catalytic mechanism of these enzymes, in many cases even after the determination of the three dimensional structures by X-ray crystallography, as some questions remained still open.

EPR spectroscopy is a well-established method for studying paramagnetic centers in enzymes. It has been one of the extensively used techniques to investigate the coordination of molybdenum centers in molybdenum enzymes despite that Mo(V) ($S = 1/2$) is the only biologically accessible paramagnetic oxidation state of the metal [4,11]. The Mo(V) state usually exists in the enzymes in equilibrium with both the oxidized Mo(VI) and the reduced Mo(IV) states. Mo(V) generally arises during enzyme turnover as a result not of primary reaction of substrate with the molybdenum center, but because of subsequent one electron transfer to or from the other redox

centers. It is typical for molybdoenzymes that no more than about 30% of the metal can be converted to the Mo(V) state. [4, 11].

Molybdenum occurs naturally in a variety of isotopes of which ^{95}Mo and ^{97}Mo have a nuclear spin ($I = 5/2$) with a combined natural abundance of $\sim 25,5\%$ (^{95}Mo : 15,9% and ^{97}Mo : 9,6%). This fact can be used to unequivocally assign EPR spectra (Figure 12), as these isotopes will result in a strong anisotropic hyperfine coupling characteristic for molybdenum [11, 91].

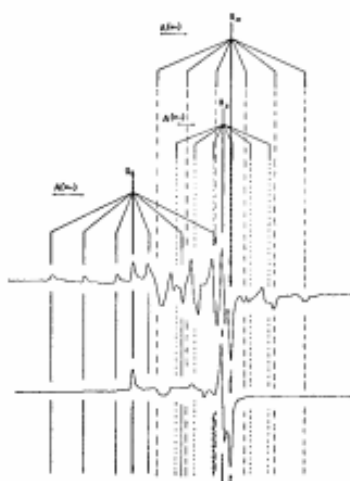


Fig. 12: The molybdenum electron spin resonance signal from xanthine oxidase: normal enzyme (lower trace) and ^{95}Mo enriched enzyme [91].

Further more, it has been shown on diverse range of structurally characterized inorganic Mo(V) model complexes that the average \mathbf{g} tensor value g_{av} is sensitive to the covalency of the metal-ligand bond and therefore to the nature of the ligands. In addition spin-orbit coupling influences the \mathbf{g} tensor anisotropy (Δg), depending on the symmetry of the metal coordination sphere. Hence, detailed analysis of EPR spectra can provide valuable information on the ligand sphere of the Mo(V) state. The ligand symmetry and the covalency of the ligand bonds also influence the hyperfine tensor of the ^{95}Mo and ^{97}Mo isotopes [92-96].

Ligands in the first and second coordination sphere of the metal center can often be directly identified via their hyperfine coupling. This has been demonstrated for ^{17}O , ^{31}P , ^{13}C and ^{33}S nuclei in the first coordination sphere and for ^1H and ^2H in the second coordination sphere of molybdenum. The anisotropic and isotropic parts of these hyperfine tensors gave valuable information on the structural arrangement of these ligands in the complex [97-107]. These studies contributed most importantly in the

understanding the structures and catalytic mechanisms of molybdenum enzymes by comparison of their EPR parameters with those found for inorganic complexes.

In the pioneer works on milk xanthine oxidase, continuous wave (CW) EPR have been used extensively to probe the ligand environment of the Mo(V) paramagnetic species, together with appropriate substitution with stable isotopes. The observed hyperfine coupling between the molybdenum unpaired electron in Mo(V) state and the magnetic nuclei introduced yielded unambiguous information about the nature of the Mo(V) coordination sphere of the various Mo(V) EPR signal giving species from xanthine oxidase [11]. CW-EPR has been also used to obtain structural and mechanistic information on the molybdenum centers in many enzymes of the DMSO reductase family, for example formate dehydrogenase, nitrate reductase and DMSO reductase [108-112].

For small hyperfine couplings, normally not resolved in the CW-EPR spectra of disordered frozen solution samples, pulsed hyperfine experiments such as electron spin echo envelope modulation (ESEEM), hyperfine sublevel correlation spectroscopy (HYSCORE) and electron nuclear double resonance (ENDOR) are required. ESEEM and pulsed ENDOR have been used to investigate the exchangeable protons of different forms of the Mo(V) center in chicken liver sulfite oxidase in H₂O and D₂O, in order to establish their hydroxyl/water coordination structures [113-117]. ¹⁷O HYSCORE spectroscopy has been performed also on the sulfite oxidase to study the oxygen trafficking in the catalytic cycle of this molybdenum enzyme [118, 119]. Important structural information about the Mo(V) site in DMSO reductase was obtained from the hyperfine interaction of the exchangeable proton of the hydroxyl ligand using ESEEM and HYSCORE spectroscopy and applying ²H isotope labeling [120].

Finally, in order to distinguish between hyperfine and g-tensor interactions multifrequency EPR can also be applied. This approach has been used extensively on xanthine oxidase and other molybdenum containing hydroxylases to distinguish differences in the coordination spheres of the metal in its Mo(V) states [121-126].

A.4 Results and discussion

Psr from the anaerobic bacterium *W. succinogenes* catalyses the reduction of polysulfide to sulfide. This enzyme contains molybdenum which appears to serve as direct electron donor to or acceptor from the respective substrates. It has been postulated that the molybdenum in the catalytic centre of Psr alternates between the oxidation states IV, V and VI during turnover [6, 25]. Hence, various redox agents have been used to either oxidize or reduce the enzyme. Consequently, the frozen solution samples of Psr have been investigated using different multifrequency CW and pulsed EPR techniques.

A.4.1 CW-EPR

A.4.1.1 Identification of Mo(V) in Psr

The CW-EPR spectrum of the signal giving species for a frozen solution of Psr treated with sodium dithionite together with the corresponding simulation are depicted in Figure 13 (13A and 13B respectively).

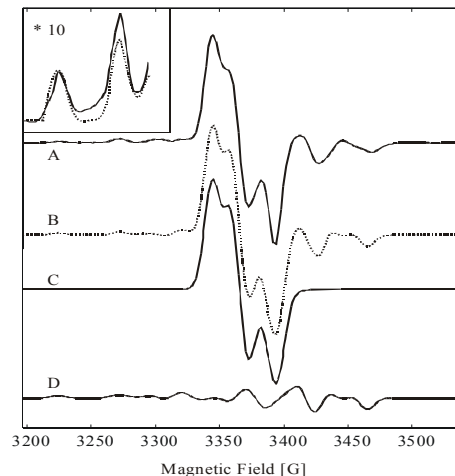


Fig. 13: Mo(V) X-band CW EPR signal of Psr, after reaction with sodium dithionite (state *Very-High-G*) measured at 120 K. The experimental spectrum (A) is shown as a solid line and the simulation of this spectrum (B) as dotted line. For a better understanding of the experimental spectra and how they are made up, the simulations for the different Mo isotopes (with (C) and without (D) Mo hyperfine coupling) are shown separately below. The insert shows the two outermost Mo hyperfine lines on an enlarged scale.

Despite the fact that the spectra is centered at a very low magnetic field i.e. having an unusually high g_{av} value, the signal can be assigned quantitatively and unequivocally to a Mo(V) species due to the specific hyperfine peaks arising from the ^{95}Mo and ^{97}Mo isotopes with a nuclear spin $I = 5/2$. These lines are best resolved at the low

field edge of the EPR-spectra and are enlarged in the insert in Figure 13. The simulation of the overall EPR signal reproduces the natural isotope abundance ratios of Mo (^{96}Mo : 74.6%, $^{95}\text{Mo}/^{97}\text{Mo}$: 25.4%). The contributions to the overall spectra from Mo isotopes without and with nuclear spin are disentangled in Figure 13C and 13D for illustration. The Mo hyperfine coupling could be satisfactorily simulated with a hyperfine tensor $A_{\text{Mo}}=(20, 20, 50)$ G.

A.4.1.2 Different Mo(V) states in Psr

Three Mo(V) species with different spectroscopic properties were observed, depending on preparative conditions and their EPR parameters have been analyzed by numerical simulation. Their EPR spectra are represented together with the respective simulations in Figure 14. Typically, 20% of the metal could be converted to the Mo(V) paramagnetic state.

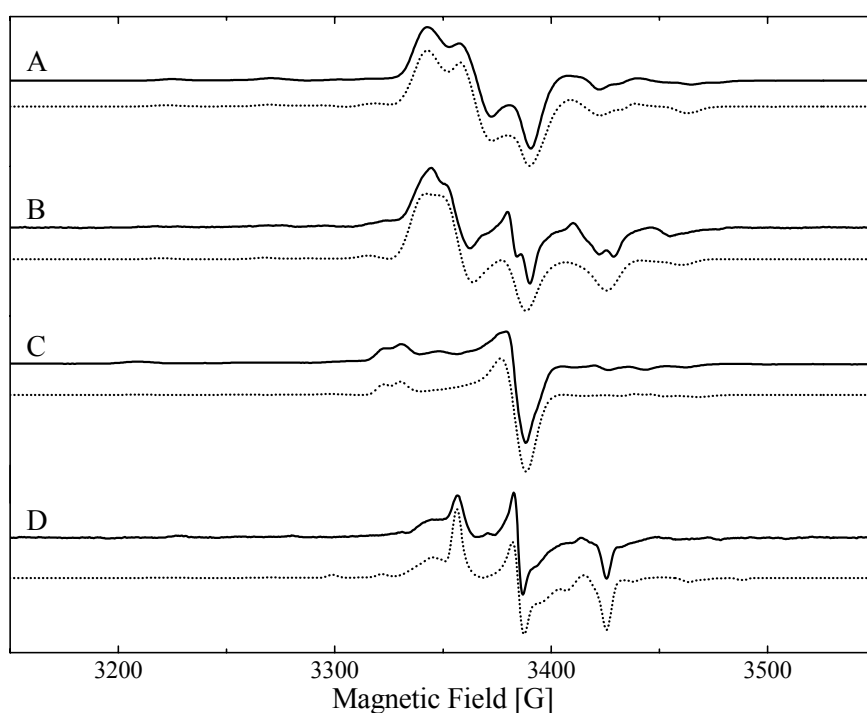


Fig. 14: X-band CW EPR signals of different Mo(V) species: A) *Very-High-G*, B) *Very-High-G/Sud*, C) *Very-High-G/split*, D) *High-G*. Solid lines: experimental spectra measured at 120 K. Other experimental conditions: mw frequency 9.43 GHz, mw power of 2 mW, modulation amplitude of 2 to 0.5 G, and modulation frequency of 100 kHz. Dotted lines: simulations of the experimental spectra with the simulation parameters given in Table 1.

These three states, called *Very-high-G*, *Very-high-G/split*, *High-G*, can be distinguished by their G-tensor values which are summarized in Table 1.

Table 1: G-Tensor values of the observed Mo(V) species in Psr. Error is ± 0.001 for all G-tensor absolute values.

State (preparation)	g_{av}	ΔG $*10^{-3}$	g_{xx}	g_{yy}	g_{zz}	Rhombicity ε $=(g_{zz}-g_{yy})/\Delta G$
<i>Very-High-G</i> (polysulfide)	2.0021	291	1.9874	2.0025	2.0165	0.47
<i>Very-High-G/Sud</i> (polysulfide+Sud)	2.0024	280	1.9872	2.0049	2.0152	0.36
<i>Very-High-G/split</i> (borohydride)	2.0023	355	1.9905	1.9905	2.0260	1
<i>High-G</i> (Na ₂ S)	1.9889	405	1.9675	1.9911	2.0080	0.43

Very-High-G:

This signal was observed for preparations of Psr with an excess of the substrate polysulfide (Figure 14A and Table 1) but could also be generated by incubation of Psr samples with the reducing agent sodium dithionite (Na₂S₂O₄) (see Figure 13). The g_{av} value of these spectra is among the highest observed for Mo-enzymes.

For preparations with the coenzyme Sud present, the same signal is observed for high concentrations of the substrate polysulfide (2mM), whereas for lower concentrations of polysulfide (300 μ M) a slight change in ΔG was observed. The spectra and G-tensor values of this preparation, labeled *Very-High-G/Sud* are shown in Figure 14B and Table 1.

Very-High-G/split:

This Mo(V) species with a strongly altered G-tensor anisotropy (ΔG) and rhombicity ε , defined as

$$\varepsilon = \frac{g_{zz} - g_{yy}}{\Delta G}$$

was observed for the Psr enzyme incubated with sodium borohydride (NaBH₄) (Figure 14C and Table 1). The g_{av} value is unaltered for this species with respect to the *Very-High-G* state, but the rhombicity ε of the G-tensor has changed to an axial G-tensor. An additional splitting is observed on the low-field (g_{zz}) peak of the spectra. This splitting arises from an additional hyperfine interaction to the Mo(V), as can be shown by the field independence of this splitting. Multifrequency EPR measurements performed at S- (3 GHz), X- (9 GHz) and Q-band (34 GHz) frequencies for this

preparation are shown in Figure 15. The spectra can be simulated with the G-tensor given in Table 1 and an additional hyperfine splitting of $A=(2, 2, 8)$ G.

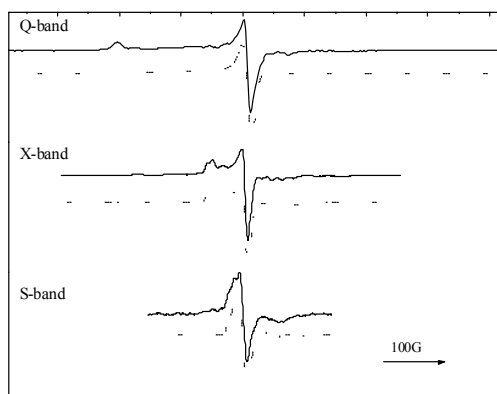


Fig. 15: Multifrequency CW EPR spectra (Q-, X-, S-band) of Psr incubated with borohydride (*Very-High-G/split*). The simulations at all frequencies are performed with an additional hyperfine splitting of 8 G. For the simulation of Q-band spectrum a slightly larger line width (7 versus 4G) was used. The Q-, S-band spectra were taken by F. MacMillan and A. Weber.

High-G:

Finally a further Mo(V) species was identified, most clearly observable for samples incubated only with Na₂S. For this signal the g_{av} is lower with respect to the *Very-High-G* species described above by $\delta g_{av} \approx 0.015$. Nevertheless even this g_{av} value is still rather high compared to most Mo(V) species reported in the literature. Contributions from this species were observable for many of the described preparations, most visible at the high-field edge of the experimental spectra (see Figure 14D). It was observed that this signal increased for samples after numerous short partial freeze/thaw cycles.

A.4.1.3 Comparison with other enzymes and model compounds

The observed *Very-high-G* Mo(V) species have g_{av} values unusually high as compared with previously observed molybdenum enzymes, similar only to *Very-High-G* states of periplasmatic and assimilatory nitrate reductases [108, 122] and formate dehydrogenase [123-125]. For all these enzymes it is known from X-ray crystallography of the Mo(IV) state of the enzyme, that the Mo center is coordinated to four equatorial dithiolene sulfur atoms from a pair of MGDs and to another sulfur atom from a cysteine residue. Accordingly the unusually high g_{av} value of the Mo(V) states of these enzymes is attributed to the large number of sulfur ligands. An increase of the g_{av} value by exchanging an oxygen to a sulfur ligand of Mo(V) ions has been

experimentally and theoretically thoroughly investigated [110, 96, 126] and is mainly due to the covalency of the metal-ligand bonds. Both, the g_{av} and the ΔG values are very similar for these states, as can be seen in Figure 16. The ratio of these two values is correlated to the coordination symmetry of the metal complex, hence the nature and structure of the ligands in Psr should be very similar to nitrate reductase and formate dehydrogenase.

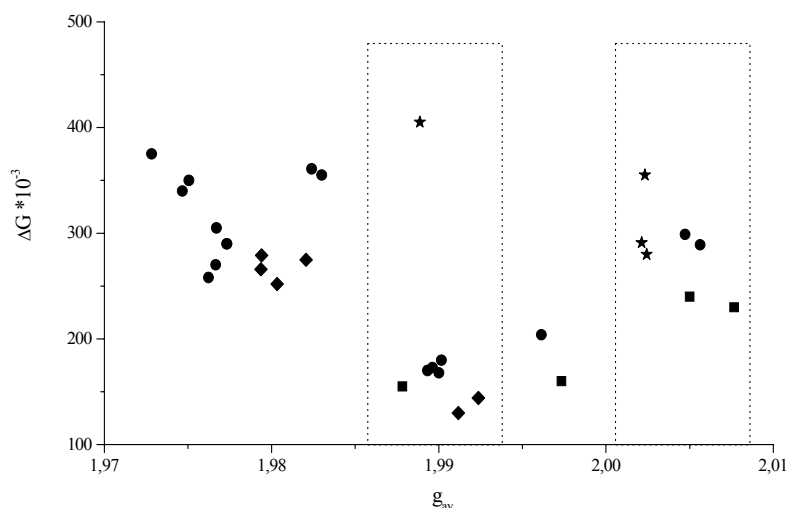


Fig. 16: Correlation of the G-tensor anisotropy ΔG with the average G-tensor value g_{av} for some observed Mo(V) states of the DMSO reductase family. ★: polysulfide reductase, ●: nitrite reductase, ■: formate dehydrogenase, ◆: DMSO reductase. The two dotted boxes enclose the *High-G* states (left box) and *Very-High-G* (right box). The three *Very-High-G* states of Psr are (ordered by increasing ΔG): *Very-High-G/Sud*, *Very-High-G*, *Very-High-G/split*. The DMSO state in the *High-G* box belongs to the mutant S147C, the two states between the two boxes belong to cyanide inhibited enzymes.

The difference of the g_{av} values between the *Very-high-G* species and the *High-G* species observed in Psr matches exactly the value δg_{av} expected for an exchange of oxygen to a sulfur ligand found as described above [96]. The same change in g_{av} has been observed in DMSO reductase for a site directed mutation Ser147→Cys [14]. Consistent with the expected 5 sulfur ligands, the g_{av} value of this mutant is very close to the g_{av} value of the *High-G* species observed in nitrate reductase, formate dehydrogenase and Psr. In all these enzymes it is possible to switch between the two states *Very-high-G* and *High-G* by addition of redox agents or substrate. In Psr the *High-G* signal could be quantitatively converted to the *Very-High-G* signal by addition of sodium dithionite.

The nature of the sixth ligand to the Mo(V) in *Very High-G* states is less clear from EPR spectroscopy. X-ray structures of the Mo(IV) or Mo(VI) states of nitrate reductase, formate dehydrogenase and DMSO reductase show one oxo ligand for

these states. For all these enzymes direct ligation of the substrate to the molybdenum via an oxygen atom is discussed for the Mo(V) transition state. The possibility of having an oxygen ligand of the *High-G* state exchanged to a sulfur ligand in the *Very-High-G* state to explain the shift in g_{av} is discussed for nitrate reductases and formate dehydrogenase, but not favored because of the better agreement of 5 sulfur ligands with EXAFS measurements [108]. Structural changes of the Mo(V) ligand sphere, which can change not only ΔG , but also the g_{av} value [96], are postulated to account for the observed change in g_{av} .

In contrast to the *Very High-G* state in Psr, an additional hyperfine coupling of approximately 6 G is observed for the *Very-High-G* states in nitrate reductases and formate dehydrogenase [108,123]. This coupling is attributed to indirect coupling to a proton, therefore an OH is assumed in both cases as the sixth ligand. No such additional hyperfine coupling is observed in Psr for the *Very-High-G* and *Very High-G/Sud* spectra.

An additional hyperfine splitting is only observed on the g_{zz} edge of the *Very-High-G/split* state of Psr. The experimental conditions to create this state are less clear; only after long incubation at room temperature with excess of borohydride (and possible contact with oxygen) could spectra with an almost axial symmetry be observed. The resolved hyperfine interaction may arise from an SH or from an OH ligand.

Finally, the *High-G* state has a g_{av} value similar to the reported value for the S147C mutant of DMSO reductase, and the *High-G* states of nitrate reductase and formate dehydrogenase [11, 123]. We therefore assume that this species has a similar coordination sphere (5 sulfur ligands), as described above. The Mo hyperfine pattern observable for the *Very-High-G* species (see Figure 13) is not well resolved for this state (Figure 14C), indicating dynamic or static heterogeneity of this state. The anisotropy of the G tensor (ΔG) is much larger in Psr, as compared to these other enzymes. Its position in the diagram of Figure 15 is exactly on the correlation line expected for square pyramidal configuration geometry, implying a highly symmetric arrangement of the two MGDs in the equatorial ligand plane. It accumulates only after extended measurement times with repeated freeze-thaw cycles, but can be converted back to the *Very-High-G* signal as described above. This may be an indication that this state is not directly involved in the native catalytic reaction and consists of inactive proteins trapped in a Mo(V) side reaction state.

A.4.1.4 Effect of Sud

Although a slight change in ΔG for the *Very-High-G/Sud* state was already obtained by fitting of the X-band spectra it could be much better resolved by Q-band EPR measurements as shown in Figure 17. In this case the change of ΔG could directly be determined from the spectra. The same parameters were obtained for the X-band and Q-band simulations.

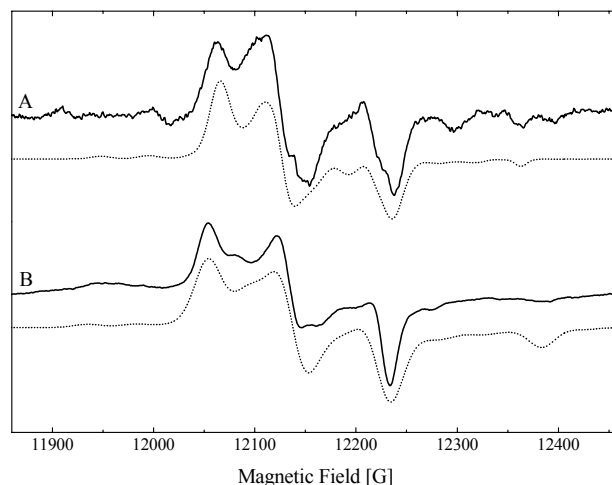


Fig. 17: Q-band EPR spectra of Psr after treatment with polysulfide: A) with Sud, (*Very-High-G/Sud*) B) without Sud (*Very-High-G*). The experimental spectra are shown as solid lines and the simulations with parameters described in Table 1 are shown as dotted lines.

Interestingly, as can be seen from table 1, the G-tensor asymmetry ΔG of the *Very-High-G* state in Psr is slightly altered by the addition of the coprotein Sud (for low concentrations of polysulfide). The function of this coprotein is known from other studies to decrease the Michaelis constant of the PSR at concentrations of polysulfide substrate lower than 100 μM [32]. MALDI mass spectroscopy has shown that the polysulfide substrate binds specifically to a cysteine residue (Cys109) of the Sud protein [31] and NMR spectroscopy has been used to solve the structure of the Sud dimer and to study its specific interaction surface with Psr upon binding [33]. In this bound complex state the transfer of sulfur from polysulfide to the active site of Psr is postulated to occur. The lowering of the Michaelis constant may be due to different aspects of the interaction of Sud on the catalytic cycle (or some combination of them): a) Sud could more efficiently collect polysulfide and guide the substrate to the active site of Psr, b) Sud could increase the contact time between substrate and active center

and therefore the probability of the forward reaction taking place, and c) Sud could lower the activation energy for the transition state via its interaction with the protein. The altering of ΔG and of the rhombicity ε for the *Very-High-G* state due to the Sud coprotein could be caused by a slight change in the geometry of the Mo(V) ligand sphere. This would imply a binding of the Sud protein to Psr close to the Mo center for the *Very-High-G/Sud* state. If the change in the electronic properties of the Mo center caused by the Sud protein also affects the polysulfide affinity as described above or is only a result of a steric interaction between Psr and Sud without influence on the catalytic rate constants has still to be investigated by stopped-flow experiments under turnover conditions. In any case, we believe that the effect of the Sud coprotein on the *Very-High-G* state indicates that this state is involved in the native catalytic reaction cycle of Psr. In this case sulfur from the transferred polysulfide could become the sixth ligand to the Mo and explain directly the very high g_{av} value of the *Very High-G* state and the shift δg_{av} with respect to the *High-G* state.

Finally, on the basis of the EPR parameters obtained here i.e. the observed shift of the g_{av} value between the different Mo(V) states in Psr and by comparison with other molybdo-enzymes, like nitrate reductase, formate dehydrogenase and DMSO reductase, structure for the observed the *Very-High-G* Mo(V) state was proposed (Figure 18).

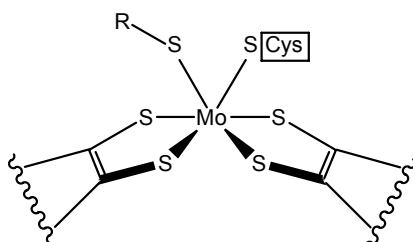


Fig. 18: Proposed structures for the observed Mo(V) *Very-High-G* state in Psr. R could be polysulfide chain or H.

As describe above, the influence of the coprotein Sud on the *Very-High-G* state (*Very-High-G/Sud*) i.e. the alteration of ΔG for this state after binding of Sud to Psr leads to the assumption that this state is an active state in the catalytic reaction of Psr and strongly suggests that sulfur from the substrate polysulfide is directly ligated to the Mo in this state.

A.4.1.5 ^{33}S labeled polysulfide

To prove that sulfur from the polysulfide substrate is the sixth ligand of the Mo(V) in the *Very-High-G* state polysulfide was labeled with ^{33}S . The idea was that ^{32}S has a nuclear spin $I = 0$ showing no hyperfine interaction with the unpaired electron on the molybdenum center whereas ^{33}S has a nuclear spin of $I = 3/2$ leading to a hyperfine splitting, which might be observable in the CW EPR spectrum.

The CW EPR spectra of Psr with ^{33}S labeled polysulfide and with polysulfide containing the natural abundant ^{32}S isotope are shown in Figure 19.

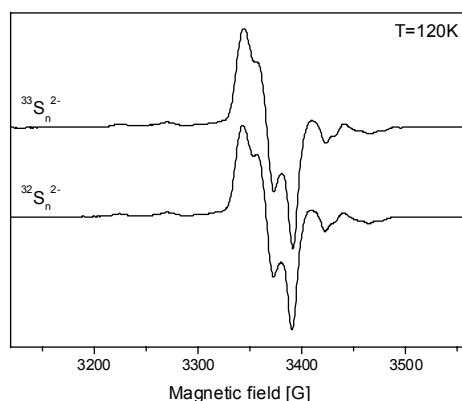


Fig. 19: X-band CW EPR spectra of the Mo(V) *Very-high G* state of Psr generated with ^{33}S isotope labeled and not labeled polysulfide. Experimental conditions: $T=120\text{ K}$, mw frequency of 9.43 GHz , mw power of 2 mW , modulation amplitude of 0.5 G , and modulation frequency of 100 kHz .

The CW EPR spectrum with the ^{33}S labeled polysulfide does not reveal any additional splitting or line broadening compared to the ^{32}S polysulfide spectrum. The reason for this could be that the ^{33}S hyperfine coupling is too small to be resolved at the line width of 6 G . This is not surprising since ^{33}S has a very small g_n of 0.429 leading even at high spin densities at the sulfur to a small hyperfine coupling constant.

A.4.2 Pulsed EPR experiments

If the sulfur hyperfine coupling is indeed small it could be possible to resolve it in pulsed hyperfine experiments. In a first step a field swept two-pulse electron spin echo spectrum was acquired to identify the field positions corresponding to the principle values of the Mo(V) G-tensor. Figure 20 shows the obtained spectrum at 20 K with the corresponding field positions marked by dashed lines. The additional

broad signals beneath the molybdenum arise from the paramagnetic iron-sulfur centers also present in the enzyme. They have long enough T_m at a temperature of 20K and are thus detectable.

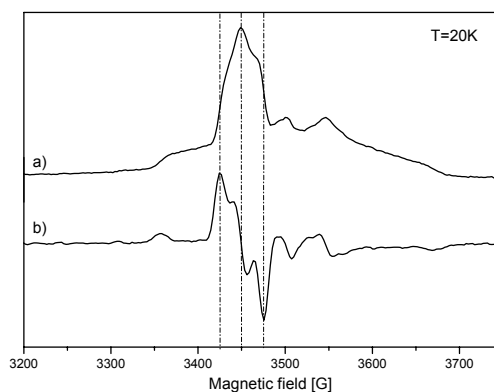


Fig. 20: a) Two-pulse echo detected field swept spectrum of the Mo(V) *Very-high G* state of Psr. b) the first derivative spectrum. Experimental conditions: temperature 20K, mw frequency = 9.68 GHz, mw pulses of length $t_{\pi/2} = 8$ ns and $t_{\pi} = 16$ ns respectively, $\tau = 200$ ns, repetition rate 1 kHz. The dashed lines indicate the principle values of the Mo(V) G-tensor.

A.4.2.1 Three-pulse ESEEM

The three-pulse ESEEM spectra with unlabeled and ^{33}S labeled polysulfide were recorded at the maximum signal intensity of the EPR spectrum. In order to avoid blind spots in the spectra caused by the τ suppression effect a series of three-pulse ESEEM traces were taken using different pulse separation time τ (Figure 21).

The time domain spectra of both samples reveal a superposition of slow and fast modulations due to hyperfine interactions. However, the time domain spectrum with ^{33}S labeled polysulfide (top trace) clearly displays an additional slow echo modulation if compared to the unlabeled polysulfide (bottom trace). This strongly indicates that a sulfur nucleus is coupled and thus indeed close to the molybdenum center in the Mo(V) *Very High-G* state of Psr.

The fast modulation present in both samples arises from coupling of protons to the molybdenum, while the slow modulation is caused by the interaction with another type of nuclei with small nuclear Larmor frequency such as nitrogen. Since this modulation is observed in both samples it could originate from the molybdopterin nitrogens. On the other hand, considering the contributing signal from the FeS centers it could as well be due to nitrogens of amino acids nearby the FeS clusters.

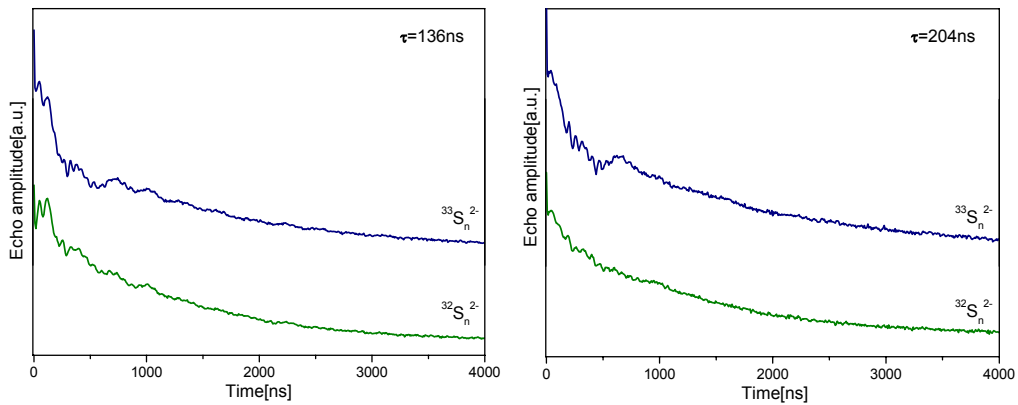


Fig. 21: Time domain three-pulse ESEEM spectra of the Mo(V) *Very-high G* state of Psr generated with ^{33}S isotope labeled and unlabeled polysulfide. The experiments were performed at $T = 20\text{K}$ with $\tau = 136\text{ ns}$ (left panel) and $\tau = 200\text{ ns}$ (right panel). Other experimental parameters: mw frequency = 9.68 GHz, mw pulses of length $t_{\pi/2} = 16\text{ ns}$, repetition rate 1 kHz, time increment $\Delta T = 8\text{ ns}$ (512 intervals), 40 scans were taken.

The corresponding frequency domain spectra consist of a multiple set of lines in the low frequency region (Figure 22). Although the Fourier transformations are sensitive to baseline subtraction in this region, again differences are observed between the labeled and not labeled sample.

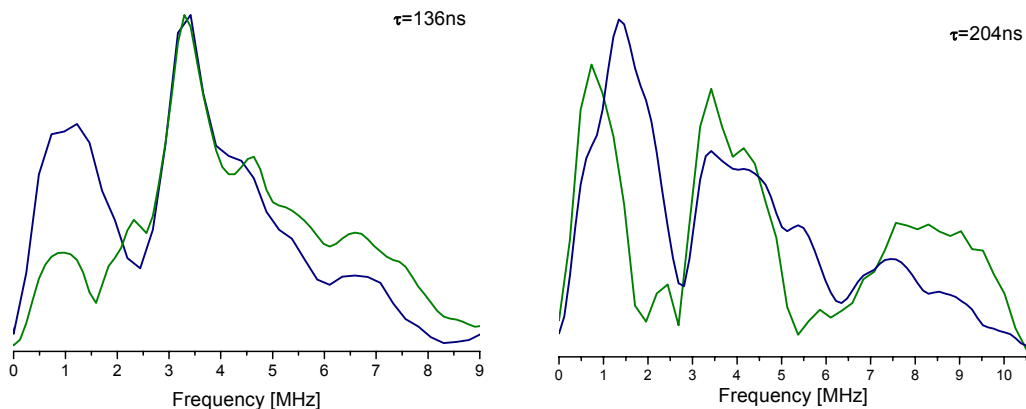


Fig. 22: Frequency domain three-pulse ESEEM spectra of the Mo(V) *Very-high G* state of Psr generated with ^{33}S isotope labeled (blue) and unlabeled polysulfide (green) and with $\tau = 136\text{ ns}$ (left panel) and $\tau = 200\text{ ns}$ (right panel).

The ^{33}S containing sample reveals additional spectral features together with changes in the intensity of the lines in the frequency range of 0 – 3 MHz. Since the main differences are observed in the low frequency region near the sulfur Larmor frequency of 1.14 MHz it is a further indication for a weak hyperfine coupling between the sulfur nuclear spin and the molybdenum electron spin. Experiments at other field positions with the ^{33}S labeled sample showed no significant change of the frequency

and intensity of the peaks. The reason that the expected orientation selectivity was not observed could be due to the numerous overlapping lines from sulfur and nitrogen nuclei.

Although the three-pulse ESEEM shows a difference in presence of ^{33}S labeled polysulfide the effect is relatively small i.e. the depth of the echo modulation due to the sulfur nucleus is small. The situation is even more complex also because the sulfur nuclear frequencies in the spectral region of interest overlap with many other lines. Therefore unambiguous assignment of the frequencies corresponding to the sulfur nuclear transitions is not possible based on the three-pulse ESEEM spectra.

A.4.2.2 HYSCORE

As mention above although differences between labeled and not labeled samples are observed, it is difficult to interpret the one-dimensional (1D) ESEEM spectra due to the overlap of lines. As it was described in the introduction a possibility to simplify the analysis is to use two-dimensional (2D) techniques like HYSCORE.

In particular, HYSCORE allows separating overlapping peaks since it correlates the nuclear transitions of one electron spin manifold with the nuclear transitions of the other electron spin manifold belonging to same nucleus. These correlations between the corresponding nuclear transition frequencies appear in the spectrum as a symmetric off-diagonal cross peaks. In addition, it also enhances the signal to noise ratio by the second Fourier transformation in the second dimension.

Bearing these advantages in mind the HYSCORE experiment was applied on the Mo(V) *Very-high G* state of Psr in order to unravel the complex spectra observed in the three-pulse experiments.

The X-band HYSCORE spectra of Mo(V) samples prepared with ^{33}S isotope labeled polysulfide and polysulfide containing the natural abundant ^{32}S sulfur isotope at the field position corresponding to g_{yy} are presented in Figure 23. The HYSCORE spectrum with ^{33}S labeled polysulfide clearly shows pairs of strong cross-peaks at low frequencies which are absent in the unlabeled sample. Hence these cross peaks can be attributed only to a ^{33}S nucleus magnetically interacting with the Mo(V) unpaired electron (Figure 23A). The observation of cross correlations between the ^{33}S nuclear transition frequencies in the HYSCORE experiment is unambiguous evidence that a sulfur nucleus from the polysulfide substrate is in close vicinity to the molybdenum active site in Psr.

The additional spectral features in the frequency range 3 - 5 MHz observed in both samples originate from nitrogen nuclear transitions. Their frequencies are close to the typical frequency from peptide nitrogens (maximum modulation frequency of ~ 4.5 MHz) observed in X-band ESEEM spectra of ferredoxin clusters and hence can be attributed to the interaction of those types of nitrogens with the FeS centers in Psr.

The intense peak on the diagonal at a frequency of about 15 MHz close to the Larmor frequency of protons originates from distant protons weakly coupled to the molybdenum center (matrix protons). The off-diagonal ridges situated symmetrically with respect to the proton Larmor frequency result from hyperfine couplings of the Mo(V) unpaired electron spin with nearby protons (most probably exchangeable protons).

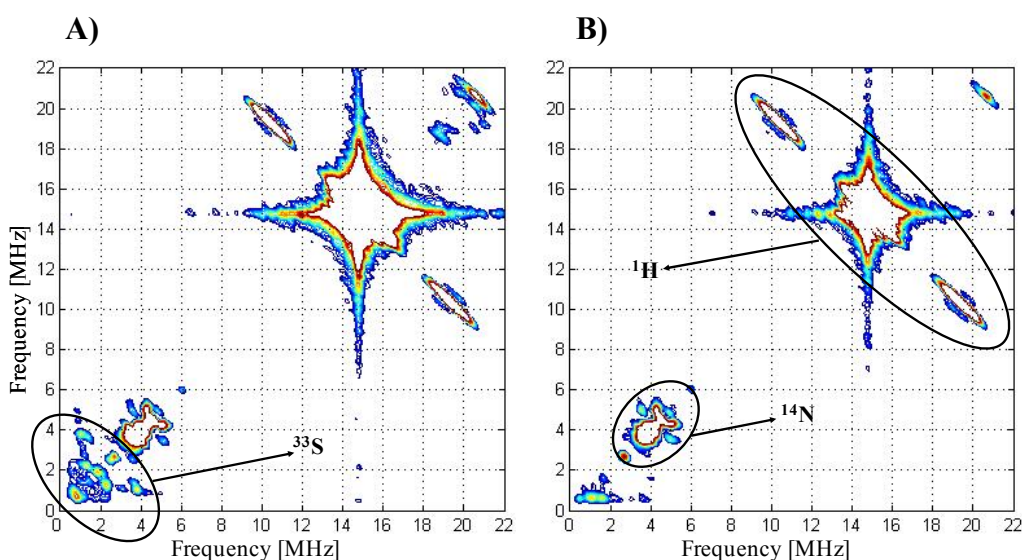


Fig. 23: HYSORE spectra of the Mo(V) *Very-high G* state of Psr generated with A) ^{33}S isotope labeled and B) unlabeled polysulfide. Only the (++) quadrant is shown. The spectra are taken at a field position corresponding to g_{yy} of the Mo(V) with $\tau = 136$ ns. Other experimental parameters: $T = 20\text{K}$, magnetic field is $B_0 = 3450$ G, mw frequency = 9.68 GHz, mw pulses of length $t_{\text{mw}2} = 12$ ns and $t_{\pi} = 24$ ns, repetition rate 1 kHz, time increments $\Delta t_1 = 20$ ns, $\Delta t_2 = 20$ ns (200×200 data points), 1 scans was taken, accumulation time $\sim 20\text{h}$.

As describe in the introduction, the ESEEM frequencies are related to the hyperfine and quadrupole parameters. Therefore this information can be extracted from the HYSORE spectra by appropriate assignment of the nuclear transition frequencies belonging to ^{33}S and by consecutive analysis. In principle, qualitative analysis of the nuclear transition frequencies observed in the HYSORE can provide preliminary estimate for the ^{33}S hyperfine and nuclear quadrupole parameters. These approximate

parameters can be useful starting values for the numerical simulation of the experimental spectra, where in a second step further refinement is achieved.

The experimental HYSCORE spectrum with ^{33}S labeled polysulfide recorded at the g_{yy} of Mo(V) for pulse separation time $\tau = 204\text{ns}$ is represented in Figure 24.

The most intense cross peaks are at frequencies of (1.2, 2.2) MHz and (-1.3, 2.2) MHz in the (++) and (-+) quadrant, respectively, which most probably correspond to the correlation between the $m_I = 1/2 \leftrightarrow -1/2$ single quantum nuclear transitions i.e. (sq^2_{α} , sq^2_{β}). These peaks are with splitting of 1 MHz and width of ≈ 0.6 MHz perpendicular to the diagonal. Additional cross correlation features with lower intensity are also resolved and will be discussed later on.

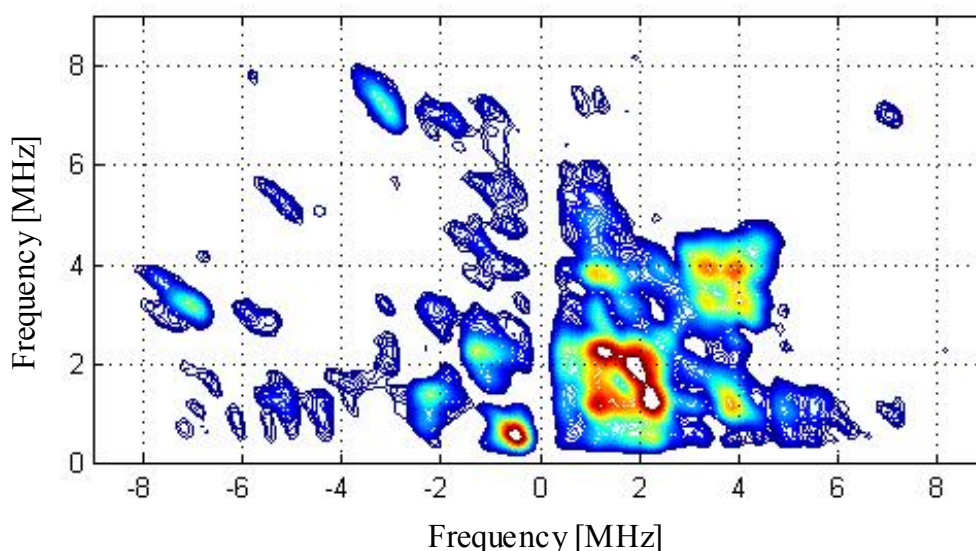


Fig. 24: ^{33}S HYSCORE spectra obtained at g_{yy} of Mo(V) with $\tau = 204$ ns. The (-+) and (++) quadrants are shown. Magnetic field $B_0 = 3450$ G, mw frequency = 9.68 GHz, $T = 20\text{K}$. Other experimental parameters: mw pulses of length $t_{p2} = 12$ ns and $t_p = 24$ ns, repetition rate 1 kHz, time increments $\Delta t_1 = 20$ ns, $\Delta t_2 = 20$ ns (200×200 data points).

The assignment of the $m_I = 1/2 \leftrightarrow -1/2$ nuclear transitions corresponding to the cross peaks with frequencies (1.2, 2.2) MHz is the least questionable. As expected these transitions have the largest intensity in all spectra since they are least affected by the nuclear quadrupole interaction [84, 88, 89, 119]. Their frequencies to first order are given by $\omega = \omega_I \pm A/2$, where ω_I is the ^{33}S Zeeman frequency and A is the secular component of the hyperfine interaction. Hence, the value of A estimated from the HYSCORE spectra obtained at the g_{yy} position of the EPR spectrum is ≈ 1 MHz. Note

that the half sum of the frequencies of these correlation peaks does not coincide with ω_I (it is shifted by 0.56 MHz). This implies that the estimated value of A may be affected by second-order effects of the nuclear quadrupole interaction. The above analytical expression is strictly valid at the canonical orientations of the G-tensor and its applicability could be questionable at this field position (g_{yy}) where many different orientations of the molybdenum center contribute. Therefore, numerical simulations with complete diagonalization of the spin Hamiltonian is necessary for more accurate estimates as shown and discussed later on. Nevertheless, the appearance of the signals from ^{33}S in both quadrants of the HYSCORE spectrum expected for intermediate coupling case $A \approx 2\omega_I$ sets an upper limit for the ^{33}S hyperfine coupling. In summary, the positions and intensity of the cross peaks indicates on a qualitative level that the size of the ^{33}S hyperfine coupling lies in weak to intermediate regime.

A.4.2.2.1 Orientation dependence

HYSCORE measurement at different field positions on the anisotropic Mo(V) spectrum selects molybdenum centers with different orientations of the effective G-tensor relative to the external magnetic field B_0 (the width of the anisotropic Mo(V) EPR spectrum is 100G which significantly exceeds the spectral interval excited by microwave pulses 7G). Ideally, the spectra taken at the high and low extreme edges near the maximal and minimal g values give “single-crystal like“ pattern from those centers whose g_{zz} and g_{xx} axes are directed along the magnetic field. The nuclear frequencies of ^{33}S determined from such spectra can provide an estimate of the components of the hyperfine and quadrupole tensors along the g_{zz} and g_{xx} axis in the G-tensor coordinate system. In contrast, the resonance condition at the intermediate g_{yy} value is fulfilled by many different, yet well defined orientations. Therefore, to estimate the principle components of the hyperfine and nuclear quadrupole tensor the HYSCORE measurements were performed at several field positions of the EPR spectrum. The corresponding HYSCORE spectra recorded at different field positions under the same experimental conditions are presented in Figure 25 and 26. Anisotropy of the ^{33}S hyperfine and quadrupole coupling is observed as can be seen from the positions and shapes of the cross peaks.

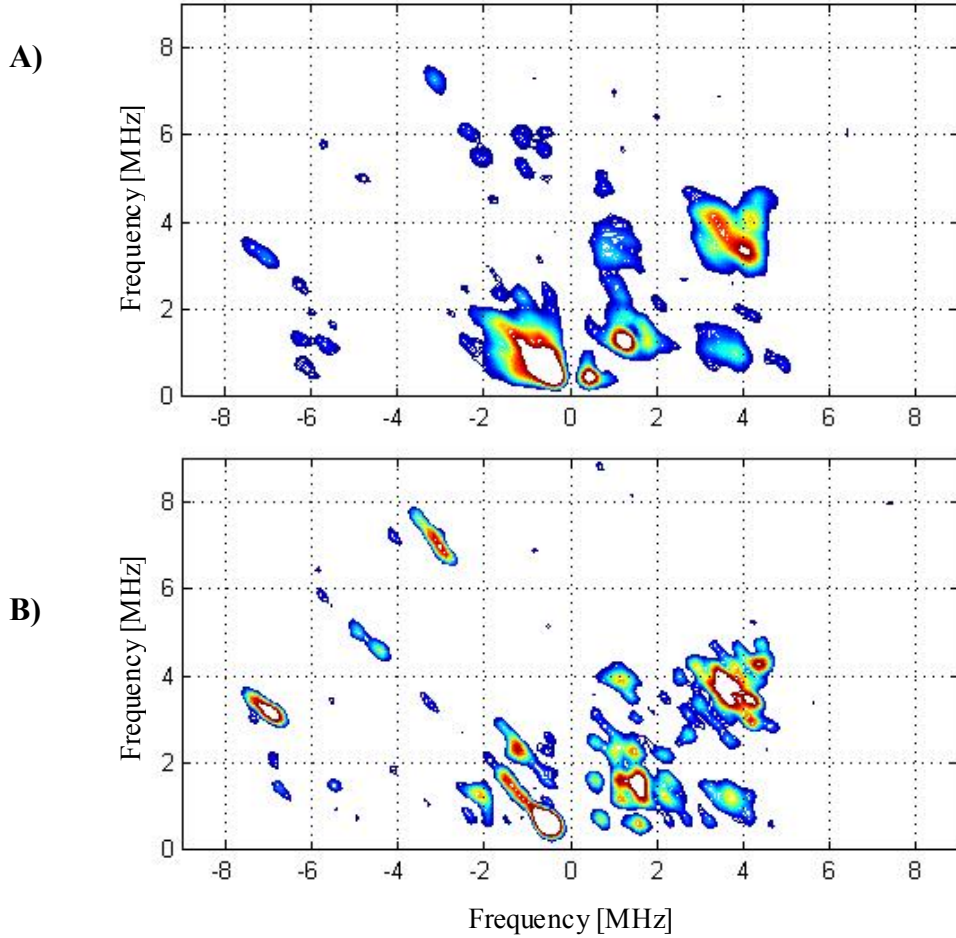


Fig. 25: ^{33}S HYSCORE obtained at observer positions A) $B_0 = 3425$ G (g_{zz}), B) $B_0 = 3437$ G of the Mo(V) EPR spectrum. The (-+) and (++) quadrants are shown. All spectra are taken with $\tau = 204$ ns at 20 K. Other experimental conditions: mw frequency = 9.68 GHz, mw pulses of length $t_{\pi/2} = 12$ ns and $t_{\pi} = 24$ ns, repetition rate 1 kHz, time increments $\Delta t_1 = 20$ ns, $\Delta t_2 = 20$ ns (200×200 data points).

The HYSCORE spectrum recorded at a magnetic field position corresponding to g_{zz} of Mo(V) (Figure 25A) shows a significant decrease in intensity of the cross peaks as expected. It reveals two broad features in the (++) quadrant with frequencies of (1.0, 3.6) MHz. In the (-+) the high frequency peaks are barely resolved and their positions do not change if compared with the spectrum at the middle of the Mo(V) signal. The cross peaks assigned to the single quantum transitions at g_{yy} are not observable here, although a broad feature around 1.7 MHz with length of 2 MHz is visible.

The HYSCORE spectrum at the intermediate field position i.e. between g_{zz} and g_{yy} reveals many cross peaks with comparable intensity (Figure 25B). It still contains the intense peaks with frequencies of (-3.2, 7.1) MHz in the (-+) quadrant. Their positions and length do not change if compared with the spectrum at g_{yy} , however they are much narrower. In the (+) quadrant the pair of cross peaks with coordinates (-1.2,

2.2) MHz are also present. In the (++) quadrant the broad features with frequencies of about (1.15, 3.7) MHz are also detected. Two pairs of cross peaks at (1.0, 2.2) and (1.6, 2.2) are observed as well. Additional pair of correlation close to the frequency axis at (0.5, 1.6) MHz appears in the (++) quadrant.

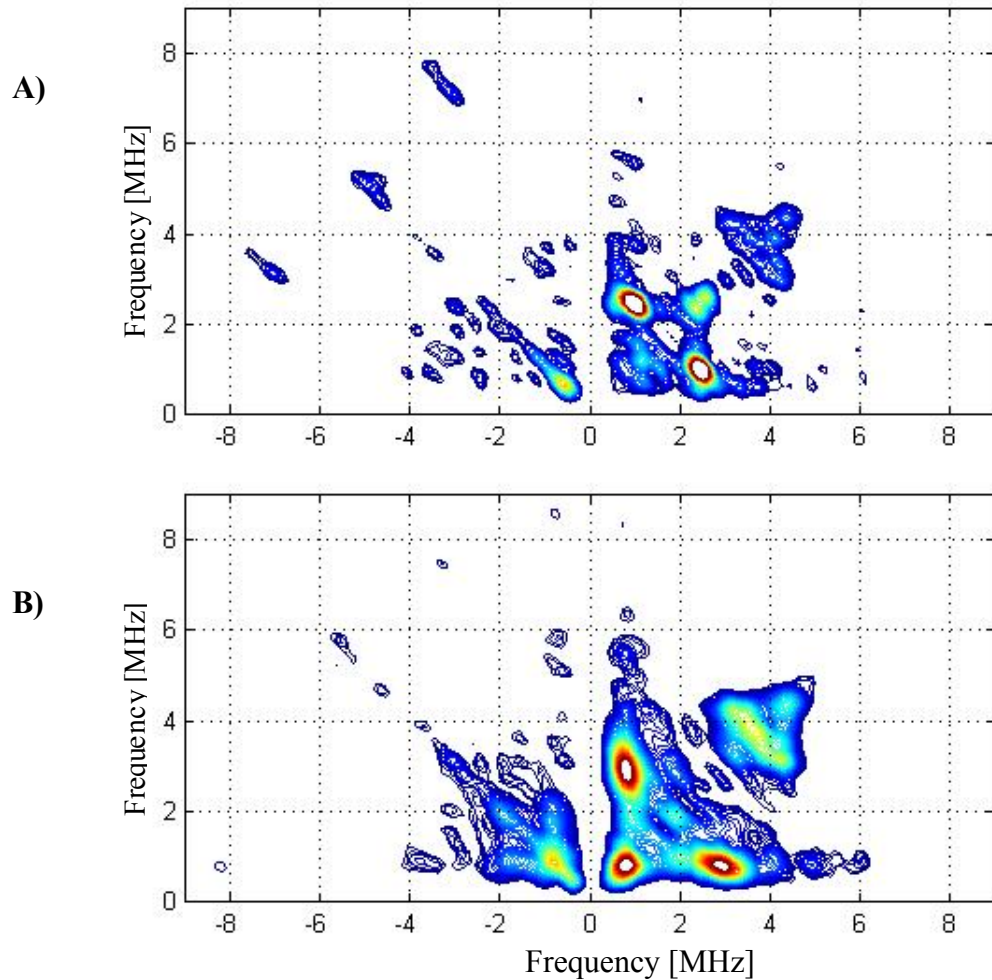


Fig. 26: ^{33}S HYSORE spectra obtained at observer positions A) $B_0 = 3462$ G, B) $B_0 = 3475$ G (g_{xx}) of the Mo(V) signal. The (-+) and (++) quadrants are shown. All spectra are taken with $\tau = 204$ ns at 20K. Other experimental conditions: mw frequency = 9.68 GHz, mw pulses of length $t_{\pi/2} = 12$ ns and $t_{\pi} = 24$ ns, repetition rate 1 kHz, time increments $\Delta t_1 = 20$ ns, $\Delta t_2 = 20$ ns (200×200 data points).

For the orientations between g_{yy} and g_{xx} the high frequency peaks at (-3.1, 7.1) MHz are still observed (Figure 26A), however, with significantly less intensity. Some weak features at lower frequencies are also present in this quadrant. The most prominent ones are with frequencies about (-1.0, 3.6) MHz. In the (++) quadrant strong cross peaks at frequencies (0.95, 2.4) MHz exist. The other main features in the (++) quadrant are no longer resolved, except for weak features close to the diagonal at 1.6

MHz and a weak ridged pattern up to 4 MHz (along 1 MHz in the other frequency direction).

Measurement at the high field edge (i.e. g_{xx}) leads to complete disappearance of the (3.1, 7.1) MHz cross peaks in the (-+) quadrant (Figure 26B). On the other hand a weak pattern in the low frequency range appears. In the (++) quadrant a long ridged pattern, parallel to the frequency axis appears. The most pronounced cross peaks are at frequencies of (0.7, 2.85) MHz. These cross peaks are broad and have remarkably significant intensity which is surprising at this field position.

The assignment of the cross peaks at the “single crystal like” positions corresponding to g_{zz} and g_{xx} of Mo(V) is quite unclear, hence a preliminary estimate of the EPR parameters could not be done. However, it is important to note that the ^{33}S pattern in the HYSCORE spectra for different orientations is very specific.

A.4.2.2.2 Pulse separation time τ dependence

Since the value of the pulse separation time τ which is kept constant in the HYSCORE experiment significantly affects the intensities of the cross-peaks, the corresponding spectrum may not contain all correlation features. To resolve all of them, a series of HYSCORE measurements with different τ values were performed. Signals from ^{33}S appear in both (-,+) and (+,+) quadrants of the HYSCORE spectra. The experimental HYSCORE spectra with ^{33}S labeled polysulfide recorded at the g_{yy} position of Mo(V) are presented in Figure 27.

In all spectra cross-peaks with maxima at (1.15, 3.7) MHz and (1.0, 4.9) MHz are resolved in addition to the ones at (1.2, 2.2) MHz attributed to the (sq^2_{α} , sq^2_{β}) nuclear transitions. They might represent the correlations between single and double quantum transitions i.e. (sq^2_{α} , dq^1_{β}) and (sq^2_{α} , dq^2_{β}) respectively. In the spectrum taken with $\tau = 116\text{ns}$ can be seen that the former cross peak in fact splits into two with frequencies (1.05, 3.7) and (1.4, 3.6) which could correspond to a correlation between (sq^2_{α} , dq^1_{β}) and (sq^3_{α} , dq^1_{β}) the nuclear transitions (Figure 27A). However, they could also be parts of the same ridge.

In the HYSCORE spectrum obtained with $\tau = 288\text{ns}$ additional features at frequency positions (0.5, 2.2) MHz appear which could originate from (sq^1_{α} , sq^2_{β}) transitions. The basic frequencies (1.2, 2.2) MHz and (-1.3, 2.2) MHz are also observable (Figure 27C).

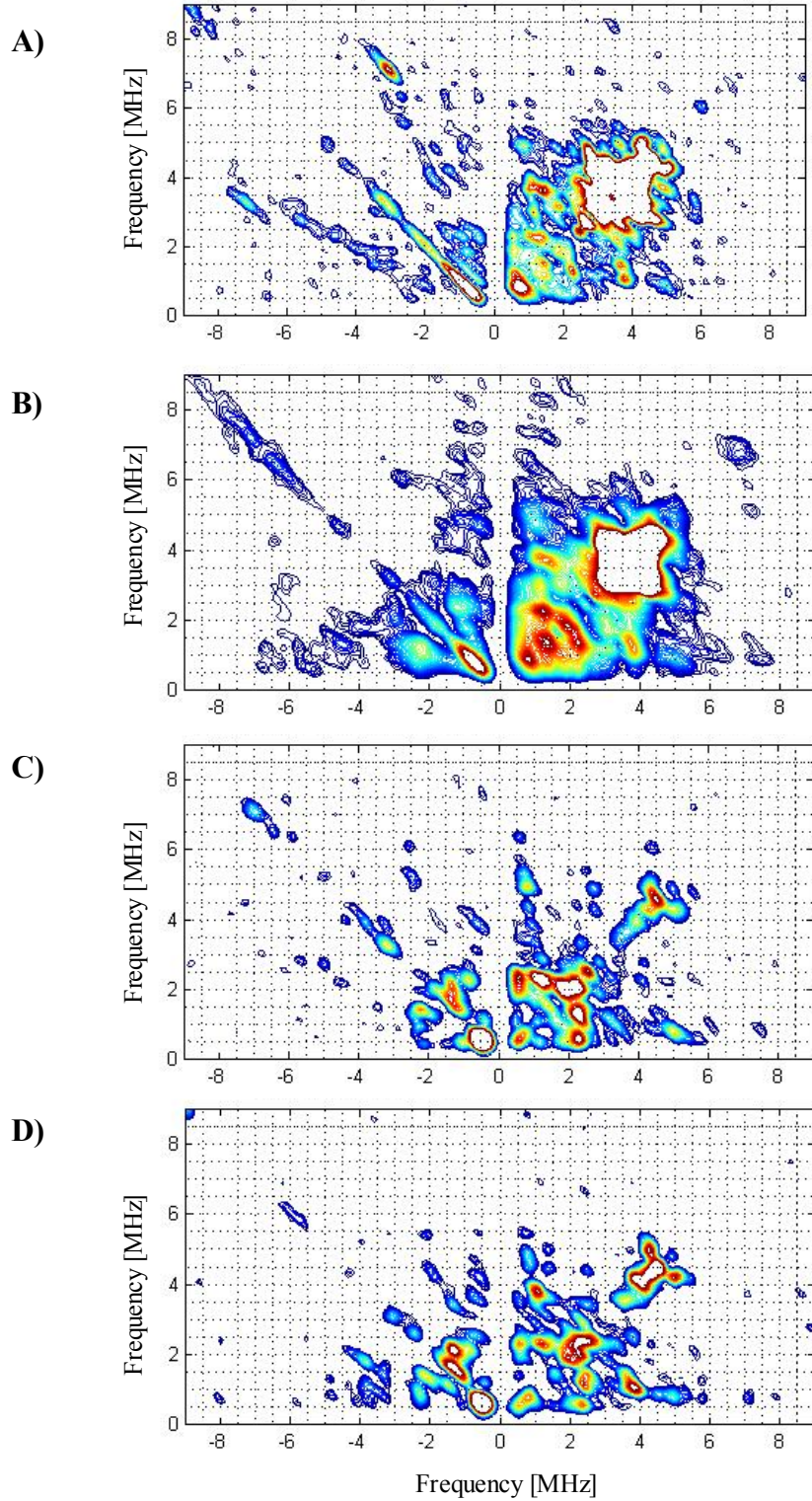


Fig. 27: ^{33}S HYSCORE spectra obtained at g_{yy} of Mo(V) with A) $\tau = 116$ ns, B) $\tau = 136$ ns, C) $\tau = 288$ ns and D) $\tau = 336$ ns. The (-+) and (++) quadrants are shown. Magnetic field $B_0 = 3450$ G, mw frequency = 9.68 GHz, $T = 20\text{K}$. Other experimental parameters: mw pulses of length $t_{\pi/2} = 12$ ns and $t_{\pi} = 24$ ns, repetition rate 1 kHz, time increments $\Delta t_1 = 20$ ns, $\Delta t_2 = 20$ ns (200×200 data points).

Additional cross-peaks at (1, 7.3) MHz with rather weak intensity are observed in the (++) quadrant of the spectrum with $\tau = 204\text{ns}$ (Figure 24). They may represent a correlation between the single and triple quantum transitions.

Finally in the (-,+) quadrant cross peaks that form long narrow ridges parallel to the diagonal with frequencies (-3.2, 7.1) MHz are observed (Figure 27A and Figure 24). These peaks are with splitting of 3.9 MHz and width of $\approx 1\text{MHz}$. As this are the highest frequencies observed it is tempting to assign them to correlation between the triple quantum nuclear transitions i.e. (tq_α , tq_β).

In summary, while the structural information which the spectra contain (at different field positions and τ values) is significant it is rather difficult to extract it directly due to the high spin of ^{33}S , its low gyromagnetic ratio (327Gs^{-1}) and its large quadrupole moment as well as the lack of analytical expressions suitable for this case. More detailed information about the isotropic and anisotropic hyperfine interaction and quadrupole interaction of the ^{33}S nucleus near by the Mo(V) center can be extracted from the experimental data by means of numerical simulations of the HYSORE spectra.

A.4.2.2.3 Quantitative analysis

Systematic simulations showed that the cross peak positions are determined by the isotropic hyperfine coupling, while the width (perpendicular to the diagonal) of the peaks is determined by the anisotropic component of the hyperfine coupling, which was found to be relatively small. Afterwards the optimum values found for the hyperfine tensor were kept fixed and the influence of the quadrupole coupling constant was investigated. As the quadrupole coupling constant increases the cross peaks split into multiple ridges resulting in an apparent broadening of each peak i.e. the ridge patterns are mainly governed by the quadrupole coupling constant.

The best agreement with the experimental spectrum at g_{yy} of Mo(V) for $\tau = 204\text{ns}$ was obtained with an isotropic hyperfine coupling constant of 1.9 MHz. The anisotropic hyperfine coupling constant was estimated to be in the range of 0.4 - 0.7 MHz, which would correspond in a point-dipole approximation to a Mo-S distance with boundaries of 2.05 - 2.48Å. This lie in the range of Mo-S bound found in similar enzymes. The largest component of the quadrupole tensor, Q_{zz} was estimated to be 0.2 MHz. The corresponding simulated HYSORE spectrum is shown in Figure 28.

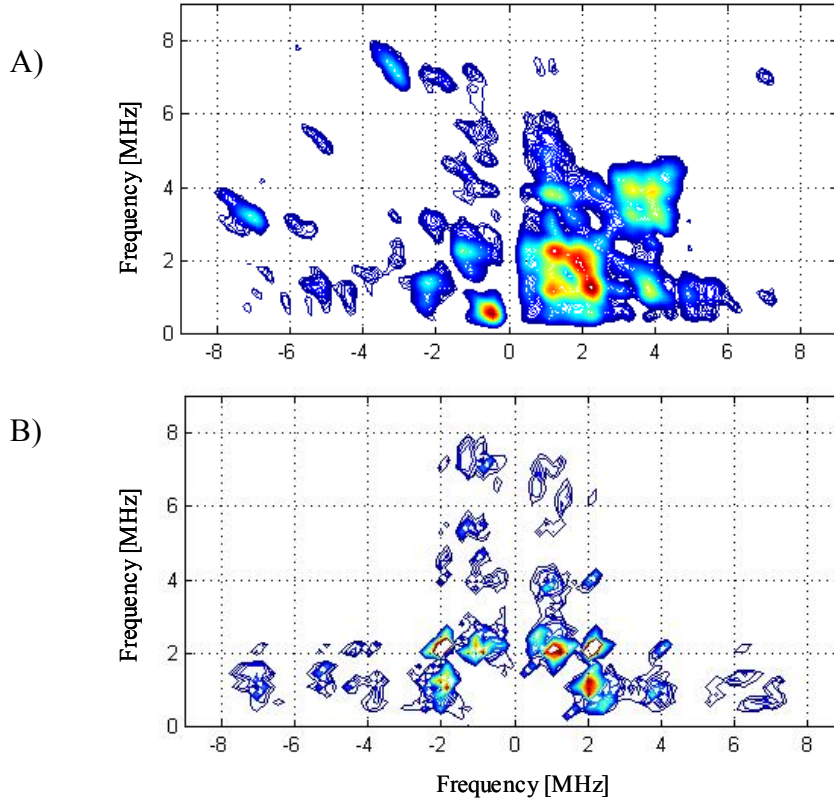


Fig. 28: A) Experimental ^{33}S HYSCORE spectrum at observer position $B_0 = 3475$ G on the Mo(V) signal, corresponding to g_{yy} , pulse separation time $\tau = 204$ ns. B) corresponding simulation. The (-+) and (++) quadrants are shown. The interaction with a ^{14}N nucleus, responsible for the cross peaks with frequencies around 4 MHz, near the diagonal was not included in the simulations.

In comparison to the experimental HYSCORE spectrum the simulated spectrum reproduces rather well both the position and the shape of most of the cross peaks. Only the high frequency features in the (-+) quadrant were not reproduced. The largest mismatch between experiment and simulations occurred at the “single crystal like” the g_{xx} and g_{zz} position where the experimental HYSCORE spectra could not be reproduced well (simulations not shown).

The position and the intensity of the cross-peaks in the HYSCORE spectra not only depend upon the strength of nuclear Zeeman, isotropic and anisotropic hyperfine and quadrupole interactions but also on the relative orientation of the anisotropic hyperfine and quadrupole tensors with respect to the G-tensor frame. The latter effect might not be significant for the g_{yy} position since many orientations contribute there but becomes important at the low and high field positions. In addition, it could affect different spectral features to different extent.

In the simulations shown here the hyperfine and quadrupole tensors were assumed to be collinear to the G-tensor axes system. We made this simplification in order to

reduce the number of variable parameters (eleven if the Euler angles defining the orientation of hyperfine and quadrupole tensors with respect to the G frame are included). The hyperfine tensor and quadrupole tensor at this stage of the simulation were also assumed to be axially symmetric as an additional simplification. It also has to be noted that the molybdenum hyperfine interaction was neglected in the calculated orientation selection used for the simulation of the experimental spectra at different B_0 . However, this may be important especially at the positions near g_{xx} where all three components of the Mo(V) hyperfine tensor contribute. The effect could become significant and hence molybdenum hyperfine interaction has to be taken into account in the future simulations. Further refinement of the hyperfine and quadrupole tensors and even more importantly variation of their orientation in respect to the G-tensor axis system could lead to better agreement with the experimental data for the magnetic field position corresponding to the canonical orientations of the G-tensor.

Finally, despite the simplifications described above, it was not possible to reproduce the positions of the ^{33}S nuclear frequencies with smaller values for the hyperfine coupling, which would account for more distant sulfur nucleus with respect to the molybdenum center. Hence, the sulfur from the polysulfide substrate is indeed bound and thus the sixth sulfur ligand to the molybdenum center in the *Very-High G* state of Psr.

More detailed structural information about the molybdenum active site in Psr could be obtained by further simulations where the simplifications mentioned above are taken into account in combination with DFT calculations in order to correlate the experimental parameters with the molecular structure.

A.5 Summary and Outlook

EPR spectra of the molybdenum centre in polysulfide reductase (Psr) from *W. succinogenes* with unusually high G-tensor values have been observed for the first time. Three EPR spectroscopically different Mo(V) states have been generated by the addition of the substrate polysulfide and other redox agents and were characterized with respect to their G-tensor values (g_{av} , Δg , ϵ) and hyperfine couplings (A_{Mo} , A_H) using multifrequency (S-, X-, Q-band) CW-EPR spectroscopy. The unusually high G-tensor values are attributed to a large number of sulfur ligands. Four sulfur ligands are assumed to arise from two pterin cofactors, one additional sulfur ligand was identified by mutagenesis studies to be a cysteine residue of the protein backbone. For the Mo(V) *Very-High-G* state it is proposed that a sixth sulfur ligand is coordinated to the Mo center, based on the experimentally observed shift of the g_{av} value. This sixth sulfur ligand is postulated to belong to the polysulfide substrate consumed within the catalytic reaction cycle of the enzyme. The influence of the coprotein sulfur transferase (Sud) on the Mo(V) G-tensor supports this assignment.

Modern pulsed EPR techniques in combination with ^{33}S isotope labeling confirmed this hypothesis. In particular, the HYSORE technique allowed the successful detection of ^{33}S nuclear modulation, which had been observed only in one other work till now [90]. The cross correlations of the ^{33}S nuclear transition frequencies observed for the isotope labeled polysulfide, which were absent in the unlabeled polysulfide, allowed to verify that a sulfur nucleus from the polysulfide substrate interacts magnetically with the molybdenum center in Psr. The distance between the Mo(V) center and the ^{33}S nucleus was determined to lie in the range of about 2 to 2.5 Å in agreement with Mo-S distances found in molybdenum enzymes of the same family.

In conclusion, pulsed hyperfine spectroscopy was proven to be an effective technique for the identification of the coordination sphere of metalloenzymes active sites. A comparison between DFT computational studies in progress and the experimental data obtained by pulsed hyperfine spectroscopy can result in a more detailed structure of the active site.

**B) Dipolar Relaxation Measurements on the Cytochrome *c*:CcO
Protein Complexes**

B.1 Goals

The main aim of this work was to obtain structural information of the protein-protein complex between cytochrome *c* oxidase and cytochrome *c* using pulsed EPR methods, which are based on the dipolar interaction between two paramagnetic centers.

The challenge is that both proteins naturally contain metal centers as redox active cofactor groups. Metal ions possess much faster relaxing spins and significantly broader line widths compared to organic radicals. More established methods such as cw-EPR and PELDOR spectroscopy cannot be applied in such cases. Therefore the motivation was to figure out whether relaxation enhancement caused by the dipolar interaction could be used to determine the distances between two metal centers. To evaluate the value of this method for such an application a number of requirements had to be tested and fulfilled:

1. The first step on the way was to observe an enhancement of the Cu_A relaxation in the oxidase due to dipolar coupling with the Fe in the cytochrome, which is an indication that protein-protein complex formation takes place. For this purpose a two-pulse Hahn echo sequence was used to detect the Cu_A transversal relaxation.
2. A crucial point for the quantitative interpretation of the relaxation data was to separate the dipolar relaxation from all other interactions contributing to the Cu_A relaxation.
3. To evaluate the optimum conditions for a 1:1 complex formation, which is mandatory for a quantitative interpretation of the data.
4. The next important step was to demonstrate that the detected relaxation enhancement is caused by a specific complex formation. Therefore three *c*-type cytochromes were used, two of them known to be efficient electron donors to the oxidase in contrast to the third, which cannot transfer electrons since it does not bind to the oxidase and can therefore serve as a control.
5. To find the optimum temperature range where a maximum effect of the dipolar relaxation can be observed. The longitudinal relaxation rate of the fast relaxing spin at this temperature is a measure of the dipolar coupling strength between the two centers. At lower temperatures the decay is only affected by the T₁ relaxation time of the fast relaxing spin while at higher

temperatures the decay is additionally sensitive to distance and relative orientation of the two paramagnetic centers.

6. It was important to test if this method could be used to investigate the protein-protein interaction in more complicated systems i.e. with more than two paramagnetic center involved. The full-size oxidase containing four paramagnetic centers was measured and compared with the results of the smaller system with only two centers.
7. Finally, the last step was to evaluate this method with respect to a quantitative determination of complex structures. To gain structural information about the electron transfer complex, quantitative simulations and SIMPLEX fits of the experimentally relaxation data were performed with a home-written program.

B.2 Introduction

B.2.1 The respiratory chain

Mitochondria and a variety of bacteria perform respiration, using oxygen. The series of enzymes that catalyze this process contain a number of redox active prosthetic groups and are located in the cytoplasmic bacterial and inner mitochondrial membranes. The assemblies of these enzyme complexes are usually referred to as respiratory chains (complexes I-IV). Electron transfer reactions catalyzed by the respiratory chain complexes are coupled to the translocation of protons across the membrane leading to an electrochemical potential across the membrane as shown in Figure 1. The conserved energy is used then in the phosphorylation process of ADP to ATP by the ATPase synthase complex (complex V). The chemiosmotic Mitchell theory gave the general mechanistic principle of oxidative phosphorylation, which explained the coupling between respiration and ATP synthesis [1-5].

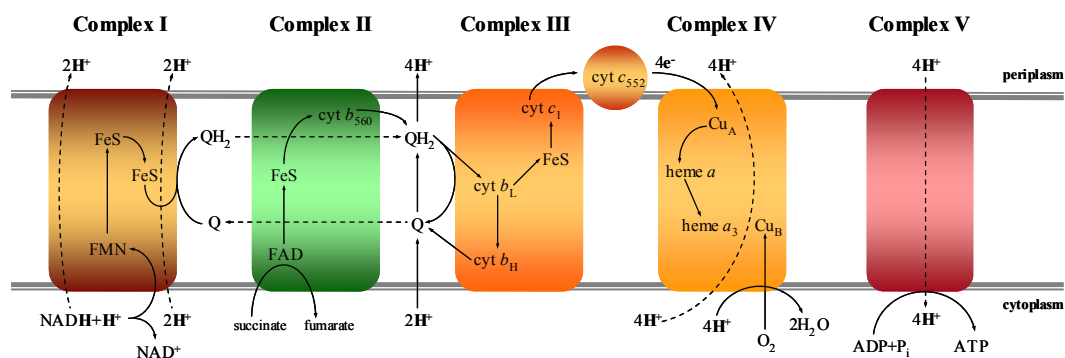


Fig. 1: Schematic representation of the respiratory chain indicating the electron transfer pathway from NADH/H⁺ to molecular oxygen via complexes I-IV.

In the aerobic respiratory chain of the soil bacterium *Paracoccus denitrificans*, which resembles very closely the process in mitochondrial membranes, electrons are passed from complex I (NAD⁺/NADH redox couple) down the chain to complex IV where molecular oxygen is the final acceptor of the electrons (O₂/H₂O couple). The energy released by these electron transfer reactions is used to transport protons across the membrane generating a transmembrane proton electrochemical gradient ($\Delta\mu_{H^+}$). This gradient consists of two components, a proton concentration gradient (ΔpH) and a transmembrane electrical potential ($\Delta\psi$). The electrochemical gradient across the membrane enables complex V to synthesize the energy carrier ATP.

B.2.1.1 Components of the respiratory chain

Complex I, or the NADH:ubiquinone oxidoreductase (NADH dehydrogenase), is the largest of all membrane bound enzymes of the mitochondrial and bacterial respiratory chains, which is one of the reasons why it is the least understood. It catalyzes the transfer of two electrons from NADH to ubiquinone in a reaction that is associated with the active transport of protons across the membrane. Complex I contains as cofactors several iron-sulfur centers (Fe_2S_2 and Fe_4S_4) and a flavin mononucleotide (FMN).

Complex II, or succinate:ubiquinone reductase (succinate dehydrogenase) participates in the electron transport chain by transferring electrons from succinate to the ubiquinone pool. In contrast to complex I, it delivers electrons to the electron transport chain without proton translocation because the reduction of ubiquinone by succinate is not associated with any proton movement across the membrane. It contains FAD (flavin adenine dinucleotide), several FeS-clusters and is anchored to the membrane by a b-type cytochrome.

Complex III, or ubiquinol:cyt *c* oxidoreductase (Cytochrome bc_1) delivers electrons from ubiquinol to cytochrome *c*. This redox reaction is again associated with the generation of a proton gradient across the membrane by a mechanism known as the Q-cycle (proton translocation by substrate protons). As the redox chemistry of quinol is coupled to protonation and deprotonation, cytochrome bc_1 complex has two active sites known as (Q_o), where oxidation of ubiquinol and release of protons take place and (Q_i), where ubiquinol reduction is coupled to an uptake of protons. Additional redox groups in the cytochrome bc_1 complex are Rieske-type FeS center (Fe_2S_2), two b-type hemes and a membrane anchored cytochrome c_1 .

Complex IV, or Cytochrome *c* Oxidase performs the final step in the electron transport chain of mitochondria and many aerobic bacteria. It catalyzes the transfer of four electrons from the reduced cytochrome *c* to molecular oxygen, forming sequential two water molecules. The electrons from the oxidation of cytochrome *c* come from the periplasmic side of the membrane while the protons required for the water formation are taken from the inner cytoplasmic side of the membrane. Therefore, complex IV generates an electrochemical gradient by the reduction of oxygen to water and in addition pumps one proton per electron across the membrane.

Complex V, or ATP synthase (F_1F_0 -ATPase) utilizes the electrochemical gradient across the membrane to promote the phosphorylation of ADP in order to produce ATP. ATP synthase is a functionally reversible enzyme. Although under physiological conditions it synthesizes ATP it can also hydrolyze ATP to pump protons against the electrochemical gradient. ATP synthesis and hydrolysis occurs in the F_1 complex.

B.2.2 Structure and function of the CcO

B.2.2.1 Structure of the CcO

The three-dimensional crystal structures of cytochrome *c* Oxidase from *P. denitrificans* showed that the bacterial enzyme is an aa_3 – type oxidase, very similar to that of beef heart mitochondria oxidase. It is composed of four subunits I, II, III and IV. Subunits I and II are the one essential for the function of the enzyme as they carry all four redox active metal centers: two heme *a* moieties (*a*, a_3) and two type of copper centers (Cu_A , Cu_B). The function of subunit IV is unknown and that of subunit III is not completely clear, but it may be involved in the assembly of CcO [6-9].

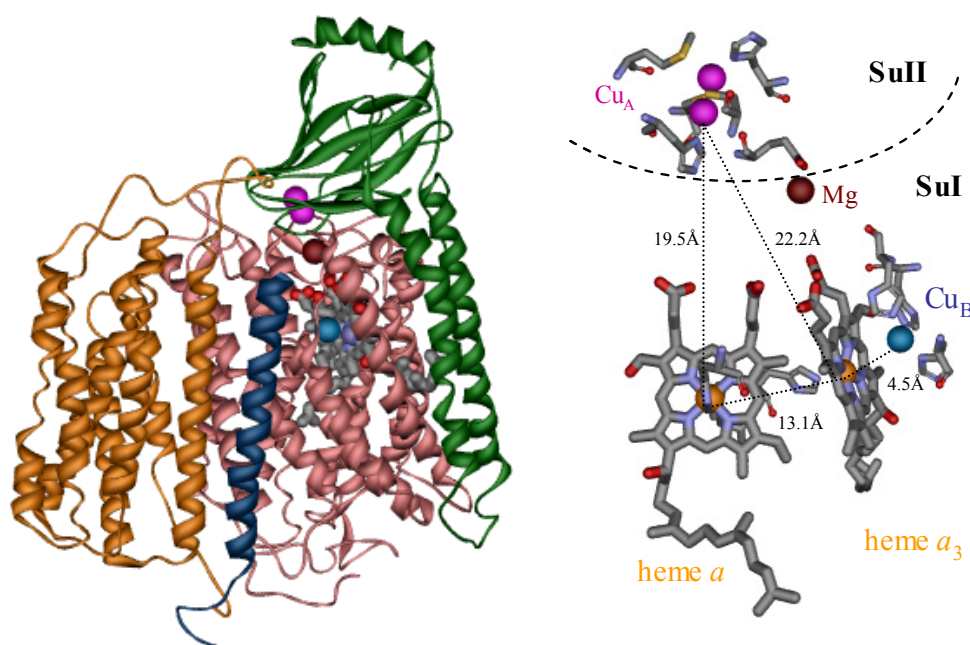


Fig. 2: Structure of CcO from *P. denitrificans* (a) and the redox-active metal centers in subunits I and II with the corresponding ligand amino acid residues. Electron transfer pathways distances are given as center to center. PDB entry 1QLE.

Subunit I contains the heme a_3 with a five fold coordinated high-spin Fe^{2+} ion and the mononuclear Cu_B center. These two metal sites are only 4.5 Å apart and form the catalytically active binuclear site of the enzyme. In addition to this binuclear site subunit I also contains heme a , which is a six coordinated low-spin Fe^{2+} ion. The binuclear Cu_A site is located in subunit II in the periplasmic space above the subunit I [10-15].

The low-spin heme a iron maintains two histidines His94 and His413 as axial ligands. The high-spin heme a_3 iron is coordinated only by one histidine ligand, His411. The Cu_B center is ligated by three amino acid residues, His326, His325, His276. Both copper atoms of Cu_A are ligated by one cysteine residue, Cys216 and Cys220, respectively, and one nitrogen of histidine His181 and one of His224, respectively. The two copper atoms are bridged via the sulfurs of the two cysteine residues, yielding a structure in which the copper and sulfur atoms lie in one plane. Each copper atom has as an additional ligand, which is in one case the sulfur of methionine Met227 and in the other the backbone carbonyl oxygen of Glu218.

In addition to these redox active centers, the bacterial enzyme also contains a non-redox active metal center, which can be Mn^{2+} , Mg^{2+} or Ca^{2+} . This binding site is located at the interface between subunits I and II. The metal ion is ligated by the carbonyl oxygen of Glu218, which is also a Cu_A ligand and of His403 which is hydrogen bonded to one of the heme a_3 propionates. Therefore this site lies directly between Cu_A and heme a_3 . The function of this site is not understood so far [10-15].

B.2.2.2 Function of the CcO

As a terminal enzyme in the respiratory chains of mitochondria and many aerobic bacteria, oxidases are located in the mitochondrial or bacterial membranes. Therefore they use electrons from cytochrome c to reduce dioxygen to water.

Electron transfer pathway

The electrons from cytochrome c enter the protein at the binuclear Cu_A site located within subunit I. The electron transfer rate between the Cu_A and cytochrome c is very fast ($\sim 70.000 \text{ s}^{-1}$), with the complex formation as the rate limiting step. Subsequently the electrons are transferred from the reduced Cu_A center to heme a over a distance of 19.5 Å with a rate of about 20.000 s^{-1} [10-12, 15-19]. The fast electron transfer

between both metal centers can be rationalized by a combination of two effects. First, the small reorganization energy for the rigid binuclear structure of Cu_A and second the presence of an efficient electron transfer pathway. The further path of the electrons is from heme *a* to heme *a*₃ which is part of the binuclear heme *a*₃ - Cu_B center of the enzyme. The electron transfer step between the two hemes is very fast as they are nearly perpendicular to each other with an iron to iron distance of 13.5 Å and closest edge-to-edge distance of only 4.5 Å. An alternative pathway suggests a direct electron transfer from Cu_A to heme *a*₃. However, it was shown that the electron transfer rate for this direct pathway is very slow (~1-100 s⁻¹) making this pathway unlikely. A reason for the slow transfer rate is most probably due to the large distance from Cu_A to the iron atom of heme *a*₃ of 22.1 Å [10-19].

Proton translocation pathway:

The electron transfer in the superfamily of terminal heme-copper oxidases is coupled to vectorial translocation of protons from the cytoplasm across the membrane into the periplasm in the bacterial case [10, 11, 16, 17]. Four protons are consumed during the reduction of molecular oxygen to water. These protons originate from the bacterial cytoplasm while cytochrome *c* donates the electrons from the opposite side of the membrane. Thus an electric field gradient and a pH difference are generated across the membrane. In addition, four protons per oxygen molecule are translocated (“pumped”) across the inner membrane using the free energy available from the exergonic reaction of water formation. This leads to an enhanced electric field and proton gradient, which is then converted to more useful energy forms via energy conserving systems such as ATP synthase.

The translocating pathways for the substrate protons to the oxygen binding site as well as the pathway for the protons pumped across the membrane have been identified. In the *P. denitrificans* CcO two possible proton pumping pathways similar to that of beef heart enzyme were identified. One shorter K-channel named after Lys354, which leads toward the binuclear center and a longer one referred to as the D-channel named after Asp 124 involving a number of polar amino acid residues [20-23]. The mechanism by which the electron transfer is connected to the proton uptake and translocation remains still unclear although different mechanisms have been discussed for a long time [10, 11, 16].

B.2.3 Structure and function of cytochrome *c*

Bacterial cytochrome *c*

Cytochrome *c*₅₅₂, acts as an electron mediator between the cytochrome *bc*₁ complex (complex III) and CcO (complex IV) in the respiratory chain of the bacterium *P. denitrificans*. The bacterial cytochrome *c*₅₅₂ is membrane bound while a soluble cytochrome *c* links both complexes in mitochondria [24].

Two genetically modified fragments of cytochrome *c*₅₅₂, both lacking the membrane anchor domain could be crystallized and X-ray structures exist [25]. Both soluble fragments are still functional with respect to their electron transfer capabilities to CcO [26]. The structure of the smaller 100 amino acid residues containing fragment was determined in the reduced and oxidized state. The structure of both states showed no significant conformational differences in contrast to the structures of the two states of the eukaryotic cytochromes *c* [26, 27].

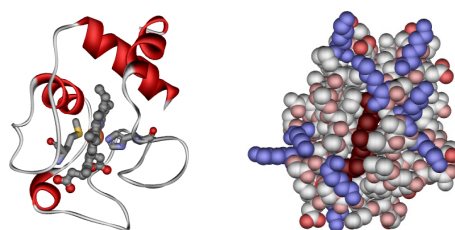


Fig. 3: 3D solution structure of oxidized cytochrome *c*₅₅₂ from *P. denitrificans* (PDB entry 1QL3). Left panel, surface exposed lysine residues surrounding the heme crevice where the heme moiety is shown in dark red, and the lysine amino acid residues in blue.

Cytochrome *c*₅₅₂ is a class I *c*-type cytochrome containing a *c*-type heme covalently attached to the protein. Thioether bonds connect the heme vinyl groups at pyrrole rings B and C with the thiol side chain of two cysteine residues (Cys14 and Cys17) forming the conserved Cys-X-Y-Cys-His motif. The heme iron has as axial ligands the histidine His18 and a methionine Met78. The heme iron has two physiologically relevant oxidation states: Fe(II) and Fe(III).

Cytochrome *c*₅₅₂ from *P. denitrificans* possesses 12 strongly acidic and only 11 strongly basic amino acid residues while horse heart cytochrome *c* possesses 21 strongly basic and 12 strongly acidic ones. Most of the basic residues are clustered around the solvent exposed heme edge. The surface around the exposed part of the heme is positively and the surface of the opposite side strongly negatively charged. The electrostatic surface potential of the eukaryotic cytochrome *c* is qualitatively

similar to the bacterial cytochrome c_{552} but the absolute values are very different. For example, the surface of bacterial cytochrome c_{552} is much more positively charged around the exposed part of the heme compared to that of horse heart cytochrome c . Especially the differences in the positively charged part result in a optimum turnover rate at lower ionic strength for c_{552} [25, 27]. It is, however, still an open question what the consequences or advantages are of having a membrane anchored donor/acceptor protein shuttling between complex III and IV [24].

Cytochrome c_1

Cytochrome c_1 is anchored to the periplasmic surface of the bc_1 complex. This protein from *P. denitrificans* has an unusually high molecular mass. Axial ligands to the covalently attached c -type heme are histidine and methionine [28].

Mitochondrial cytochrome c

Mitochondrial cytochrome c mediates the electron transfer between the membrane-integrated complexes III and IV in the respiratory chain of eukaryotes.

The three-dimensional structure of oxidized horse heart cytochrome c , determined with high resolution showed that it carries a c -type heme prosthetic group, covalently bound to the polypeptide chain via a thioether link between cysteine residue Cys14 and porphyrin ring B as well as between Cys17 and porphyrin ring C. The heme contains a six- coordinated iron. In addition to the four porphyrin nitrogens the iron is ligated by two axial ligands, a histidine (His18) and a methionine (Met80). The heme group is buried within a hydrophobic pocket formed by the polypeptide chain. Horse heart cytochrome c is characterized by a large number of lysines residues, which are particularly concentrated in a ring around the most exposed edge of the heme [29, 30].

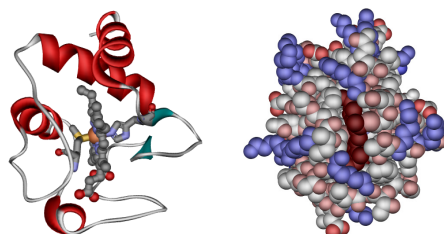


Fig. 4: 3D solution structure of oxidized horse heart cytochrome c (PDB entry 1HRC). Left panel, surface exposed lysine residues surrounding the heme crevice where the heme moiety is shown in dark red, and the lysine amino acids in blue.

B.2.4 Electron transfer protein-protein complexes

B.2.4.1 Nature and structures of protein-protein complexes

Protein-protein interactions are important in a variety of biological processes as for example electron transfer and signal transduction. Interaction between proteins are not optimized to achieve highest affinity, but rather to acquire a lifetime that is sufficient for the function of the protein-protein complex. Therefore, the lifetime of a protein-protein complexes can be very short if its function proceeds with a high turnover rate. As a result such protein-protein complexes are characterized by their transient nature. Examples for such transient complexes are the redox proteins in the mitochondrial respiratory chain which catalyze the reduction of oxygen to water in consecutive intra- and interprotein electron transfer reactions [31-34]. Therefore, formation of an electron transfer protein-protein complexes is required as small diffusible redox proteins facilitate the electron transport between the large membrane embedded enzyme complexes. To promote the high turnover and efficiency of the energy conversion machinery the binding of the small electron carriers has to be both fast and specific to reach complex orientation of the reaction partners suitable for rapid electron transfer followed by fast dissociation of the product [31-36]. This is achieved by high association and dissociation rate constants. Because of their transient character structures of protein-protein complexes are difficult to obtain and only a few structures of such complexes have been determined by X-Ray diffraction or NMR spectroscopy [37-44].

One of them is the structure of the electron carrier cytochrome *c* complexed to cytochrome *bc₁* of yeast [42]. This structure showed a tight and specific binding where cytochrome *c* is bound to the cytochrome *c₁* subunit of the enzyme. The complex is stabilized by hydrophobic interactions around the heme cleft, creating a small compact contact site. A central cation- π interaction appears to be an important feature of this cytochrome binding. In addition, the binding comprises weak electrostatic interactions involving peripheral patches of charged residues, which further stabilize the protein-protein complex by long range electrostatic forces. These forces might be important for the orientation of the two constituents of the complex with respect to each other. The distance between the two iron centers in the complex between yeast cytochrome *bc₁* and iso-1-cytochrome *c* is 17.4 Å, which is the shortest reported for *c*-type cytochromes and its redox partners. The close distance and the orientation of both *c*-type hemes suggest a fast and direct heme to heme electron

transfer. An electron transfer rate of $8.3 \cdot 10^6$ based on the Dutton model s^{-1} was calculated [45].

The interplaner angle of the heme groups is 55° , which is close to the value of app. 60° found in other structures. This geometry might be generally favorable for electron transfer complexes between *c*-type cytochromes and their heme group containing redox partners [42,45,46]. In the other two structures of *c*-type cytochrome complexes available, yeast iso-1-cytochrome *c* and horse heart cytochrome *c* are co-crystallized with yeast cytochrome *c* peroxidase. In these complexes the distance between the two iron centers is much longer, 26.5 Å and 30 Å respectively. Therefore, indirect electron transfer pathways, involving aromatic amino acids was proposed [41, 42].

NMR spectroscopy has been also used to determined structures of different protein-protein complexes of redox proteins. It demonstrated that only in some cases the proteins assume a single orientation within the complex while other complexes are found to be non-specific and exist as a dynamic ensemble of differently oriented complexes [43,44,47]. An example for the former is the plastocyanin/cytochrome *f*-complex [43,44] where the observed large chemical shift perturbations are evidence for a well-defined orientation of the proteins within the complex. The NMR studies showed that uncharged polar as well as hydrophobic residues display the largest chemical shift perturbations upon binding. The binding interface determined in this complex consist of a small hydrophobic patch for specificity, surrounded by polar, uncharged residues that may enhance dissociation and a patch of charged amino acid residues that enhances the association by electrostatic interaction [77]. The electrons entry and exit site is located within the hydrophobic interaction surface, ensuring rapid electron transfer from one redox partner to the other.

Finally, the respiratory chain complexes form large structural and functional units called supercomplexes. The existence of stable supercomplexes III and IV, which contain in bacteria tightly bound cytochrome *c*, have been known for many years [48]. But the idea that respiratory chain complexes associate into supercomplexes has been accepted generally only after the isolation of supercomplexes consisting of complex I, III and IV from beef heart mitochondria and of assemblies of complexes II, III, and IV form in yeast [49].

It seems that the organization in supercomplexes have some functional advantages as catalytic enhancement by reducing the diffusion distances of substrate or channeling

of the substrate to a specific enzyme. In addition, supercomplex formation may play an important role in structural stabilization of labile membrane protein complexes. The later appeared to be the major factor for the assembly of complexes I, III and IV (1:4:4 stoichiometry) and cytochrome c_{552} into a NADH oxidase supercomplex in *P. denitrificans* [50].

B.2.4.2 Model for protein-protein complex formation

The determination of protein-protein complex structures resulted in a better understanding of the mechanism of complex formation [37-44]. It became clear that electrostatic interactions between acidic and positive patches on the protein surfaces are important for the affinity and that hydrophobic interactions contribute to specificity. These findings in combination with earlier kinetic experiments supported the so-called two-state model of complex formation. This model divides the electron transfer complex formation in two steps [35, 36]. In the first step complex formation is influenced by long-range electrostatic interactions leading to encounter complexes. In the second step the two proteins orient in such a way that they adopt the optimal orientation for an efficient electron transfer. It is believed that short-range forces, such as hydrophobic contacts and hydrogen bonds, are the driving forces for this rearrangement. In the initially formed encounter complexes the partner proteins can assume many different orientations within the binding domain, which are of approximately equal energy. The reason for the occurrence of such an ensemble of orientations is the large number of charges spread over a large surface area, which are all involved in electrostatic protein-protein interactions and the long range action of Coulombic forces. Both together assure high affinity but poor specificity. The active electron transfer complex is in contrast a single well-defined complex, stabilized by hydrophobic interactions as well as electrostatic contacts. The former provide the specificity.

B.2.4.3 Electron transfer complex of CcO and cytochrome *c*

Cytochrome *c* is the specific and efficient electron mediator between complexes III and IV of the mitochondrial and bacterial respiratory chains therefore the complex formation and the electron transfer reaction between the redox proteins are of particular interest. However, up to now there is no X-ray structure of the cytochrome *c*/CcO complex available. Nevertheless, the complex formation and electron transfer

between the last two proteins has been a subject of extensive investigations during the last years.

It was for example found that the reaction between cytochrome *c* oxidase and cytochrome *c* is strongly dependant on the ionic strength, indicating that electrostatic interactions stabilize the complex. It has been suggested that structural differences between the complex formed at a very low and at a physiologically more relevant ionic strength might be the reason for the observed differences in electron transfer rate constants [51-57]. At low ionic strength the product dissociation is believed to be the rate-limiting step. Formation of a 1:1 stoichiometric complex, which may be isolated *in vitro* has been observed at ionic strength below 10mM for the mitochondrial cytochrome *c* and CcO [54]. There is no experimental estimate for the dissociation constant for the complex of bacterial cytochrome *c*₅₅₂ neither with the full size CcO nor with the soluble Cu_A domain. Nevertheless, the K_D for the complex of bacterial cytochrome *c*₅₅₀ and the soluble Cu_A domain was estimated to be 1.6 μ M, which is very similar to that between the mitochondrial cytochrome *c* and the intact CcO (K_D = 1 μ M) [54, 55, 58].

The surfaces of cytochrome *c* and CcO have been of particular interest in many studies as the electron transfer between these two proteins depends on specific recognition with an affinity low enough to allow for rapid dissociation. This resulted in the identification of a number of amino acid residues on the surfaces of both proteins, which are involved in recognition and complex formation.

B.2.4.3.1 CcO binding domain

Kinetic studies of the electron transfer between CcO and cytochrome *c* have shown that the Cu_A center in the oxidase is the primary acceptor of electrons [52].

The location of the cytochrome *c* binding site on oxidase has been mapped using several methods, including chemical modification and site-directed mutagenesis [59-66]. A number of negatively charged amino acid residue located mainly in subunit II were identified to be involved in cytochrome *c* binding [58,62-64]. Taken together, all these studies indicated that the binding site is predominantly located in subunit II of CcO above the Cu_A center. This is consistent with the crystal structure of *P. denitrificans* oxidase as well as with the eukaryotic enzyme. Both structures reveal that these exposed acidic residues are clustered, creating an extended, negatively charged patch on the surface of subunit II. The size and extend of the docking patch

(mainly glutamates and aspartates) in CcO from *P. denitrificans* has been defined by consequent mutagenesis combined with kinetic studies (E126, D135, D178, E140, E142, D146, D159). In addition, some residues (D257 and D156) of subunit I have also been found to be part of the binding site in the *P. denitrificans* enzyme [62-64].

Considering the size of the negatively charged region it was suggested that a rather unspecific, electrostatically favored “encounter complex” is formed first, which then rearranges to a more specific complex that is optimized for electron transfer [53, 63, 64]. In this concept, the initial recognition between the redox partners is not by stereo specific lock- and key- interaction but rather via complementary charged patches that can associate in many different orientations of similar energy [35].

The interaction domain on subunit II of CcO from *P. denitrificans* has also been investigated for hydrophobic residues, which may contribute to the electron transfer reaction. The results indicated that tryptophan W121 is the electron entry site to the oxidase and that in addition to the acidic residues some other hydrophobic residues (Y122, I117, L137) play an important role in the docking reaction [62-65].

B.2.4.3.2 Cytochrome *c* binding domain

It has been demonstrated in several studies with cytochrome *c* and its different redox partners that it binds essentially through electrostatic interactions. Therefore, further investigations have been focused on the charged residues on the protein surface [66-69]. A number of basic residues (mostly lysine), concentrated in a ring that surrounds the most exposed heme edge, have been identified to be involved in the electrostatic interactions with the complementary acidic residues on the CcO [72]. The classical horse heart cytochrome *c* is characterized by its high excess of basic residues and very high positive pI value compared with other *c*-type cytochromes. The soluble fragment of *c*₅₅₂ from *P. denitrificans* resembles the mitochondrial cytochromes not only in size but also in surface charge distribution, despite the fact that it carries a slight negative net charge at neutral pH (pI of 6.3) [26, 27, 29, 30].

B.2.4.3.3 Kinetics and ionic strength dependence

A strong dependence of the electron transfer rates on ionic strength has been observed for the reaction between the two redox partners from *P. denitrificans*, indicating that the preliminary protein-protein interaction is also in this case of electrostatic nature (Figure 5).

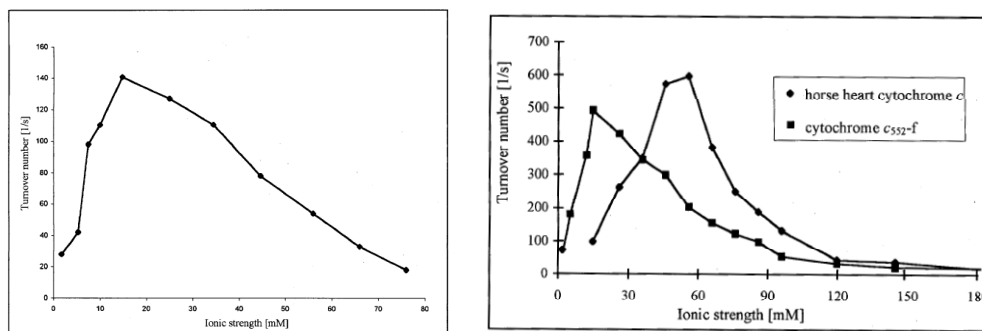


Fig. 5: Ionic strength dependence on the turnover number, a) oxidation of cytochrome *c*₅₅₂-ff by wild type *aa3* oxidase under steady-state conditions at the pH optimum of 6.1, b) oxidation of horse heart cytochrome *c* and cytochrome *c*₅₅₂-f respectively under steady-state conditions at 20 μ M substrate [70].

An explanation for the bell shaped dependence of activity on ionic strength has been suggested: The turnover rate initially increases with ionic strength, because an increase in salt concentration favors diffusion at the binding site and allows rearrangement of the primarily by long range electrostatic forces aligned proteins to achieve the optimum orientation for electron transfer. Short-range forces such as hydrophobic interactions might contribute significantly in this fine tuning. At high ionic strengths a decrease in the turnover rate is observed, due to the shielding of charges leading to a decrease in the affinity of the redox partners. At lower ionic strength the redox partner proteins lack the conformational flexibility to achieve the conformation optimal for electron transfer [62-65].

The electron donor properties of the soluble fragments of *c*₅₅₂, of the full size *c*₅₅₂ with membrane anchor from *P. denitrificans* and of the horse heart cytochrome *c* to CcO from *P. denitrificans* have been analyzed by steady-state kinetic experiments [70, 71]. Both the shortest fragments of *c*₅₅₂ and the nonhomologous electron donor, horse heart cytochrome *c* displayed maximum turnover rates (about 1000 s⁻¹) at pH 7.5, while the native membrane anchored protein exhibit maximal rates at pH 6.1. In addition, mitochondrial and bacterial cytochromes showed crucial differences in their kinetic behavior with respect to the ionic strength. The strongly charged mitochondrial protein yields an optimum reaction rate with the *P. denitrificans* CcO at an ionic strength of 56 mM while this value is significantly lowered to 15 mM for the bacterial cytochromes. However, at the optimum conditions both cytochromes have comparable sets of kinetic parameters. Furthermore, mutations on the presumed docking site of CcO demonstrated that both type of cytochromes, though quite different in their electrostatic properties, cover similar areas on the hydrophilic

domain of subunit II of the CcO. Nevertheless, the possibility of specific docking sites differing to some extent for the two types of cytochromes was not excluded completely [70]. It is important to note that in all kinds of experiments the interaction between a detergent-solubilized oxidase and a soluble c_{552} have been investigated in solution. The physiological situation, where both proteins are embedded in a membrane may pose much higher constraints on the complex arrangement. The c_{552} membrane anchor would fix the distance of the heme domain with respect to the membrane surface and any supermolecular association with the oxidase or with the oxidase and the bc_1 complex would restrict the requirement for a diffusional encounter of the proteins even further [65].

B.2.4.3.4 NMR and MD studies

The interaction between ^{15}N labeled c_{552} and the soluble subunit II of CcO from *P. denitrificans* has been studied by solution NMR spectroscopy in order to obtain structural data regarding the surface contacts between c_{552} and CcO [72]. In these NMR experiments only small chemical shift changes were observed for c_{552} upon interaction with the soluble subunit II. Similar amino acid residues in c_{552} were identified to be affected upon binding, independent of the oxidation state of c_{552} , implying that the protein-protein interaction is not dependent on the redox states of the electron transfer partners. Only one, namely K70, of the nine positively charged lysine residues showed a change in the NMR experiment upon complex formation. The strongest chemical shift perturbations upon binding were observed for a patch of non-charged hydrophobic amino acid residues (A16, G75, A81, D24, V26, A79, F80, G25, G27, G82), centered around the heme, in contrast to the docking studies that proposed a complex formation based on multiple electrostatic contacts between the partner proteins [see below].

The interaction surfaces between beef heart CcO and horse heart cytochrome *c* have also been studied by computational approaches. They provide again evidence for a salt bridge stabilized complex, primarily involving two lysine residues on the electron donor molecule and a central hydrophobic region surrounding the heme cleft [73].

Computational docking studies yielded models for the complexes of CcO from *P. denitrificans* with its physiological counterpart c_{552} and its non-homologous electron donor partner horse heart cytochrome *c* [74]. In the complex of CcO with c_{552} the latter is found in two different orientations, depending on whether it is docked against

the two-subunit oxidase or against the full size four subunit CcO. Independent of the orientation, the distance between the heme-iron and the center of gravity of the binuclear Cu_A amounts in both cases to 19 Å, respectively.

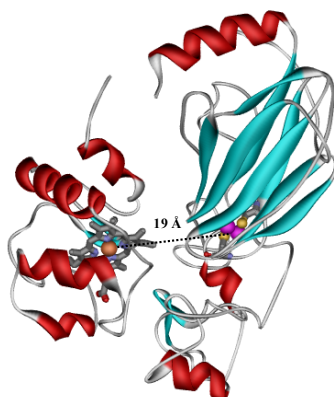


Fig. 6: Predicted complex by docking studies of *c*₅₅₂ and CcO from *P. denitrificans*. Only the interface region of the oxidase is shown.

The complexes between the two-subunit CcO and *c*₅₅₂ as well as horse heart cytochrome *c* are very similar. Nevertheless, five putative salt-bridges have been found to be formed between the acidic residues on the CcO interface and the positively charged lysine residues on the cytochrome surface (D135:K87, E126:K86, D178:K72, D257:K73, D156:K79), while only three residues pairs forming salt-bridges were found with *c*₅₅₂ (D159:K15, D257:K70, D156:K77 with two subunit CcO and D159:K70, D178:K77, D156:K19 with four subunit CcO). In addition, the complex of CcO with horse heart cytochrome *c* is very similar to a previously proposed docking model of bovine CcO with horse heart cytochrome *c*.

Very recently, docking studies using HADDOCK program were performed. An ensemble of structural models for the complex between CcO and *c*₅₅₂ were calculated in this study based on the experimental data from site directed mutagenesis and NMR experiments. It was found that a single static structural model cannot satisfy all experimental data simultaneously. Hence, it was proposed that the complex exists as a dynamic ensemble of different orientations in equilibrium and may be represented by a combination or average of the various limiting conformations calculated [75].

B.2.5 EPR characteristics of CcO and cytochrome *c*

B.2.5.1 EPR characteristics of the redox active metal centers in CcO

The mixed valence $[\text{Cu}_A(1.5) \dots \text{Cu}_A(1.5)]$, $S = 1/2$ binuclear Cu_A has unique spectral properties, which make it distinct from any other classes of copper complexes. A seven line hyperfine pattern arising from the two equivalent copper nuclei ($I = 3/2$) is diagnostic for a Cu-Cu interaction in which one unpaired electron is equally shared between two Cu ions forming a mixed valence binuclear center.

The similarities observed between the EPR detectable Cu_A site in beef CcO and nitrous-oxide reductase (N_2OR) from *P. stutzeri* were the first indication that the Cu_A signal in CcO could be attributed to a mixed valence binuclear copper site. Multifrequency EPR investigations of beef CcO allowed later the resolution of the characteristic multiline hyperfine splitting pattern (Figure 7). This confirmed together with spectral simulations that the Cu_A site in CcO is unquestionably a mixed valence binuclear copper center [76-82].

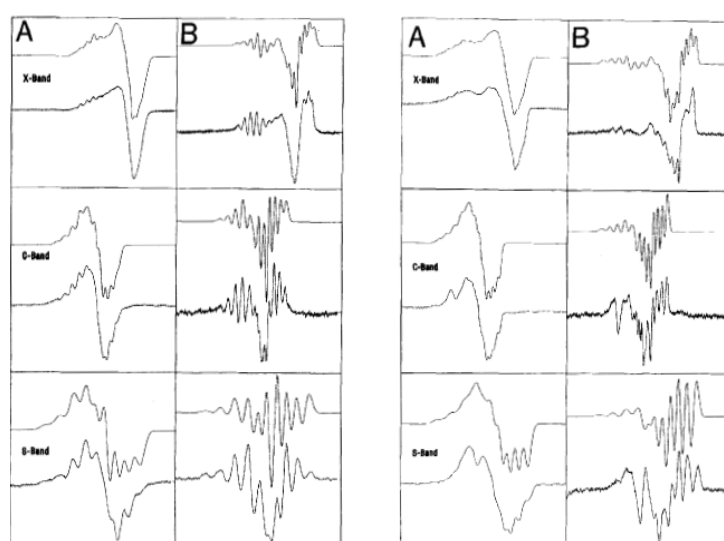


Fig. 7: X-band, C-band and S-band first-derivative (A) and second-derivative (B) spectra and computer simulations (above the experiment) for N_2OR (left panel) and bovine heart CcO (right panel) [78].

Cu_A in the oxidized state of CcO from *P. denitrificans* is also an mixed valence binuclear copper center as it gives rise to an EPR signal with \mathbf{g} -tensor values of $g_{zz} = 2.18$, $g_{yy} = 2.03$, $g_{xx} = 2.00$ and an Cu-hyperfine tensor with $A_{zz} = 38.0$, $A_{yy} = 24.5$ and $A_{xx} = 22.7\text{G}$, similar to that of the binuclear copper in beef heart CcO and N_2OR from *P. stutzeri* [83, 84]. The EPR spectrum of Cu_A in the soluble subunit II from *P. denitrificans* at neutral or acidic pH shows at X-Band an axial signal with $g_{\parallel} = g_{zz} = 2.18$ and $g_{\perp} = g_{yy} = g_{xx} = 2.01$ and with partially resolved hyperfine structure. The

hyperfine structure shows an intensity pattern of 1:2:3:4:3:2:1 and a splitting of 35 G (Figure 8). The g values and the copper hyperfine coupling constants are the same as those of the full CcO complex [79, 84, 85].

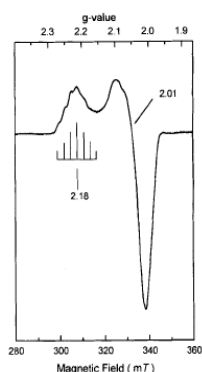


Fig. 8: X-band EPR spectrum of *P. denitrificans* Cu_A domain at pH 6 and glassing agent (ethanediol) [84].

From a spectroscopic point of view the soluble subunit II of CcO has the advantage that the binuclear Cu_A ($S = 1/2$) is the only EPR active center in contrast to the full oxidase where in manganese-free enzyme preparation three additional EPR active metal centers are present [83, 85, 86].

A precise determination of the Cu_A g -tensor orientation with respect to the molecular axis system requires single-crystal EPR data, which are not available yet. However, extensive EPR studies on frozen solutions of Cu_A in N₂OR and on bovine heart CcO in orientated membranes together with quantum chemical calculations lead to the following assignment (Figure 9): g_{zz} lies approximately perpendicular to the CuSSCu plane, g_{yy} lies along the Cu-Cu direction, and g_{xx} lies along the S-S axis [79, 81].

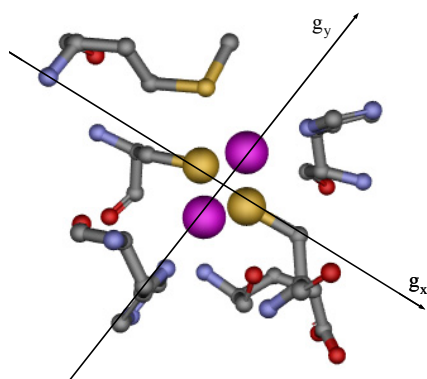


Fig. 9: Orientation of the Cu_A g -tensor in the molecular coordinate system. The copper atoms are shown in violet and the cysteine sulfur atoms in yellow.

The T_1 relaxation time of Cu_A has been measured using saturation recovery Pulsed EPR in the temperature range of 1.5 to 20K [87] and are represented later in table 1.

The full CcO complex contains in its oxidized state four EPR active metal centers: beside the already mentioned Cu_A site in subunit II, the enzyme contains a low-spin heme a [Fe(III), $S = 1/2$], a high-spin heme a_3 [Fe(III), $S = 5/2$] and a mononuclear Cu_B [Cu(II), $S = 1/2$], all three are bound to subunit I. The low-spin heme a has a characteristic rhombic EPR signal with g values of $g_1 = 3.07$, $g_2 = 2.25$, $g_3 = 1.45$. The high-spin heme a_3 and Cu_B form the binuclear active center of the enzyme and are strongly antiferromagnetically coupled to form an $S = 2$ spin system, which exhibits no EPR signal in conventional EPR spectrometer [86-91].

B.2.5.2 EPR characteristics of cytochrome c

Cytochrome c contains a six-coordinated low-spin Fe(III)-complex with $S = 1/2$ displaying a very broad but well-resolved rhombic EPR signal with g -tensor values of $g_{zz} = 3.06$, $g_{yy} = 2.25$, $g_{xx} = 1.25$ (Figure 10).

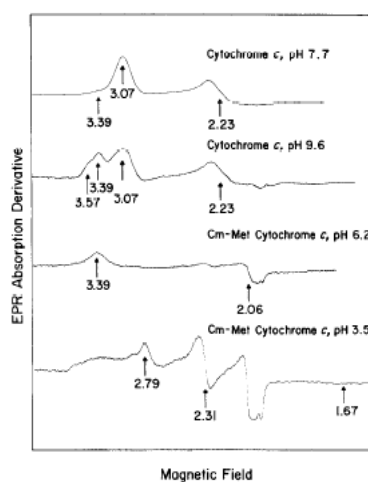


Fig. 10: The EPR spectra of horse cytochrome c and the Cm-Met derivative at 1.6K [93].

EPR experiments with single crystals of horse heart cytochrome c gained the orientation of the principle g values relative to the molecular axes system (Figure 11). The largest g value is within 5° of the porphyrine plane normal direction, the other two in-plane g values are aligned along the porphyrin N-Fe-N axis, within 5° . The medium g -value is along the nitrogen of ring II (bound to Cys 17) and the minimum g value points along the nitrogen of ring I (bound to Cys 14) [92-94]. It has to be noted here that the EPR spectral characteristic of cytochrome c are known to change with

the pH. Especially, at alkaline pH (above 9) the methionine iron bond is broken although the iron is still in the low-spin state [95, 96].

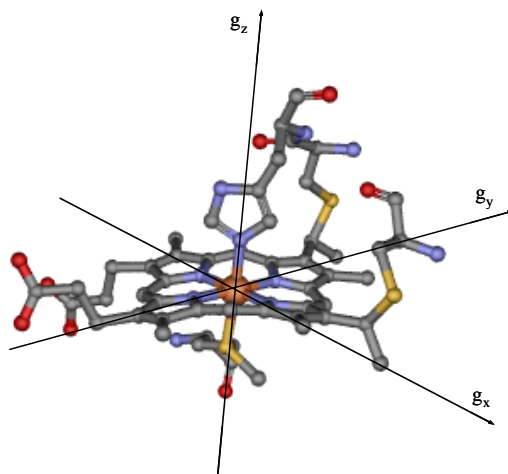


Fig. 11: Orientation of the g -tensor in the molecular coordinate system. The iron atom is shown in orange and the cysteine sulfur atoms in yellow and the pyrrole nitrogens in blue. g_y is trough the nitrogen of pyrrole rings C (bound to Cys 17) and A. The g_x is trough the nitrogen of pyrrole rings B (bound to Cys 14) and D.

The T_1 relaxation times of heme a and cytochrome c have been measured using saturation recovery pulsed EPR in the temperature range 1.5 to 20K [87] and are represented in table 1 together with the values for Cu_A .

Table 1: Longitudinal relaxation (T_1) time of cytochrome c , heme a and Cu_A given in μs from ref. [87].

	12K	15K	18K	20K	23K
cytochrome c	6.508	1.582	0.498	0.255	0.105
heme a	4.606	1.071	0.325	0.163	0.065
Cu_A	164.7	38.2	11.5	5.8	2.3

B.3 Distance determination by EPR techniques

All EPR methods aiming at the determination of distances between paramagnetic centers use the magnetic dipole-dipole coupling between them [36, 52, 53, 97]. The most simple way to measure distances is by CW EPR, if a splitting of the signal due to the dipole-dipole coupling can be observed. In this case the distance can be directly determined from the splitting of the spectral line which is inverse proportional to the cube of the distance [83]. However, for distances larger than 2 nm the splitting is usually too small to be resolved in the intrinsic inhomogeneous line width even for organic radicals in disordered biological samples.

Pulsed EPR methods, like pulsed electron-electron double resonance (PELDOR) and double quantum coherence (DQC) can be used in such cases because these methods are not limited by the inhomogeneous line width [2, 98-113]. They refocus all static broadenings and allow therefore to extend the distance range up to 8nm.

Unfortunately, the application of these advanced pulsed methods to metal centers is hampered due to the very fast relaxation rates of metal ions and the extreme broad intrinsic line widths. The fast relaxation times limit the possible time window for the pulsed experiments, and the broad line widths reduce the efficiency of the microwave pulses, which only excite a small fraction of the spins.

As an alternative approach in the case of such fast relaxing spin pairs, one can observe the dynamic modulation of the dipolar coupling between the two spins induced by the relaxation. Such relaxation measurements are particularly useful if one spin of the pair (B) relaxes much faster than the other one (A) [2, 114-119]. In this experiment, the longitudinal (T_1) and the transverse relaxation (T_2) of the observer spin A is enhanced by the fast modulation of the dipolar coupling by the relaxation of spin B. A number of experiments have been used to measure this dipolar relaxation effect:

- a) CW-EPR saturation experiments have been used to probe the dipolar relaxation enhancement [120-124]. In this case the experiment is sensitive to the product of T_1 and T_2 . A disadvantage of the method is that such saturation measurements on broad inhomogeneous lines are difficult to interpret quantitatively. Additionally it is experimentally difficult to perform such experiments on fast relaxing metal centers.
- b) Pulsed EPR experiments can be used to probe separately the different relaxation rates influenced by the dipolar coupling: An inversion recovery or saturation recovery experiment can be used to probe the influence of the dynamic dipolar coupling on the

T_1 relaxation time. This is especially sensitive if the relaxation rate of the fast relaxing spin B is on the order of the Zeeman splitting of the observer spin [2, 125-131].

A stimulated echo experiment can also be used to probe the dipolar coupling strength by relaxation. Different from the other pulsed experiments the dipolar coupling can be detected in this RIDME experiment as an oscillation of the signal intensity [132]. In this case the dead time of the spectrometer has to be shorter than the inverse dipolar coupling strength and the T_1 relaxation time of spin B. Unfortunately this effect is obscured by ESEEM oscillations from hyperfine couplings to close by spins and therefore difficult to observe at X-band frequencies.

A two pulse Hahn echo experiment can be used to probe the effect on the transversal relaxation time T_2 . This experiment is especially sensitive in the case where the relaxation rate of spin B is comparable to the dipolar coupling strength and additionally also slightly larger than the intrinsic transversal relaxation rate of the observer spin A. The relaxation rates of cytochrome *c* and the binuclear Cu_A and the expected distance of them in the protein-protein complex predict, that in this case only an effect on the transversal relaxation time of Cu_A will be observable. Therefore we performed Hahn-echo experiments to probe the protein-protein complex.

B.3.1 Electron electron dipole-dipole interaction

The magnetic dipole-dipole coupling between two electron spins is analogous to the dipole-dipole coupling between an electron and a nuclear spin. For a pair of two unlike spins A and B at distance R and angle θ_D between the spin-spin vector and the magnetic field (Figure 12) the dipolar interaction Hamiltonian H_{DD} with an external magnetic field in the z-direction can be expressed as:

$$H_{DD} = \frac{g_A g_B \beta_e^2}{R^3} (A + B + C + D + E + F) \quad \{1\}$$

The secular term A of this Hamiltonian is given by:

$$H_{DD} = \frac{g_A g_B \beta_e^2}{R^3} (1 - 3 \cos^2(\theta_D)) S_Z^A S_Z^B \quad \{2\}$$

where g_A and g_B are the effective g-values of spins A and B, respectively. S_Z^A and S_Z^B are the respective Pauli spin operators.

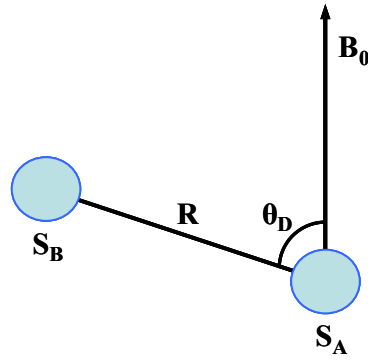


Fig. 12: The two electron spins A and B in a magnetic field sense each other through the magnetic dipole-dipole interaction. The strength of this interaction depends on the distance between the spins R and the orientation (θ_D) of the interspin vector with respect to the B_0 .

This dipolar interaction leads to a splitting of the resonance lines of spin A and B of D :

$$D = \frac{g_A g_B \beta_e^2}{R^3} (1 - 3 \cos^2(\theta_D)) \quad \{3\}$$

For a disordered sample the orientation dependence of the dipolar coupling results in a Pake pattern. The angular part of the dipolar coupling term A vary between -2 for $\theta_D = 0^\circ$ and 1 for $\theta_D = 90^\circ$, passing through 0 at the magic angle of 54.7° . The dependence of the dipole-dipole coupling on the angle θ_D is demonstrated in Figure 13.

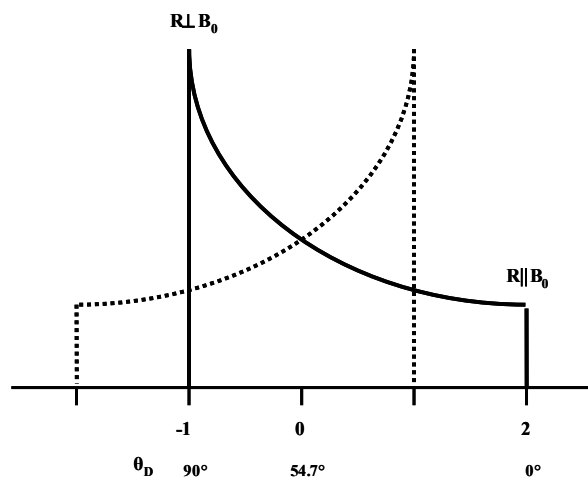


Fig. 13: Dipolar spectrum for a disordered sample (Pake pattern). The frequencies axis is scaled by two in the spectra obtained by pulse ELDOR experiments.

B.3.2 Pulsed techniques to measure dipole-dipole coupling

PELDOR: three-pulse ELDOR was introduced by Milov and Tsvetkov in the eighties [99] and was extended by Spiess and Jeschke to a dead time free four-pulse version [101]. Both pulse sequences select the spin-spin coupling ν_{AB} between the two unpaired electrons A and B out of all other couplings (Figure 14). In the 4-pulse version (Figure 14B), the amplitude of the refocused echo is monitored as a function of the position T of the inversion pulse between the two π -pulses of the detection sequence. The $\pi/2 - \tau - \pi - t - \pi$ detection sequence is applied at a microwave frequency ν_A which is different from the microwave frequency ν_B of the inversion pulse. The echo amplitude oscillates with the frequency of the dipolar coupling D , from which the distance R_{AB} can be calculated using equation {2}. This technique is applicable for two spins with similar relaxation times, where the effect is due to the forced flip of spin B.

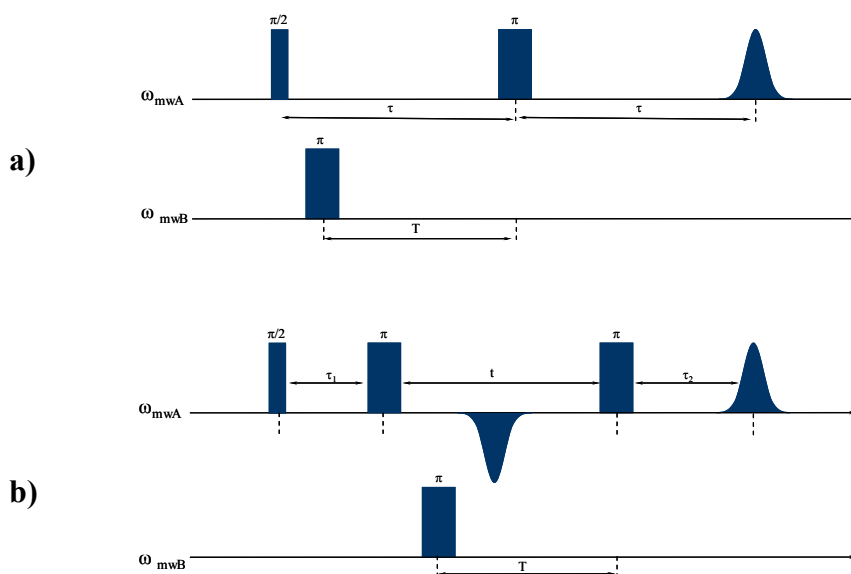


Fig. 14: Pulse sequences for PELDOR: a) three-pulse ELDOR, b) four-pulse ELDOR.

Dipolar Relaxation Measurements: In a coupled spin system, the dipolar Hamiltonian can be modulated by dynamic processes arising from spin relaxation. For two unlike coupled spins, of which one relaxes much faster than the other dipolar coupling can manifest itself as a change in the relaxation behavior of the slower relaxing spin. In the presence of an applied magnetic field, the field experienced by the slow relaxing

species (spin A) is a combination of the applied field and a local fluctuation caused by the spin flips of the fast relaxing species (spin B). If spin B has a much more rapid rate $1/T_1^B$, this will enhance the spin-lattice relaxation rate of species A. The observed enhanced spin-lattice relaxation rate for the A species are then the sum of intrinsic and dipolar contributions to the spin-lattice relaxation and spin-spin relaxation rates of A. It has been shown, based on the time-dependent perturbation relaxation theory that a local minimum in the T_1 relaxation time of the slow relaxing spin (spin A) occurs when the relaxation rate of the fast relaxing spin B, $1/T_1^B$ equals the Larmor frequency of spin A ($T_1^B \sim \omega_A$). Similarly, a minimum in the transverse relaxation time of spin A can be found when the relaxation rate $1/T_1^B$ is equal to the dipolar coupling strength in frequency units ($T_1^B \sim 1/\Delta_{AB}$ and $T_1^B > T_2^A$) [133]. For the two paramagnetic centers investigated in this work only the second process will be effective in the accessible temperature range.

Pulse sequences to measure the transverse relaxation time: The transverse relaxation time can be determined using two-pulse sequence: $\pi/2 - \tau - \pi$ -echo (Figure 15). The decay of the echo signal on incrementing the second free evolution period τ is direct measure of T_m . Often, though, T_m is not determined by a single process, which can lead to non-single exponential behavior. In fact, T_m encompasses all processes that cause loss of electron spin phase coherence. T_2 is one of the contributions. There are many other contributions, including a range of dynamic processes which constitute a dephasing mechanism. The shape of the echo decay curve then depends upon the rate of the process that dominates the dephasing.

Frequently there is an echo modulation superimposed on the decay due to the interaction of the electron spin with nuclear spins. The modulation damps out as a function of the increased pulse separation and this makes it difficult to extract T_m . The extend to which the modulation impacts estimates of T_m depends both on the depth of the modulation and on how long the modulation lasts relative to T_m .

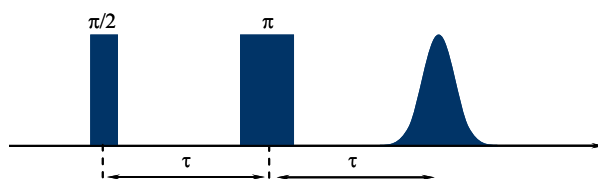


Fig. 15: Hahn echo pulse sequences to measure T_m .

In dipole-dipole coupled spin systems the dynamic dipolar interaction contributes to the Hahn echo decay. Analysis of the signal decay kinetics gives information about the spin-spin process and the magnitude of the electron spin-spin interaction.

The relaxation behavior caused by the dipolar coupling on the Hahn echo decay curve has been calculated to be [134]:

$$\Phi_{dd}(2\tau) = C^{-2} \left[\frac{K}{2} \left((K+C)e^{-(K-C)2\tau} + (K-C)e^{-(K+C)2\tau} \right) - \Delta^2 e^{-K2\tau} \right] \quad \{3\}$$

where Δ is one-half of the dipolar splitting, $K=1/T_1^B$ and $C^2=K^2-\Delta^2$.

In the slow-relaxing ($K \ll \Delta$) and the fast-relaxing limit ($K \gg \Delta$) equation 3 reduces to simple mono-exponential decay curves:

$$\Phi_{dd}(2\tau) = \exp\left(\frac{-2\tau}{T_1^B}\right) \quad \text{and} \quad \Phi_{dd}(2\tau) = \exp(-\Delta^2 T_1^B \tau) \quad \text{respectively.}$$

As T_1^B depends strongly on temperature [2,87], the dipolar relaxation is also dependent on temperature, with a minimum in relaxation time where $1/T_1^B = \Delta$.

Due to the orientation dependence of Δ in an experiment on disordered samples, where molecules with many different orientations of the dipolar vector are excited the resulting dipolar echo decay is a sum of the decays caused by all excited orientations. This manifests itself in a non-monoexponential echo decay curve at higher temperatures where the dipolar relaxation is sensitive to Δ . This effect has to be taken into account by averaging over all molecular orientations if numerical simulations of the echo decay curves are performed because the equations given above are for single orientation. For the spin system investigated in this work, an additional orientation dependence is introduced by the strongly anisotropic g tensor of the cytochrome, leading to an effective g value that is strongly dependent on its specific orientation with respect to the dipolar vector.

Different spectral positions of the powder spectrum relax according to their effective dipolar coupling, causing an anisotropic relaxation over the spectrum. Therefore the anisotropy of the dipolar relaxation can be probed by performing Hahn echo experiments at different field positions on the powder spectrum. High microwave frequencies, which lead to a well resolved powder patterns are recommendable for relaxation measurements as spins with smaller distribution of orientations can be

excited, which makes this experiment much more sensitive to the orientation of the dipolar vector.

As it was describe above, the total Hahn echo signal decay is a product of an intrinsic signal decay of spin A (which includes its own intrinsic relaxation and electron spin echo envelope modulation (ESEEM) effects) and the dipolar relaxation from spin B. It is given as follows:

$$\Phi_{tot}(2\tau) = \Phi_{Adecay}(2\tau)\Phi_{Ahf}(2\tau)\Phi_{dd}(2\tau) \quad \{4\}$$

where Φ_{Adecay} represents the intrinsic echo decay of spin A alone and Φ_{Ahf} is the ESEEM modulation caused by hyperfine coupled nuclei to spin A. To obtain the pure dipolar signal decay Φ_{dd} , the total echo decay Φ_{tot} needs to be divided by the signal of spin A alone, which is given by:

$$\Phi_A(2\tau) = \Phi_{Adecay}(2\tau)\Phi_{Ahf}(2\tau).$$

This division can be easily realized experimentally in the case of protein-protein complexes, because Φ_{tot} and Φ_A can be measured independently. Hence, it was applied in the present work to remove all unwanted contributions and extract pure dipolar relaxation, which thus can be analyzed with higher precision.

Pulse sequences to measure the longitudinal relaxation time T_1 : The longitudinal relaxation time T_1 can be measured directly by saturation recovery and inversion recovery pulse experiments. In the saturation recovery experiment, long microwave pulse which is sufficiently strong to saturate the spin system is applied, followed by detection pulses to monitor the recovery of the longitudinal magnetization to its equilibrium value. Saturation equalizes the populations of the energy levels and thus the saturation recovery experiment uses only half of the population difference of transition at thermal equilibrium. In the inversion recovery experiment the full population difference is utilized by an inversion π pulse. To monitor the magnetization along the z axis as a function of time T two pulse echo sequence is used. The pulse sequences used for determination of T_1 by these two techniques are sketched in Figure 16.

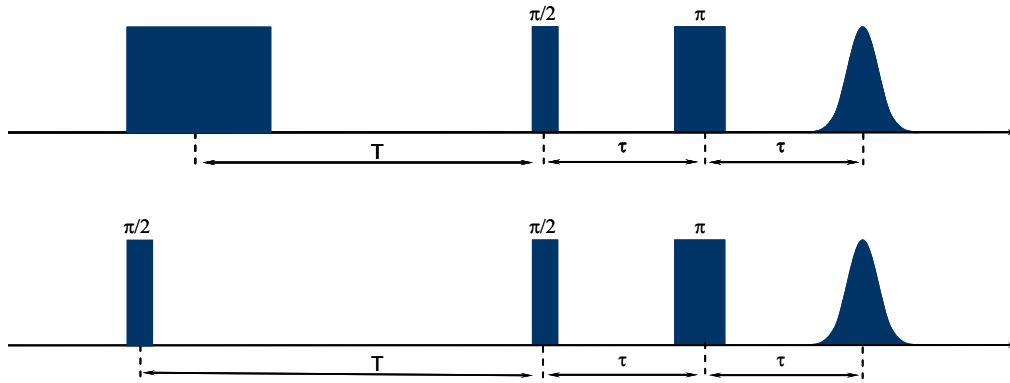


Fig. 16: Pulse sequences to measure T_1 saturation recovery (top), inversion recovery (bottom).

For dipole-dipole coupled spin systems with one slow relaxing spin A and one faster relaxing spin B, the relaxation behavior caused by the dipolar coupling between them on T_1 is described in details in ref. [2].

B.3.3 Relaxation

Relaxation in any physical system is the recovery from a non-equilibrium state to an equilibrium state and the corresponding characteristic times are called relaxation times. Since relaxation times are dependant on the electronic structure of the paramagnetic center and on its interaction with its environment, relaxation times can provide an information on that.

Longitudinal relaxation: In longitudinal electron spin relaxation the magnetic quantum number m_s and thus the energy of the spin system changes. Energy conservation requires that the same energy quantum is absorbed or provided by the environment. The thermal motion of the environment is the source and sink of energy exchange in the electron spin relaxation processes. In solids, thermal motion is usually described by phonons which are energy quanta of lattice vibration. Longitudinal relaxation is caused by absorption or stimulated emission of phonons. Since a coupling between the spin system and the lattice is required this type of relaxation is called *spin-lattice relaxation*. It is characterized by the longitudinal relaxation time T_1 .

Three main processes lead to spin-lattice relaxation, depending on the temperature: direct process, Raman process and Orbach process.

Transverse relaxation: Unlike longitudinal relaxation, transversal relaxation does not require an exchange of energy with the environment. A spin flip which leads to longitudinal relaxation destroys the correlation of the precession phase between the affected spin and the other spins, therefore it also contributes to transverse relaxation. The energy conserving flip-flop process of two spins is twice as effective as a single spin flip in destroying coherence. In such a flip-flop process, one of the spins changes from the α to the β state thereby providing the energy for the second spin to change from β to the α state, a mechanism which is called *spin-spin relaxation*. This process is characterized by transversal relaxation time T_2 . T_2 is often not well defined in solids as an infinite network of coupled spins is present. To quantify the transversal relaxation in the solid state the phase-memory time T_m is often a useful empirical parameter. If the phase memory decay function is a simple exponential, the Bloch equations can be written with T_m in place of T_2 . If the phase memory decay function is not a simple exponential, T_m does not describe well the spin dynamics.

Spectral diffusion: It is a generic term that encompasses all processes that move spin magnetization between positions in the EPR spectrum. If this process moves an excited spin outside the detection window for the experiment that is used to measure T_1 or T_2 , the spectral diffusion is an apparent relaxation process. Spectral diffusion includes motion of an anisotropic paramagnetic center, electron-electron exchange, electron nuclear cross relaxation and nuclear flip-flops.

Spin diffusion: It is observed in spin echo experiments when the concentration of electron spin/gauss is sufficiently high that the second pulse flips both the observer spin and the neighboring electron spin to which the observed spin is dipolar coupled. By flipping the neighboring spin the pulse changes the resonant energy of the observed spin and results in dephasing. In the two-pulse experiment, spin diffusion interferes with the refocusing of the magnetization and thus contributes to T_m . Spin diffusion is also called by some authors *instantaneous diffusion*.

B.4 Results and Discussion

Here, we want to study the complex formation between CcO oxidase and its redox partner cytochrome *c* by measuring the dipolar interaction between the paramagnetic Cu_A center in CcO and the paramagnetic Fe (III) center in cytochrome *c*. Analysis of the dipolar coupling may be used to determine the distance and orientation between the two metal centers within the protein-protein complex.

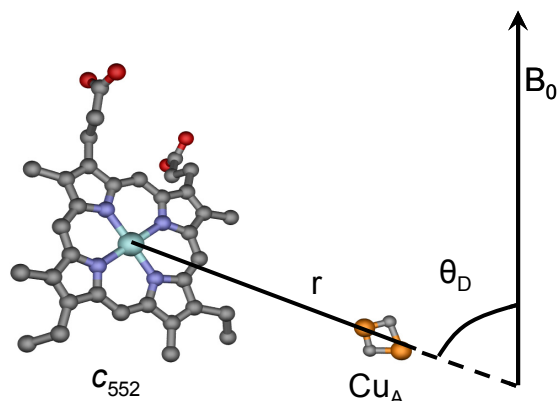


Fig. 17: Schematic representation of the dipolar interaction between two electron spins A (Cu_A) and B (c₅₅₂). R is the distance between the two spins, θ_D is the angle between the dipolar vector and the external magnetic field B_0 .

Full size CcO contains four paramagnetic centers, which leads to an EPR spectrum with overlapping signals. In addition some of these centers are close enough to influence each others relaxation properties. To avoid these complications, soluble subunit II of CcO (CcO_{II}), which carries only binuclear Cu_A as a paramagnetic center was used as the simplest protein system to which cytochrome *c* can bind. Consequently, upon protein-protein complex formation two $S = \frac{1}{2}$ spin centers, the Cu_A from CcO_{II} and the Fe (III) from cytochrome *c*, would be coupled to each other. The two-pulse field-swept spectra of the paramagnetic centers in the separated proteins, are shown in Figure 18, together with the corresponding g tensor values. The signal exhibited by Cu_A at neutral pH is typical for a mixed valence binuclear copper center [Cu^{1.5+}...Cu^{1.5+}]. Cytochrome c₅₅₂ exhibits a broad rhombic EPR spectrum, typical for *c*-type ferricytochrome containing Fe (III) in a low-spin state. The c₅₅₂ spectrum was taken at lower temperature (5 K) as it has much shorter relaxation times (electron spin-spin relaxation times T_2) compared to Cu_A. The electron spin-lattice relaxation times T_1 of both paramagnetic centers have already been measured in the

temperature range from 4K to 20K (see table 1 in Chapter B.2.5). The cytochrome *c* T_1 is much shorter than those of Cu_A (see table 1 in Introduction).

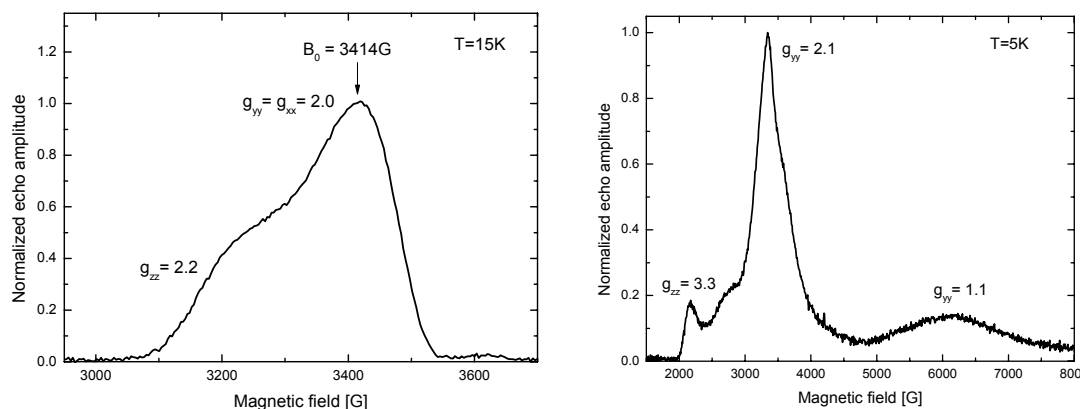


Fig. 18: Electron spin-echo detected field sweep spectra of Cu_A in CcO_{II} (right) and of c_{552} (left). Both metal centers are in the oxidized form. Experimental conditions: mw frequency = 9.72 GHz, mw pulses of length $t_{\pi/2} = 8 \text{ ns}$ and $t_{\pi} = 16 \text{ ns}$ respectively, $\tau = 120 \text{ ns}$.

For two dipole-dipole coupled electron spins with broad EPR spectra, of which one spin relaxes slowly relative to the other spin, as in case of CcO and c_{552} relaxation measurements were the most suitable EPR technique to investigate the magnetic dipole-dipole interaction. Cu_A in CcO_{II} is the slowly relaxing is the observer spin whose relaxation is enhanced by the rapidly relaxing Fe (III) in c_{552}

B.4.1 Relaxation enhancement: indication for complex formation

Electron spin echo decay measurements of Cu_A were recorded in the presence and absence of cytochrome *c* in order to examine the distance and orientation between the binuclear Cu_A center of CcO_{II} and its redox partner cytochrome *c* bound in a protein-protein complex. In this experiment the intensity of a Hahn echo was recorded as a function of the separation time τ between the two pulses at the maximum of the Cu_A signal. The presence of cytochrome causes a significantly faster decay of the echo of Cu_A due to dipole-dipole interaction between the two paramagnetic centers. Figure 19 shows the two-pulse echo decay traces of CcO_{II} alone in comparison with the decay of the CcO_{II} and c_{552} mixture measured under the same conditions (temperature 15K, field position corresponding to $g_{\perp} = g_{xx} = g_{yy}$ of the Cu_A signal).

The significant increase in relaxation rate of Cu_A in CcO_{II} upon addition of c_{552} is clear evidence that complex formation takes place in the mixture of the two proteins.

This confirms a previous observation by NMR spectroscopy that complex formation between the two fully oxidized proteins takes place despite the fact that no electron is transferred to the oxidized Cu_A center [72].

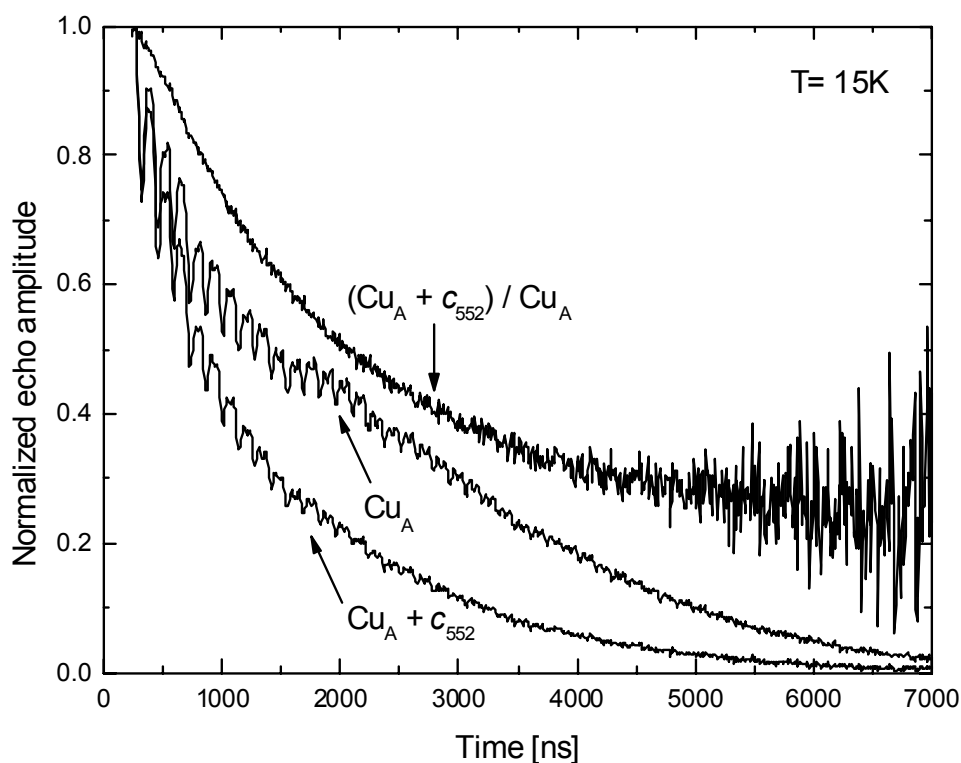


Fig. 19: Electron-spin echo decay traces of: 100 μM Cu_A in CcO_{II} alone (Cu_A) and in a 100 μM : 100 μM mixture with c_{552} ($\text{Cu}_A + c_{552}$). The division of these two time traces yields the pure dipolar relaxation trace $(\text{Cu}_A + c_{552})/\text{Cu}_A$. All measurements performed at a magnetic field value of $B_0 = 3414$ G, microwave frequency $\nu_{\text{MW}} = 9.72$ GHz and a temperature of 15K.

The echo decay traces of Cu_A in presence of cytochrome c are product of dipolar relaxation due to coupling to cytochrome c , the Cu_A intrinsic relaxation and ESEEM modulation. This limits the precision of the data analysis on both qualitative and quantitative level as described in the theory section. Hence, CcO_{II} was measured independently from the CcO_{II} :cytochrome c protein-protein complex and the two experimental traces were divided. This procedure removed all intrinsic relaxation and hyperfine modulation of Cu_A and resulted in extraction of the pure dipolar contribution to the relaxation traces. The division method was applied to all experimental echo decay traces shown further on. The extraction of the pure dipolar relaxation traces was a crucial step in the data analysis and in the monitoring and evaluation of the protein-protein interaction. It permitted a clear distinction between

specific binding and through-space dipole-dipole interactions caused by statistically distributed cytochromes.

Note that, this method has some limitations. It is necessary that the two spins are spectrally separated, i.e., at the detection position on the observer spin there should be no contribution from the rapidly relaxing spin. For cytochrome *c*, which has a very broad spectrum there is no such position on the Cu_A signal. However, as cytochrome *c* is extremely fast relaxing a contribution from its signal only shows up at very low temperature range.

B.4.2 Specific complex formation

The dipole-dipole interaction of Cu_A in CcO_{II} with the Fe of three different cytochromes has been investigated: a soluble fragment of c_{552} , which in the bacterium serves as membrane-anchored electron donor to the oxidase; c_{hh} which is often used as substrate in enzymatic assays for the bacterial oxidase, providing high turnover activity; c_1 a soluble fragment derived from cytochrome bc_1 complex, which for its highly negative surface potential cannot build a specific complex with CcO_{II} and is used for a negative control. The dipolar relaxation traces of Cu_A with these three different cytochromes are shown in Figure 20.

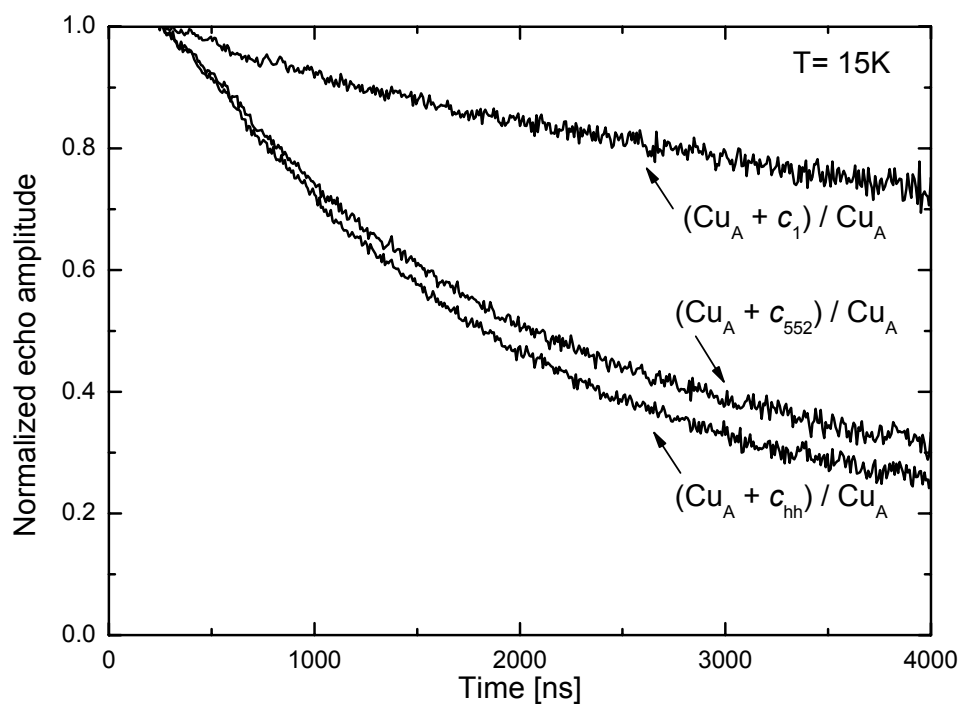


Fig. 20: Dipolar relaxation traces of 100 μM :10 $0\mu\text{M}$ mixtures of CcO_{II} with c_{hh} ($(\text{Cu}_A + c_{\text{hh}})/\text{Cu}_A$), c_{552} ($(\text{Cu}_A + c_{552})/\text{Cu}_A$) and c_1 ($(\text{Cu}_A + c_1)/\text{Cu}_A$). All measurements performed at a magnetic field value of $B_0 = 3414$ G, microwave frequency $\nu_{\text{MW}} = 9.72$ GHz and a temperature of 15K.

As can be seen, the dipolar relaxation traces of the mixtures of CcO_{II} with the binding cytochromes c_{hh} and c_{552} are very similar, and decay much faster than the trace of CcO_{II} and the control protein c_1 . This is as expected because the distance between the two paramagnetic centers for the specifically bound protein-protein complex, according to MD simulations, NMR binding studies and mutation experiments should be in the range of 20 Å. This distance is much shorter than the average intermolecular distance between statistically distributed paramagnetic centers in the protein sample (which is about 250 Å for 100 μM of cytochrome c concentration).

Furthermore, dipolar relaxation traces with higher concentrations of cytochromes mixed with CcO_{II} showed a linear concentration dependence of the decay for c_1 , whereas for the other two cytochromes the dipolar relaxation did not scale with concentration (Figure 21).

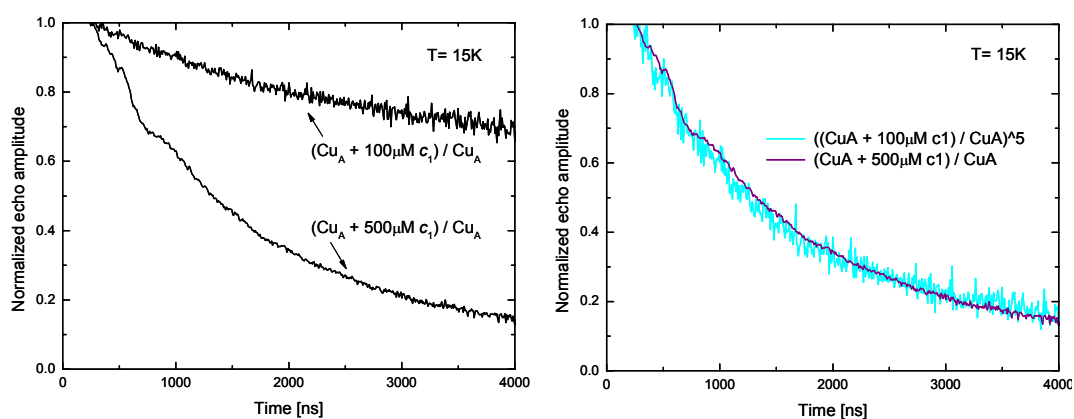


Fig. 21: Original dipolar relaxation traces of mixture of CcO_{II} with c_1 ($(Cu_A + c_1) / Cu_A$) (left panel) and after taking into account the concentration effect (right panel). The concentration of Cu_A in CcO_{II} is 100 μM and the concentration of c_1 is 100 μM and 500 μM respectively. All measurements performed at a magnetic field value of $B_0 = 3414$ G, microwave frequency $\nu_{MW} = 9.72$ GHz and a temperature of 15K.

These results further support the assumption that in the case of c_1 mainly through-space interaction of statistically distributed cytochromes were detected, whereas in the other two cases a much stronger effect from a specific protein-protein complex between CcO_{II} and cytochrome c could be observed.

B.4.3 Temperature dependence

Due to the strong temperature dependence of the T_1 relaxation time of cytochrome c the dipolar relaxation traces should have a strong temperature dependence with a minimum in relaxation time for the condition $1/T_1 = \Delta$, in accordance with theory. The

dipolar relaxation traces in the temperature range 12-23 K of the complex of CcO_{II} with c_{hh} are shown in Figure 22 and with c_{552} in Figure 23.

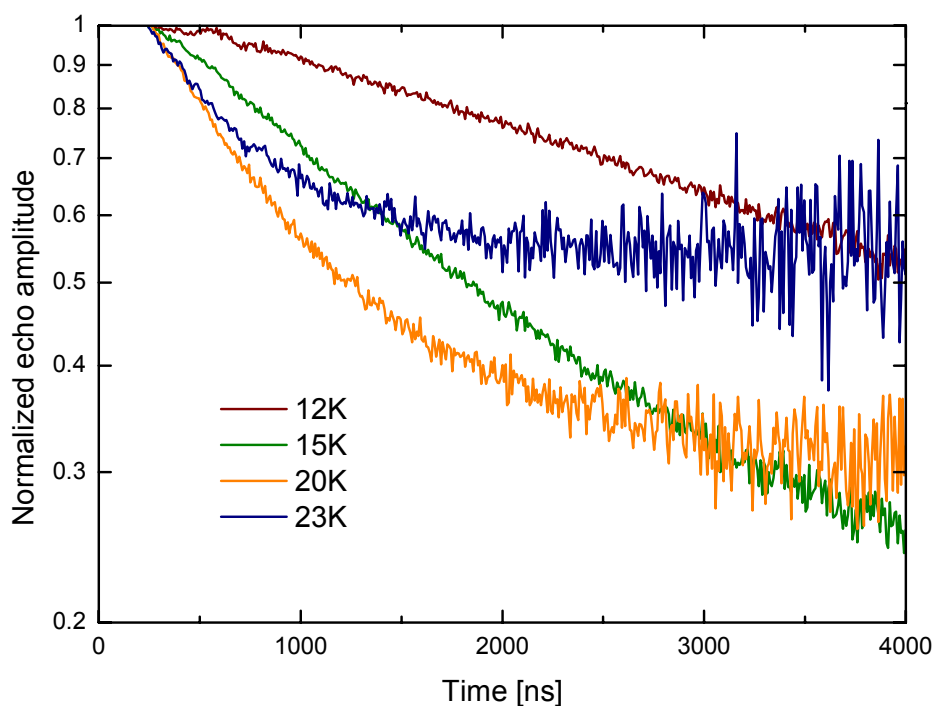


Fig. 22: Semi-logarithmic plot of the dipolar relaxation traces of the 100 μM : 100 μM mixture of CcO_{II} with c_{hh} , measured at different temperatures as indicated in the plot. All measurements performed at a magnetic field value of $B_0 = 3414$ G, microwave frequency $\nu_{MW} = 9.72$ GHz.

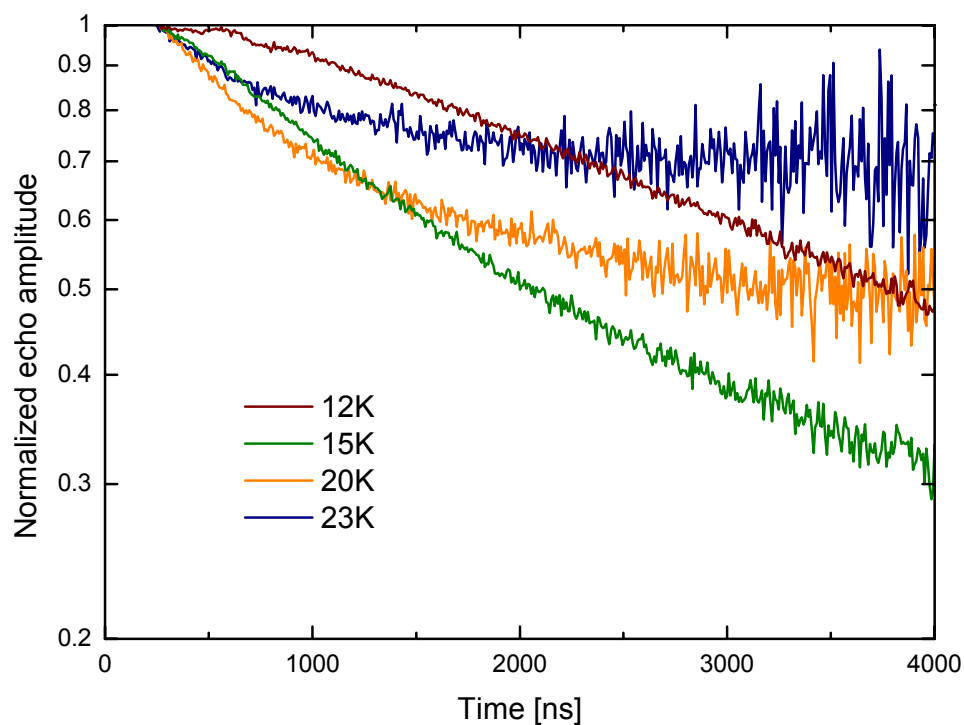


Fig. 23: Semi-logarithmic plot of the dipolar relaxation traces of the 100 μM : 100 μM mixture of CcO_{II} with c_{552} , measured at different temperatures as indicated in the plot. All measurements performed at a magnetic field value of $B_0 = 3414$ G, microwave frequency $\nu_{MW} = 9.72$ GHz.

Both complexes show indeed a pronounced minimum in dipolar relaxation at a temperature of about 15 K. Whereas the low temperature decay trace (12K) is monoexponential, the higher temperature decay traces show strongly nonexponential behavior due to orientation dependence of dipolar coupling.

At higher temperatures the echo decay curve is not a single exponential because the dipolar relaxation is sensitive to Δ . Molecules with many different orientations of the dipolar vector with respect to the magnetic field are excited, i.e., the total dipolar relaxation decay is a sum of the decays of all excited in the experiment orientations.

Despite the similarities of the dipolar relaxation behavior in the complexes with c_{552} and c_{hh} , the temperature dependences are not identical. This will be discussed in more details later on.

It is important to note here that at very low temperature (10K and 12K) a small contribution of nitrogen modulation at the beginning of the dipolar decays is visible and that this causes a slight deviation from monoexponential behavior expected in this temperature range. This is an indication that there is some contribution of the cytochrome signal to the dipolar relaxation decays. Even at 15K the detection of cytochrome c contribution is not avoidable. However, this is not a problem at higher temperature as T_2 of cytochrome c becomes extremely short and no signal contribution is observed. This effect is more strongly pronounced in the dipolar decay traces for higher cytochrome concentrations (Figure 24).

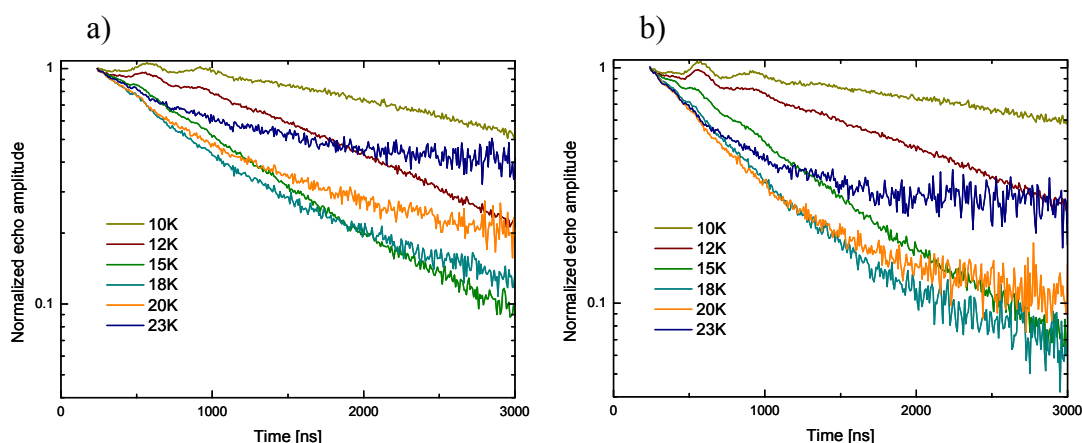


Fig. 24: Semi-logarithmic plot of the dipolar relaxation traces of the 100 μM : 500 μM mixtures of CcO_{II} with a) c_{552} and b) c_{hh} , measured at different temperatures as indicated in the plot. All measurements performed at a magnetic field value of $B_0 = 3414$ G, microwave frequency $\nu_{\text{MW}} = 9.72$ GHz.

The temperature dependence of the echo decay traces for the c_1 mixture, however, is very different (Figure 25). Not only is the strength of the dipolar relaxation much

weaker in this case, but the decay curves are monoexponential at all temperatures and do not show any pronounced minimum in dipolar relaxation. Again this is in agreement with our assumption that c_1 does not form a specific protein-protein complex with CcO_{II} .

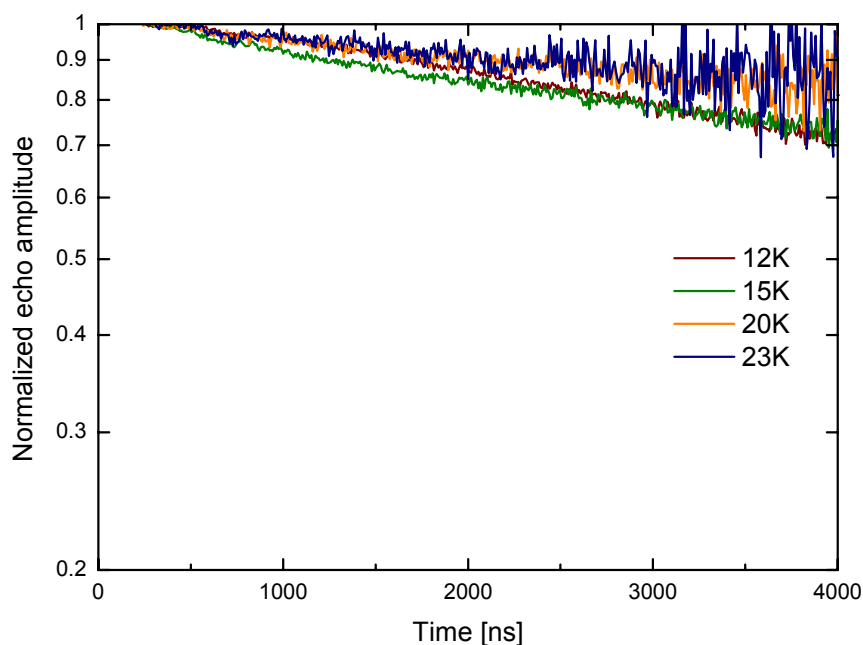


Fig. 25: Semi-logarithmic plot of the dipolar relaxation traces of the of 100 μ M : 100 μ M mixture of CcO_{II} with c_1 , measured at different temperatures as indicated in the plot. All measurements performed at a magnetic field value of $B_0 = 3414$ G, microwave frequency $\nu_{MW} = 9.72$ GHz.

As can be seen the observed relaxation for the mixture of CcO_{II} with c_1 is much weaker than for the specifically bound complexes. Also the linear scaling with concentration is in agreement with through-space interaction of statistically distributed cytochromes. Nevertheless, it should be mentioned that the decay curves are somewhat faster than a pure statistical distribution would account for. This increased relaxation could reflect a slightly enhanced probability to find the proteins close to each other, which could be described by inelastic scattering of the proteins in solution.

The temperature dependences of the echo decay traces of the complexes with c_{552} and c_{hh} are qualitatively similar but not identical. The difference in the temperature dependence displayed by the protein-protein complex of CcO_{II} with c_{hh} and c_{552} , respectively probably reflects structural differences between the two protein-protein complexes. Two alternative models could be proposed in order to explain the experimentally observed differences:

The first possibility is that the complexes observed are the active complexes with one single well-defined geometry that is optimized for efficient electron transfer. If this is the case, different binding geometries of the two cytochromes (meaning different orientation and/or distance) in the complexes may lead to a different temperature dependence of the dipolar traces.

A second possible explanation is that in case of c_{552} only the encounter complexes are detected in our echo decay experiments. In the encounter complex cytochrome c does not bind in a single well-defined structure, it assumes many different orientations. As slight distribution of distances and orientations would account for its less pronounced (averaged out) temperature dependence. It is also possible that a mixture of both electron transfer and encounter complexes are present which would lead to similar effect of averaging out the temperature dependence of the dipolar relaxation as a broader distribution of distances and orientations is detected.

It is important to note that the existence of an ensemble of complexes with different geometries leads to complication of the quantitative analysis of the corresponding dipolar relaxation traces and therefore the extraction of such parameters as distance and orientation between the various paramagnetic centers might be very difficult.

Different loose complexes may also be form between CcO_{II} and c_{hh} . The difference in temperature dependence between the two cytochromes is caused by differences in distributions of distances and orientation. On the other hand, c_{hh} might assume some preferential conformation which leads to strongly pronounced dependence of the dipolar relaxation. It cannot be excluded that the membrane anchor of c_{552} plays an important role in stabilization of the effective electron transfer complex, especially considering that a super complex, consisting of c_{552} complexed with the bc_1 complex and CcO has been isolated [48].

The existence of a highly dynamic protein-protein complex between CcO_{II} with c_{552} and c_{hh} is in agreement with the relatively small chemical shift-changes upon complex formation previously observed by NMR spectroscopy. This was attributed to the fact that various loose complexes exist rather than one specific electron transfer complex between CcO_{II} with c_{552} . A very low affinity (no binding constant reported) was given as an alternative explanation for the NMR results, which may be related to the lack of the membrane anchor of c_{552} and the fact that in nature both proteins are membrane-embedded [72]. Resent docking studies using this NMR results and the result from mutagenesis and kinetic investigations also point to the existence of many different

complexes of which only some are favorable for electron transfer and suggested that the complex may have considerable dynamic features. In fact, in these docking calculations four clusters of structural solutions were found [75].

B.4.4 Concentration dependence

For quantitative simulations pure dipolar relaxation traces due to 1:1 complex formation are necessary. To evaluate that 1:1 complex formation takes place, echo decay experiments were performed on samples with a constant concentration of $100\mu\text{M}$ Cu_A and varying concentrations of cytochrome: $50\mu\text{M}$, $100\mu\text{M}$ and $500\mu\text{M}$. The concentration dependence of the dipolar relaxation is shown in Figure 26.

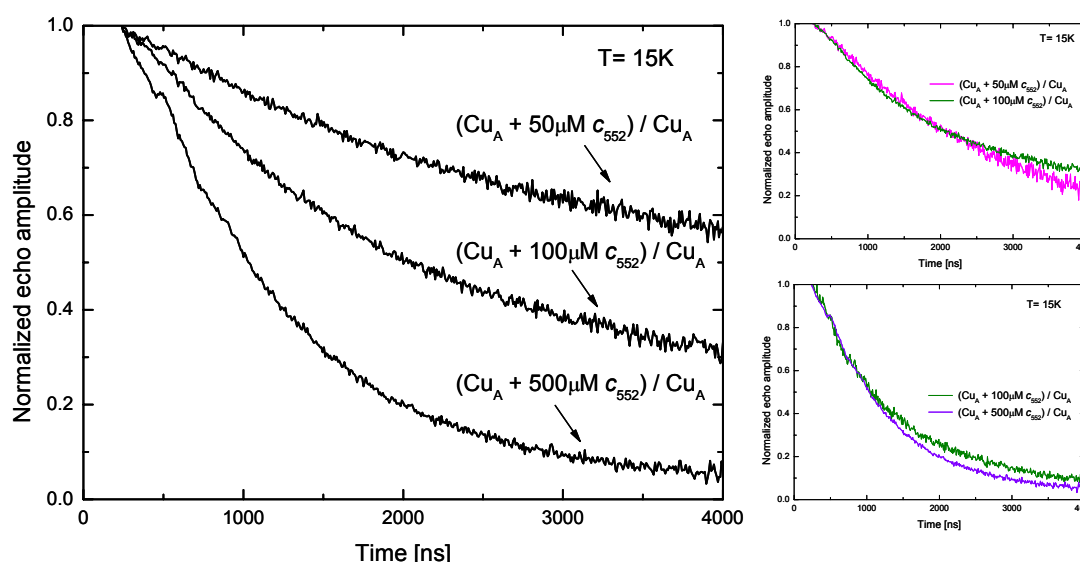


Fig. 26: a) Dipolar relaxation traces of mixture of CcO_{II} with c_{552} ($(\text{Cu}_A + c_{552})/\text{Cu}_A$). The concentration of Cu_A in CcO_{II} is $100\mu\text{M}$ and the concentration of c_{552} is $50\mu\text{M}$, $100\mu\text{M}$ and $500\mu\text{M}$ respectively (left panel); $(\text{Cu}_A + 50\mu\text{M } c_{552})/\text{Cu}_A$ after offset correction to account for unbound CcO_{II} (right panel top); $(\text{Cu}_A + 100\mu\text{M } c_{552})/\text{Cu}_A$ after correction to account for the concentration effect (right panel top). All measurements performed at a magnetic field value of $B_0 = 3414\text{ G}$, microwave frequency $\nu_{\text{MW}} = 9.72\text{ GHz}$ and a temperature of 15K .

The results show that a 1:1 complex is formed in the $100\mu\text{M}:100\mu\text{M}$ protein mixture. This is confirmed by the dipolar decays corresponding to $100\mu\text{M}:500\mu\text{M}$ which show faster decay due only to the higher cytochrome concentration. The 1:1 decay can be rescaled to that of the 1:5 mixture after taking into account the concentration effect (through-space intermolecular dipole-dipole interaction of randomly distributed cytochromes). This is taken into account by using the dipolar relaxation traces of the 1:1 mixture with c_1 . The fourth power of the $100\mu\text{M}:100\mu\text{M}$ mixture of CcO_{II} and c_1 trace (to account for the $400\mu\text{M}$ extra cytochrome in the sample) is multiplied with

the 1:1 mixture of c_{552} and CcO_{II} trace and compared to the 1:5 mixture of CcO_{II} and c_{552} trace (Figure 26 right panel top). Evidence for formation of 1:1 complexes is also found in measurements with 100 μ M: 50 μ M mixtures where a slower decay was observed with an offset corresponding to the percentage of unbound CcO_{II} . This decay can be almost rescaled to the 1:1 mixture after subtraction of the offset (Figure 26 right panel bottom). In this case the deviation is bigger which is probably due to the uncertainties in the concentration of the proteins as a very small amounts of cytochrome were pipetted. The rescaled traces are not exactly on top of the 1:1 which is most probably caused by errors in sample concentration.

The pure dipolar relaxation traces are extremely sensitive to the concentration of the two proteins in the mixture. An excess of CcO_{II} in the mixture leads to an offset after the division procedure, an excess of cytochrome results in faster decay. Although the concentrations of the stock solutions of the two proteins were determined with high precision (upper error limit 10%), an error up to 15% could be introduced due to pipeting errors while mixing the samples, which leads to unwanted offset. Therefore, an additional offset may have to be taken into account in the quantitative analysis. This means that the precision of the method in distance determination by quantitative simulations of the dipolar relaxation decays depends critically on the precision of the concentration of the two proteins after mixing. However, at low temperature (12K) the dipolar trace decays with T_1 of the fast relaxing spin and it could be used to help and determine the offset.

Observation of 1:1 complex formation and its concentration dependence on the level described above was possible only after addition of glycerol to the samples otherwise aggregation of the proteins occurred causing problems to quantify the concentration dependences.

It has to be also mentioned here that all echo decay experiments were performed with samples of both cytochromes at very low ionic strength to enforce complex formation and obtain stoichiometric 1:1 complex. This might also be a cause for formation of loose complexes.

B.4.5 Orientation dependence

The dipolar coupling depends on the angles (θ_D , ϕ_D) of the dipolar vector with respect to the magnetic field. Additional orientation dependence is introduced by the strongly anisotropic g tensor of the cytochrome, leading to an effective g value that depends

strongly on the specific orientation of the cytochrome with respect to the dipolar vector. Therefore, anisotropy of the dipolar relaxation over the EPR spectrum is expected at high temperatures where it is sensitive to Δ . Good orientation selectivity is required for this purpose. At X-band the Cu_A g- tensor is not fully resolved and in particular due to the Cu_A special hyperfine features it is not possible to selectively excite small fractions of spins. Nevertheless, echo decay measurements at 20K have been performed at different field position to probe for anisotropy of the dipolar relaxation. The corresponding traces are shown in Figure 27.

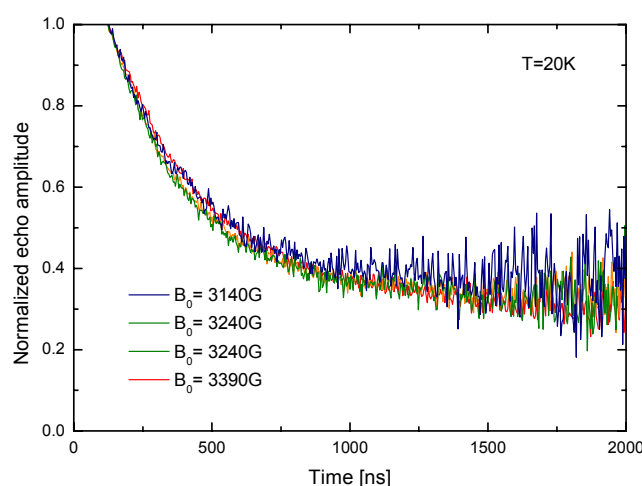


Fig. 27: Dipolar relaxation traces of 100 μM :100 μM mixture of CcO_{II} with c_{hh} ($(\text{Cu}_A+c_{\text{hh}})/\text{Cu}_A$). The measurements were performed at various magnetic fields as indicated in the plot, microwave frequency $\nu_{\text{MW}} = 9.68$ GHz and a temperature of 20K.

The results clearly show that within the signal to noise there is no dipolar relaxation anisotropy is observed. Although it is very difficult to draw conclusions about the nature of the protein-protein complex based only on these low frequency data (as no large relaxation anisotropy is expected here) it seems more probable that a rather flexible complex instead of one single well defined complex could be the reason for the completely averaged out dipolar relaxation anisotropy. It could, however not be excluded that the relaxation anisotropy is very small and X-band frequency is not sensitive enough to detect due to the lack of the orientational selectivity. This is the limitation of the standard X-band frequency. Therefore it necessary to perform the same experiments at higher magnetic fields where the g-tensor is resolved due to the increased Zeeman splitting. Experiments at high magnetic field could therefore clarify if only one single complex is formed or if there are many different complexes, as anisotropy of the dipolar relaxation would be expected only for a well-defined complex of CcO and cytochrome c .

B.4.6 Influence of ionic strength

In order to probe specificity of complex formation experiments were performed after adding 10mM NaCl to the samples to increase the ionic strength to the optimum known for maximum electron transfer between Cu_A and c_{552} [65,70]. The result from the echo decay measurements performed at different temperatures of the both mixtures Cu_A with c_{552} and c_{hh} are shown in Figure 28.

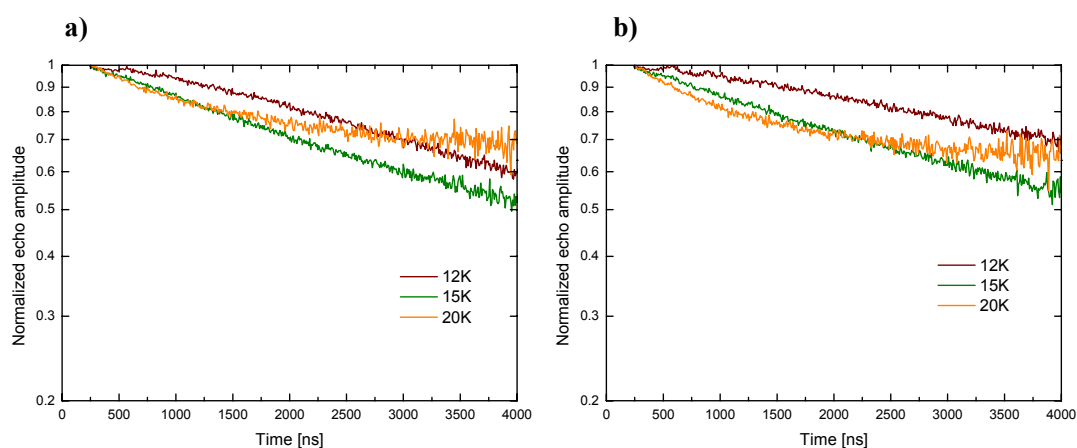


Fig. 28: Semi-logarithmic plot of the dipolar relaxation traces of the of 100 μ M : 100 μ M with 10mM NaCl mixtures of CcO_{II} with c_{552} (a) and c_{hh} (b), measured at different temperatures as indicated in the plot. All measurements performed at a magnetic field value of $B_0 = 3414$ G, microwave frequency $\nu_{MW} = 9.72$ GHz.

The dipolar relaxation traces are difficult to analyze because of the drastically increased offset corresponding to the fraction of unbound proteins due to the decreased affinity. However, on a qualitative level it is still possible to draw some conclusions. The dipolar decay traces display only a slight shape change which might account only for a change in the equilibrium from the encounter complex (most probably predominantly present at low ionic strength) towards the more specific electron transfer complex, i.e., the population of the two states changes. It does not seem that the equilibrium is completely shifted to the active electron transfer complex as then the was a case the shorter distance expected for an efficient ET complex would lead to much faster decay in the beginning of the decay traces. All these arguments could be indications that this complex is highly dynamic.

It is worth mentioning that at higher ionic strength c_{hh} displays a very similar temperature dependence to that of c_{552} . This would be an indication that at high I the complex with c_{hh} is more flexible and would support the idea that at low I , due to its higher positive charge, some more preferred orientations of c_{hh} within the complex

exist, which are electrostatically stabilized but not suitable for ET. In addition, the fraction of complex formed with c_{hh} is less than that with c_{552} at high ionic strength, while they are bound in approximately the same amount at low I . At higher ionic strength the specificity of protein interactions is predominant and as c_{552} is the homologous electron donor it might form complex in bigger amount.

The c_{552} complex is characterized by high flexibility at both ionic strengths. At low ionic strength (electrostatic forces are mainly responsible for protein interaction) this may be because only or predominantly encounter complex is formed. This would be surprising at higher ionic strength though, since the maximum electron transfer rate due to formation of a redox active complex has been observed to be at 15mM by kinetic experiments [70].

From all EPR results it seems that this particular complex of c_{552} is highly dynamic, the encounter and ET complexes are in very fast exchange i.e. the energy minimum is very broad, because of functional reasons. As we work with frozen samples (a snapshot), both encounter complexes in many orientations and ET complex in one single orientation contribute to the relaxation traces. Their ratio could change depending on ionic strength.

B.4.7 Full-size CcO:cytochrome *c* complex

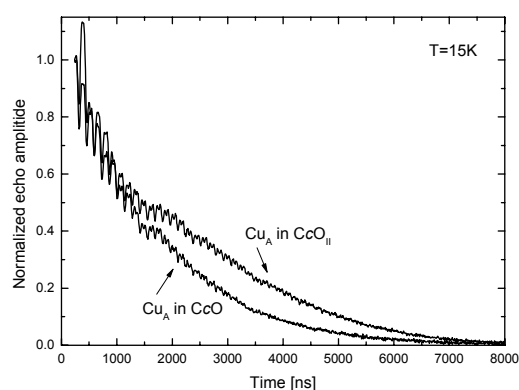


Fig. 29: Electron spin-echo decay traces of: 100 μ M Cu_A in CcO_{II} and in CcO . The measurements performed at a magnetic field value of $B_0 = 3414$ G, microwave frequency $\nu_{MW} = 9.72$ GHz and a temperature of 15K.

In the full-size CcO three additional paramagnetic centers are present: heme a , Cu_B and heme a_3 . Cu_B and heme a_3 form the binuclear center of the enzyme and are antiferromagnetically coupled. Heme a is a fast relaxing spin and introduces additional relaxation to the Cu_A since it is located close enough to enhance the Cu_A

relaxation due to dipolar interaction with the later. In fact this distance is very close to the one predicted for the $CcO:c_{552}$ complex. As a result, the two pulse echo decay traces of Cu_A in CcO are faster compared to these of Cu_A in CcO_{II} (Figure 29).

Echo decay experiments were also performed to investigate the complex formation between full-size CcO and cytochrome c . The echo decays of Cu_A in CcO have been measured in presence and absence of cytochrome c . Relaxation enhancement of Cu_A in CcO upon addition of cytochrome c has been detected (Figure 30).

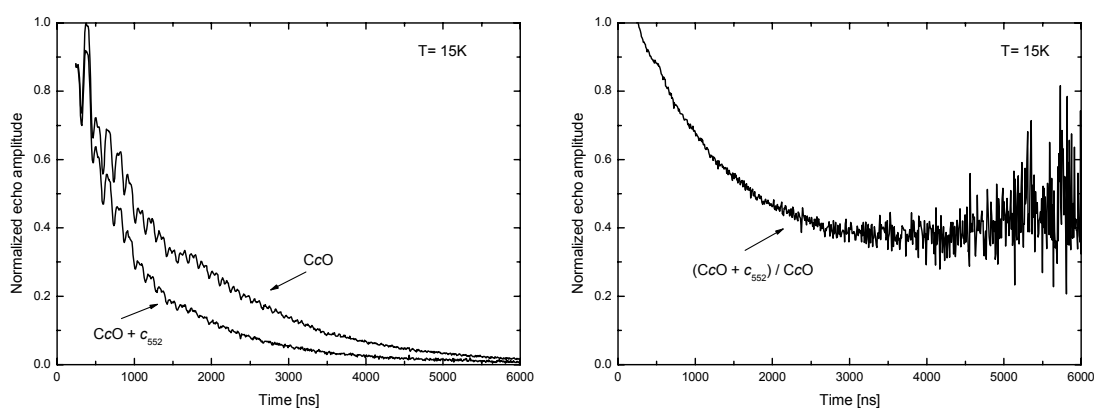


Fig. 30: Electron spin-echo decay traces of: 100 μM Cu_A in CcO alone (CcO) and in a 50 μM : 100 μM mixture with c_{552} ($CcO + c_{552}$). The division of these two time traces yields the pure dipolar relaxation trace $(CcO + c_{552})/CcO$. All measurements performed at a magnetic field value of $B_0 = 3414$ G, microwave frequency $\nu_{MW} = 9.72$ GHz and a temperature of 15K.

These experiments showed that the division method also in this case removes all the contributions of the internal paramagnetic centers in CcO to the Cu_A signal, and retains only the dipolar relaxation due to the external paramagnetic center (cytochrome c). This is only valid if the system of interest can be measured in the presence and in absence of one additional fast relaxing paramagnetic center. This is very important if this method is used for investigations of supercomplexes for example. The dipolar relaxation traces in the temperature range 12-23 K of the complexes of CcO with c_{hh} and c_{552} are shown in Figure 31. The dipolar relaxation traces for both complexes show temperature dependences very similar to those of the complexes between CcO_{II} and c_{552} or c_{hh} which is an indication that there are no structural differences in the complexes formed with the soluble subunit II and full-size oxidase.

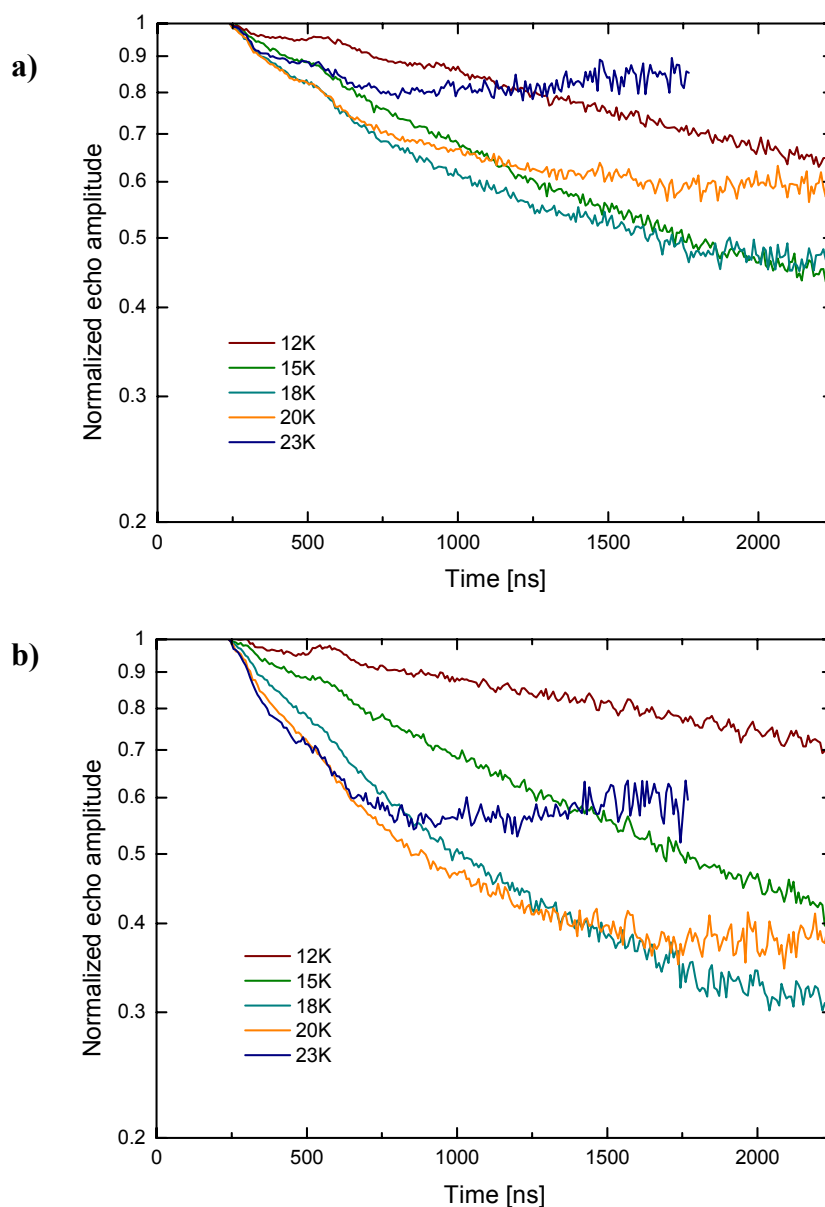


Fig. 31: Semi-logarithmic plot of the dipolar relaxation traces of the of 50 μM : 100 μM mixtures of CcO with a) c_{552} and b) c_{11h} , measured at different temperatures as indicated in the plot. All measurements performed at a magnetic field value of $B_0 = 3414$ G, microwave frequency $\nu_{\text{MW}} = 9.72$ GHz.

However, in this case a 2-fold excess of cytochrome c was required. Using mixtures of 1:1 ratios of protein concentrations was not sufficient as a less relaxation enhancement on Cu_A was observed in comparison to the one of Cu_A in CcO_{II} with cytochrome c . This was an indication that most of the oxidase is in the unbound state. This might be caused by less accessibility due to the bigger size of the full-size oxidase. Additionally, the concentration of the CcO had to be decreased by factor of two as some clustering of the oxidase molecules was still detected if the concentration

was kept as with the CcO_{II} . The latter is something one has to be aware of and keep in mind while dealing with biomolecules and using this method.

Beside of that this was a very promising result as it shows that this method could be more generally applied to biological systems which are known to contain many different paramagnetic centers. It could be used not only to study protein-protein interaction but also distances within one biomolecule which posses two paramagnetic centers if the fast relaxing one could be turn to a diamagnetic state.

B.4.8 Dipolar relaxation within CcO

The distance between Cu_A and heme a in CcO is known from the enzyme crystal structure to be 19.5 \AA and heme a is a fast relaxing spin in comparison to Cu_A (see table 1 in Chapter B.2.5). Therefore CcO seemed to be a good system with fixed distance and orientation between the two paramagnetic centers on which relaxation experiments can be applied to determine the dipole-dipole interaction between Cu_A and heme a . Especially as the distance between Cu_A and heme a is in the same range as the one predicted between Cu_A and cytochrome c in the protein-protein complex it was thought that it could be used as a closely related calibration model in the quantitative analysis of dipolar relaxation.

Unfortunately, it was not possible to extract the dipolar contribution to the echo decay traces (Figure 32).

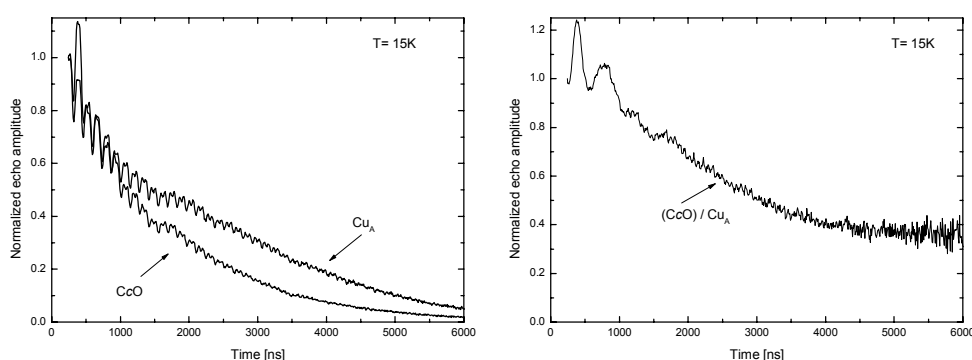


Fig. 32: Electron spin-echo decay traces of $50 \mu\text{M}$ Cu_A in CcO (CcO) and of $100\mu\text{M}$ Cu_A in CcO_{II} (Cu_A). The division of these two time traces does not yield the pure dipolar relaxation trace $(CcO)/Cu_A$. All measurements performed at a magnetic field value of $B_0 = 3414 \text{ G}$, microwave frequency $\nu_{MW} = 9.72 \text{ GHz}$ and a temperature of 15K .

The division of the Cu_A from CcO echo decay trace to the echo decay trace of Cu_A from CcO_{II} resulted in decay traces which still had contribution of nitrogen ESEEM modulation left i.e. the echo decay traces after division are not only affected by the

dipolar coupling between the two paramagnetic centers and therefore not suitable for analysis.

These experiments have shown that the magnetic properties of Cu_A in the full-size oxidase differ to some extent from those of Cu_A in CcO_{II} . As only a very small change in the nitrogen hyperfine coupling is observed with this extremely sensitive method, most probably it is due to a slight difference in the binding geometry of the binuclear copper centers. This might be because subunit II is cut off at the Mg/Mn binding site which shares a ligand with the Cu_A site. However, the Cu_A g tensor detected was typical for mixed valence binuclear copper center and is evidence that only a very slight change in the coordination sphere must have occurred.

Finally, it could not be excluded that Cu_B and heme a_3 although antiferromagnetically coupled, might cause additional relaxation enhancement and thus contribute to the echo decay traces. They possess a total spin $S = 2$ and are located at about the same distance to the Cu_A as heme a .

B.4.9 Quantitative analysis

Simultaneous fits of the dipolar decay traces for all temperatures were performed to investigate the protein complex structure. A number of structures were found with a similar quality of the fit as shown in Figure 33, assuming a single binding geometry of the complex. The R values of these fit structures range from 1.6 up to 4 nm for different but very specific values of the exchange coupling J and dipolar and cytochrome angles. However, we discard all these solutions since they predict pronounced anisotropy of the relaxation traces at high-field (G-band) frequency, which is not observed in the experiments [personal communications M. J. M. Penning de Vries and T. Prisner]. The lack of relaxation anisotropy at X-band and particularly at G-band can be attributed to the existence of complex ensemble with multiple geometries e.g. cytochrome c orientations, dipolar angles or distances. To test this hypothesis, a simple model with two distinct binding sites was incorporated in the fitting procedure. This led to even more free parameters, but nevertheless a pronounced minimum was repetitively found for fits with random starting values. One distance was always in the range of 1.8 - 2.3 nm and a second long distance was found with approximately 4 nm. The populations of the two sites varied between 1:1 and 2:1, depending on the fit procedure starting values. One solution obtained by such

a fit is overlaid with the experimental traces in Figure 33 together with the parameters.

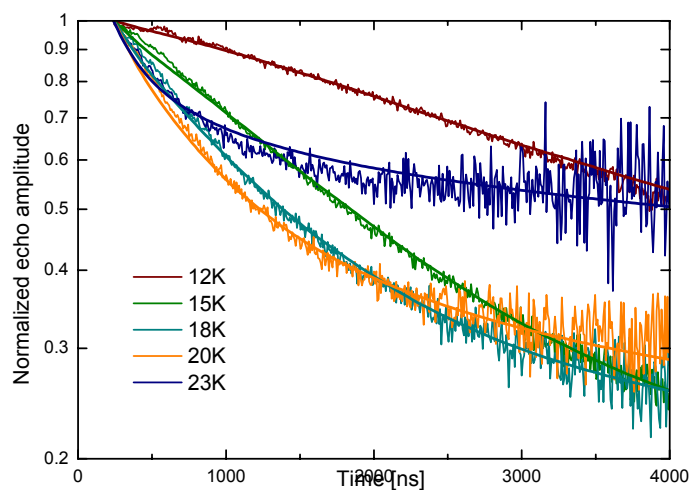


Fig. 33: Experimental X-band relaxation traces of $100 \mu\text{M} : 100 \mu\text{M}$ mixtures of CcO_{II} with c_{hb} , measured at different temperatures as indicated in the plot together with simulations (noiseless lines). The fit parameters are: dipolar angles: $\theta_{\text{D}} = 54^\circ$, $\varphi_{\text{D}} = 11^\circ$, distance Fe to center Cu-Cu: $R_1=2.3 \text{ nm}$, $R_2=4 \text{ nm}$, Euler angles: set 1= $(27,6,29)^\circ$, set 2= $(90,57,12)^\circ$, relative amplitudes of both structures : $A_1=1.2$, $A_2=1$, unbound $\text{CcO}_{\text{II}}=11\%$.

The two observed states with distances of 2 and 4 nm may represent the two states of a transient protein-protein complex as proposed in the two-step model of complex formation between electron transfer proteins [47, 63, 72]

Another possibility is that the protein complex consists of a dynamic ensemble of conformations with distances in the range of 2-4 nm with not one single electron transfer complex, but where an electron is transferred whenever the two redox centers are close enough [35, 75].

B.5 Summary and Outlook

For the first time pulse EPR techniques were used successfully to study the interaction between electron transfer proteins. Electron spin echo measurements of the slower relaxing Cu_A paramagnetic center in the soluble subunit II of Cytochrome *c* Oxidase in complex with different cytochromes were performed, allowing a clear distinction between binding and non binding cytochromes. The division method provides pure dipolar relaxation traces which can be quantitatively analyzed such that details of the structure of a protein-protein complex can be obtained without the necessity of taking the intrinsic relaxation properties of the observed paramagnetic species into account.

In the investigated system the temperature dependence of the dipolar relaxation traces suggest that a broad distribution of complex structures is observed in the EPR experiments rather than a single well defined conformation of the protein-protein complex. This is very strong indication that this particular protein-protein complex is of highly pronounced dynamic nature. Quantitative simulations of the data suggest that a broad distribution in distances (2 - 4 nm) and orientations between the Cu_A and Fe(III) exists in the complex between CcO and cytochrome *c*.

It has been demonstrated experimentally in this work that complementary to the PELDOR method, the relaxation method can be applied to spectrally broad paramagnetic centers in coupled spin pairs, where one of the spins is extremely fast relaxing. Therefore dipolar interaction between natural metal centers in enzymes can be directly measured.

Additionally it is possible to apply this method to protein complexes, where more than two paramagnetic centers are involved. It has been demonstrated experimentally on the complex of cytochrome *c* with full-size CcO that also in this case the division method removes all the contributions of other internal paramagnetic centers in CcO to the Cu_A signal and retains only the dipolar relaxation due to external cytochrome *c*. Therefore, the relaxation method could be in future applications used for studying also membrane embedded and larger protein complexes.

Summary

One of the central research topics in the field of biophysical chemistry is the structure and function of membrane proteins involved in energy transduction. Both, the aerobic and the anaerobic respiration include electron transfer and proton translocation across the mitochondrial and bacterial membranes. These electron transfer processes lead to changes in oxidation states of cofactors some of which are paramagnetic. Therefore, EPR spectroscopy is the method of choice to obtain electronic and structural information directly related to the function of the respiratory chain proteins. In this work, multifrequency continuous wave (CW) and pulsed EPR spectroscopy has been used to characterize the molybdenum active site of polysulfide reductase (Psr) from the anaerobic bacterium *Wolinella succinogenes* and the protein-protein complex between cytochrome *c* oxidase (CcO) and cytochrome *c* from the aerobic bacterium *Paracoccus denitrificans*.

Molybdenum in Psr

Psr is an enzyme essential for the sulfur respiration of *Wolinella succinogenes*. Biochemical studies suggested that the active site of this enzyme contains a mononuclear Mo center, which catalyzes the reduction of the substrate polysulfide to sulfide. Until now there is no crystal structure available for Psr. Consequently, current characterizations of this enzyme have to rely on biochemical and spectroscopic investigations. Within the present work, CW and modern pulsed EPR techniques were applied to investigate its catalytically active site.

In the first part of this thesis, different redox agents have been used to generate paramagnetic states of Psr. Multifrequency CW-EPR spectroscopy was applied to identify the Mo(V) states. Using simulations of the experimental spectra, three spectroscopically distinct states have been identified based on the Mo hyperfine- and g-tensor values. Comparison of their EPR parameters with those of related enzymes indicated five or six sulfur ligands at the Mo center depending on the state. The state generated by addition of polysulfide is suggested to be the catalytically active form, in which the Mo is coordinated by a sulfur of the polysulfide chain as the sixth ligand. ^{33}S ($I = 3/2$) labeled polysulfide was prepared to probe the proximity of the polysulfide to the molybdenum center via its hyperfine coupling. 1D-ESEEM and 2D-

HYSCORE spectroscopy was used to detect these hyperfine and quadrupole interactions, which are too small to be observed in conventional CW EPR spectra. To date there has been only one pulsed-EPR study involving a ^{33}S nucleus [Finazzo et.al. 2003]. The reasons are that this nucleus has a high nuclear spin of $I = 3/2$ and a large nuclear quadrupole moment in addition to the low Larmor frequency. All these make the detection of sulfur and the extraction of structural information demanding. However, analysis of the 2D-data led to a Mo(V) ^{33}S distance in a range of about 2 to 2.5 Å. Mo-S distances found in molybdenum enzymes of the same family are in a range of 1.8 to 2.8 Å suggesting that the ^{33}S is indeed the sixth ligand of the Mo(V) center and demonstrating that polysulfide is the actual substrate for this enzyme. Thus HYSCORE experiments have been proved to be a powerful technique to gain further insight into the active site structures of molybdenum enzymes and the trafficking of substrate atoms during catalysis. Density functional theory (DFT) calculations together with quantitative numerical simulations of the 2D-data will help to obtain more structural details about the molybdenum binding site in Psr.

CcO:cytochrome c complex

Protein-protein complex formation is an important step in energy conversion biological processes such as respiration and photosynthesis. These protein-protein complexes are involved in long range electron transfer reactions and are known to be of transient nature. Within the bacterial and mitochondrial respiratory electron transport chains such a complex is formed between CcO and cytochrome *c*. Upon complex formation cytochrome *c* donates the electrons required for the CcO catalyzed reduction of dioxygen to water. Here, the protein-protein complex formation between CcO and cytochrome *c* from *Paracoccus denitrificans* was investigated by pulsed EPR spectroscopy. The idea was to use the relaxation enhancement due to the distance and orientation dependent magnetic dipole-dipole interaction between the paramagnetic centers in the different CcO constructs and cytochromes.

Two-pulse electron spin echo experiments were carried out on mixtures of the Cu_A containing soluble subunit II or the full size CcO with the physiological partner cytochrome c_{552} or horse heart cytochrome *c*. Significantly enhanced relaxation of Cu_A due to specific protein-protein complex formation has been observed in all four cases. In contrast the non-binding cytochrome c_1 showed only a very weak relaxation enhancement due to unspecific protein-protein interactions. The echo decays of the

slowly relaxing observer spin (Cu_A of CcO) measured in the absence and presence of the fast relaxing spin (Fe(III) of cytochrome c) permitted the extraction of the pure dipolar relaxation contributions for the different complexes. Measurements at different temperatures proved the dipolar nature of the relaxation enhancement. Furthermore, it was demonstrated experimentally that this approach also works for the full-size CcO , which contains four paramagnetic metal centers, in complex with cytochrome c .

Quantitative simulations of the data suggest a broad distribution in distances (2 - 4 nm) and orientations between the Cu_A and Fe(III) in the complex between CcO and cytochrome c . High-field EPR spectroscopy will be useful to further analyze and prove these complex structures.

Within the present work, it has been shown that pulsed relaxation enhancement experiments can be used to investigate the distance and relative orientation between paramagnetic metal centers. Furthermore, it has been demonstrated on a qualitative level, that this method can be used complimentary to other biophysical approaches to study transient electron transfer protein-protein complexes. Finally, within this work it has been proven that this method can be applied also to biological systems where more than two paramagnetic centers are present. This is particularly interesting for supercomplexes between membrane proteins.

List of publications

T. Prisner, S. Lyubenova, Y. Atabay, F. MacMillan, A. Kröger, O. Klimmek: Multifrequency cw-EPR investigation of the catalytic molybdenum cofactor of polysulfide reductase from *Wolinella Succinogenes*, *JBIC*, 2003, 8, 419

K. Budiman, A. Kant, S. Lyubenova, O. Richter, B. Ludwig, H. Michel, F. MacMillan: Tyrosine 167: The origin of the radical species observed in the reaction of cytochrome *c* oxidase with hydrogen peroxide in *Paracoccus denitrificans*, *Biochemistry*, 2004, 43, 11709

S. Lyubenova, K. Siddiqui, M. J. M. Penning de Vries, B. Ludwig, T. Prisner: Binding of cytochrome *c* to cytochrome *c* oxidase characterized by multi-frequency pulse EPR spectroscopy, 2006, Manuscript in preparation

S. Lyubenova, O. Klimmek, T. Prisner: Direct detection of a sulfur ligand to the molybdenum center of polysulfide reductase from *Wolinella Succinogenes* by HYSCORE spectroscopy, 2006, Manuscript in preparation

List of posters presented

S. Lyubenova, F. MacMillan, K. Budemann, H. Michel and T. Prisner: A tyrosine radical in cytochrome *c* oxidase?
Joint meeting of the French and German Biophysicists- Biophysical aspects of electron and proton transfer, 2001, Hünfeld, Germany

S. Lyubenova, F. MacMillan, O. Klimmek and T. Prisner: EPR studies of the molybdenum center of polysulfide reductase from *Wolinella Succinogenes*
6th European Conference on Bioinorganic Chemistry (EROBIC), 2002, Lund, Sweden

S. Lyubenova, F. MacMillan, O. Klimmek and T. Prisner: Pulse and CW-EPR studies on the molybdenum center of polysulfide reductase from *Wolinella Succinogenes*
Gordon Research Conferences - Molybdenum and Tungsten Enzymes, 2003, Kimball Union Academy, USA, *Poster and Invited talk*

S. Lyubenova, M. J. M. Penning de Vries, K. Siddiqui, B. Ludwig and T. Prisner: Binding studies of cytochrome *c*₅₅₂ to CcO as measured by multi-frequency relaxation measurements
5th Meeting of the European EPR groups, 2003, Lisbon, Portugal

S. Lyubenova, F. MacMillan, O. Klimmek and T. Prisner: Pulse and CW-EPR studies on the molybdenum center of polysulfide reductase from *Wolinella Succinogenes*
5th Meeting of the European EPR groups, 2003, Lisbon, Portugal

M. J. M. Penning de Vries, S. Lyubenova, K. Siddiqui, B. Ludwig and T. Prisner: Cytochrome *c* and cytochrome *c* oxidase: distance measurements using multifrequency pulsed EPR

1st Joint German/British Bioenergetics Conference- Mechanisms of Bioenergetic Membrane Proteins: Structures and Beyond, 2005, Naurod, Germany

S. Lyubenova, M. J. M. Penning de Vries, K. Siddiqui, B. Ludwig and T. Prisner: Binding of cytochrome *c* to cytochrome *c* oxidase: distance determination by dipolar relaxation

European EPR summer school, 2005, Naurod, Germany

S. Lyubenova, O. Klimmek and T. Prisner: HYSCORE on the molybdenum center of polysulfide reductase from *Wolinella Succinogenes*

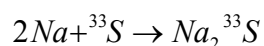
12th International Conference on Biological Inorganic Chemistry (ICBIC), 2005, Ann Arbor, USA

Methods and Materials

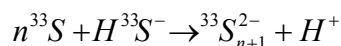
A.6)

A.6.1 Sample preparation

W. succinogenes was grown as reported previously in ref. [25-28], followed by purification of PsrABC complex according to ref. [32]. The EPR samples were prepared under anaerobic conditions (nitrogen or argon) by freezing of ca. 100 μ L of sample in quartz EPR tubes (o.d. 4mm Wilmad). Psr concentration was usually 130-150 μ M. The following redox agents were used to either oxidize or reduce the protein: Na₂S (200 μ M - 6mM), Na₂S₂O₄ (2mM), NaBH₄ (20mM), polysulfide (S_n) (50 μ M – 2mM) in sulfide containing solutions. The ³³S isotope labeled polysulfide (2mM) in sulfide containing solution was used in the labeling experiments. The enzyme concentration was 100 μ M. The elemental sulfur was obtained from Isoflex USA (³³S enrichment of 99%). The Na₂³³S was prepared according to the reaction [127]:



The ³³S isotope labeled polysulfide was obtained by mixing the elemental sulfur with the Na₂³³S according to the reaction:



In order to better dissolve the elemental sulfur a Glycin buffer at pH=10 was used and the mixture was heated up to 37°C.

A.6.2 EPR spectroscopy

CW-EPR: The X-Band CW-EPR spectra were recorded on a Bruker ESP300E spectrometer (mw frequency 9.42 GHz) using a standard rectangular Bruker EPR cavity (ER4102T) equipped with an Oxford helium cryostat (ESR900). The microwave frequency was measured using a Systron Donner frequency counter (6054D), and the magnetic field was measured using a Bruker gaussmeter (ER035M). A mw power of 2 mW, a modulation amplitude of 2 to 0.5 G, and a modulation frequency of 100kHz were used. The S-Band CW-EPR spectra were measured on a home-built CW and pulsed S-Band instrument using a Bruker (ER 4118S-MS-5W1) probehead and an Oxford cryostat (CF935). The Q-band EPR measurements were performed on a Bruker ELEXSYS E500 spectrometer equipped with a Bruker Q-band microwave bridge, a Bruker Q-band EPR resonator (ER5103QTH), and an Oxford

cryostat (CF935). All EPR-spectra were recorded at 120 K. The magnetic field was calibrated by a DPPH standard sample.

Pulsed EPR: The pulse EPR experiments (ESEEM and HYSCORE) were performed on a pulse X-Band Bruker Eleksys-580 spectrometer (microwave frequency 9.72GHz) and on a home-built pulse S-Band spectrometer (microwave frequency 3.5GHz).

All measurements were done in frozen solutions at a temperature of 20K and a repetition rate 1 kHz. The following pulse sequences were used:

Three-pulse ESEEM experiments were carried out using the pulse sequence $\pi/2-\tau-\pi/2-T-\pi/2$. At X-Band with microwave pulses of length $t_{\pi/2} = 16$ ns, a starting time $T_0 = 20$ ns, and a time increment $\Delta T = 8$ ns (512 intervals). To remove blind spots, time τ was varied in steps of $\Delta \tau = 16$ ns, with a starting value $\tau_0 = 120$ ns (25 time intervals). A four-step phase cycle was used in all experiments. The number of scans taken was 40 and 10 shots per point

HYSCORE experiments were carried out using the pulse sequence $\pi/2-\tau-\pi/2-t_1-\pi-t_2-\pi/2$. At X-Band, $t_{\pi/2} = 12$ ns, $t_{\pi} = 24$ ns, starting times $t_{01} = 36$ ns, and $t_{02} = 48$ ns and time increments $\Delta t_1 = 20$ ns, $\Delta t_2 = 20$ ns (data matrix 200×200) for 5 τ values (116, 136, 204, 288 and 336 ns) were used. An eight-step phase cycle was used in all experiments. Single scan was taken, accumulation time ~ 20 h.

A.6.3 Data manipulation and simulations

The ESEEM and HYSCORE time-domain data were baseline corrected using second- or third-order polynomial, apodized with a Hamming window, and zero filled. After 1D or 2D Fourier transformation the absolute - value spectra were calculated.

A home-written (in Matlab) simulation and fit program has been used for quantitative interpretation of the CW-EPR spectra [128]. The program *PESEEM_Selection* was used to calculate the orientation selection. The simulations of the HYSCORE spectra are performed in Matlab using simulation routine called *HY_IDEAL_F* for an $S=1/2$ system coupled to nucleus with an arbitrary nuclear spin I . Both programs have been written at the house [129]. The variable parameters are: the three principle values of the hyperfine tensor A_{xx} , A_{yy} , A_{zz} ; the largest component of the quadrupole tensor Q_{zz} and the asymmetry parameter η ; the six Euler angles α , β , γ and α' , β' , γ' , which describe the nuclear hyperfine and quadrupole tensor in respect to the principle axis system of the g-tensor.

B.6)

B.6.1 Sample preparation

The Cu_A containing soluble fragment of CcO (CcO_{II}) and the soluble cytochrome *c*₅₅₂ fragment both from *P. denitrificans* have been expressed in the heterologous *E. coli* system and purified as previously reported [26,71]. The soluble fragment of cytochrome *c*₁ was derived from the bc₁ complex, containing 125 amino acid residues expressed in *E. coli*. It carries negative surface charges like CcO_{II}, does therefore not interact with CcO_{II} and was used as a negative control in the experiments. Cytochrome *c* from horse heart (Sigma-Aldrich) was dissolved in 25 mM HEPES-KOH buffer at pH 7.0.

To fully oxidize cytochrome *c* and *c*₅₅₂ for EPR experiments, they were incubated with a tiny amount of cytochrome *c* oxidase from *P. denitrificans* for 30 min, and purified by gel filtration using a 5 mM HEPES-KOH buffer and 10% glycerol at pH 7.0. Cytochrome *c*, *c*₅₅₂ and *c*₁ concentrations were determined by recording redox difference spectra with extinction coefficients $\Delta\epsilon_{550-535} = 25.3$, $\Delta\epsilon_{550-540} = 19.4$, $\Delta\epsilon_{550-540} = 19.4 \text{ mM}^{-1}\text{cm}^{-1}$ for cytochrome *c*, *c*₅₅₂, *c*₁ respectively. The CcO_{II} concentration was determined by taking absorption spectra with an extinction coefficient $\epsilon_{480} = 3.0 \text{ mM}^{-1} \text{ cm}^{-1}$ [26]. The samples used for EPR measurements typically contained 100 μM fully oxidized CcO_{II} and varying ratios (50 μM 100 μM and 500 μM) of fully oxidized cytochromes in 5 mM HEPES –KOH and 10% glycerol at pH 7.0 buffer. The samples were transferred into standard quartz EPR tubes and subsequently frozen in liquid nitrogen.

B.6.2 Pulse EPR spectroscopy

The electron spin echo decay experiments were recorded at X-Band (microwave frequency 9.72GHz) using a Bruker Elexsys-580 spectrometer equipped with a Bruker MD5-W1 dielectric ring cavity and an Oxford CF935 helium flow cryostat with ITC-5025 temperature controller. A two-pulse $\pi/2$ - τ - π Hahn echo sequence was used to record both the field-swept EPR spectra and the echo decay traces. The lengths of the microwave $\pi/2$ and π pulses were 20 and 40 ns, respectively and the starting value for τ was 120 ns. The shortest τ -value of 120 ns is given by the dead time of the receiver channel after the short microwave pulse. All two-pulse echo decay experiments were performed on the maximum of the Cu_A signal, in a

temperature range of 10 to 25 K. The echo decay traces of the protein mixtures and CcO_{II} alone, were taken with exactly the same experimental settings and both traces were corrected for baseline artifacts by subtraction of off-resonance traces. All echo decay traces were normalized to 1 for the shortest τ value. The echo decay traces were reproducible to a very high accuracy (on the level of 5% for a certain sample) for the same protein concentrations and did not depend on the freezing procedure.

B.6.3 Analysis of experimental data

A home written MatLab simulation program based on the theory described in Chapter B.3 has been used to simulate the temperature dependence of the dipolar relaxation time traces for the protein-protein complex between Cu_A and cytochromes [135]. According to theory the terms B-F may also contribute to the dipolar splitting in case of spin systems with large g -anisotropies (e.g. paramagnetic transition metal ions). Despite the fact that these contributions are still rather small for Cu_A , they have been taken into account in the numerical simulations of our data.

The experimental dipolar relaxation traces at different temperatures were simultaneously fitted via a SIMPLEX algorithm. Fit parameters for a single binding geometry were: the distance R ; the polar angles of the dipolar vector with respect to the Cu_A g -tensor frame (θ_D, φ_D); the Euler angles (α, β, γ) of the cytochrome g -tensor with respect to the Cu_A g -tensor frame; the exchange coupling J ; an offset to account for unbound CcO_{II} . Additionally the literature values of the cytochrome T_1 relaxation times as a function of temperature were allowed to vary within a factors ± 2 to account for experimental errors.

References

A.7)

- [1] Prisner T., Rohrer M., MacMillan., *Annu. Rev. Phys. Chem.* **2001** 52, 279
- [2] Berliner L. J., Eaton S., Eaton G. Eds., *Biological Magnetic Resonance* Vol. 19 **2000** Kluwer Academic/Plenum Publishers, New York
- [3] Hoff A., *Advanced EPR: Applications in biology and biochemistry* **1989** Elsevier, Amsterdam
- [4] Sigel A., Sigel H., Eds., *Metal ions in biological systems* Vol. 39 **2002** Marcel Dekker, Ins., New York
- [5] Hill R., *Chem. Rev.* **1996** 96, 2757
- [6] Zannoni D., Eds., *Advances in Photosynthesis and Respiration* vol. 16 **2004** Springer
- [7] Moura J., Brondino C., Trincão J., Ramão M., *JBIC* **2004** 9, 791
- [8] Kisker C., Schindelin H., Baas D., Kroneck P., *FEMS Microbiol. Rev.* **1999** 22, 503
- [9] McEwan A., Ridge J., McDevit C., *Geomicrobiol. J.* **2002** 19, 3
- [10] Kisker C., Schindelin H., Rees D., *Annu. Rev. Biochem.* **1997** 66, 233
- [11] Bray R., *Rev. of Biophys.* **1988** 21, 299
- [12] Rajagopalan K. V., Johnson J., *JBC* **1992** 267, 10199
- [13] Rajagopalan K. V., *Adv. Enzym.* **1991** 64, 215
- [14] Okamoto K., Matsumoto K., Hille R., Eger B., Pai E., Nishino T., *PNAS* **2004** 101, 7931
- [15] Enroth C., Eger B., Okamoto K., Nishino T., Nishino T., Pai E., *PNAS* **2000** 97, 10723
- [16] Kisker C., Schindelin H., Pacheco A., Wehhi W., Garrett R., Rajagopalan K. V., Enemark J., Rees D., *Cell* **1997** 91, 973
- [17] McAlpine S., McEwan A., Shaw A., Bailey S., *JBIC* **1997** 2, 690
- [18] Bray R., Adams B., Smith A., Bennett B., Bailey S., *Biochem.* **2000** 39, 11258
- [19] Schneider F., Lwe J., Huber R., Schindelin H., Kisker C., Kniblein J., *JMB* **1996** 263, 53
- [20] McAlpine A. S., McEwan A. G., Bailey S., *JMB* **1998** 275, 613
- [21] Li H., Temple C., Rajagopalan K. V., Schindelin H., *JASC* **2000** 122, 7673
- [22] Schindelin H., Kisker C., Rajagopalan K. V., Rees D. C., *Science* **1996** 272, 1615
- [23] Dias J., Than M., Humm A., Huber R., Bourenkov G., Bartunik H., Bursakov S., Calvete J., Caldeira J., Carneiro C., Moura J., Moura I., Ramão M., *Structure* **1999** 7, 65
- [24] Boyington J., Gladyshev V., Shangulov S., Stadtman T., Sun P., *Science* **1997** 275,
- [25] Hedderich R., Klimmek O., Kröger A., Dirmeier R., Keller M., Stteter K., *FEMS Microbiol. Rev.* **1999** 22, 353
- [26] Schauder R., Kröger A., *Arch. Microbiol.* **1993** 159, 491
- [27] Fauque G., Klimmek O., Kröger A., *Meth. Enzym.* **1994** 243, 268
- [28] Klimmek O., Kröger A., Steudel R., Holdt G., *Arch. Microbiol.* **1991** 155, 177
- [29] Krafft T., Gross R., Kröger A., *Eur. J. Biochem.* **1995** 230, 601
- [30] Jankielewicz A., Schmitz R., Klimmek O., Kröger A., *Arch. Microbiol.* **1994** 162, 238

- [31] Klimmek O., Stein T., Pisa R., Simon J., Kröger A., *Eur. J. Biochem.* **1999** 263, 79
- [32] Klimmek O., Kreis V., Klein C., Simon J., Kröger A., *Eur. J. Biochem.* **1998** 253, 263
- [33] Lin Y., Dancea F., Löhr F., Klimmek O., Wienk H., Kröger A., Rüterjans H., *Biochem.* **2004** 43, 1418
- [34] Pilbrow J., *Transition ion electron paramagnetic resonance* **1990** Clarendon Press, Oxford
- [35] Abragam A., Bleaney B., *Electron paramagnetic resonance of transition ions* **1970** Oxford University Press, Oxford
- [36] Weil J. A., Bolton J. R., Wertz J.E., *Electron paramagnetic resonance* **1994** Wiley, New York
- [37] Deligiannakis., Louloudi M., Hadjiliadis N., *Coord. Chem. Rev.*, **2000** 204, 1
- [38] Mims W., Peisach., *Advanced EPR: Application to biology and biochemistry* **1989** Elsevier, Amsterdam
- [39] Mims W., Peisach., *Biological magnetic resonance* **1981** Plenum press, New York
- [40] Dikanov S., Shubin A., Kounosu A., Iwasaki T., Samoiloa R., *JBIC* **2004** 9, 753
- [41] Dikanov S., Davydov R., Bowman M., *JACS* **1998** 120, 6797
- [42] Dikanov S., Tyryshkin A., Hüttermann J., Bogumil R., Witzel H., *JACS* **1995** 117, 4976
- [43] Konovalova T., Dikanov S., Bowman M., Kispert L., *JPC* **2001** 105, 8361
- [44] Baute D., Arieli D., Neese F., Zimmermann H., Goldfarb D., *JPC* **2004** 126, 11733
- [45] Brecht M., van Gastel M., Buhrke T., Friedrich B., Lubitz W., *JACS* **2003** 125, 13075
- [46] Foester S., van Gastel M., Brecht M., Lubitz W., *JBIC* **2005** 10, 51
- [47] Ioanitescu I., Dewilde S., Kiger L., Marden M., Moens., Van Doorslaer S., *Biophys. J.* **2005** 89, 2628
- [48] Kababya S. Nelson J., Calle C., Neese F., Godfarb D., *JACS* **2006** ,
- [49] Maly Th., MacMillan F., Zwiker K., Kashani-Poor N., Brandt U., Prisner T., *Biochem.* **2004** 43, 3969
- [50] Grimaldi S., MacMillan F., Ostermann T., Ludwig B., Michel H., Prisner T., *Biochem.* **2001** 40, 1037
- [51] Kisselva N., Khvorova A., Westhof E., Schiemann O., *RNA* **2005** 11, 1
- [52] Abragam A., *The principles of nuclear magnetism* **1961** Oxford University Press, London
- [53] Atherton N., *Principles of electron spin resonance* **1993** Ellis Horwood Limited, Chicester
- [54] Poole P., Farach H., *The theory of magnetic resonance* **1972** Wiley-Interscience, New York
- [55] Schweiger A., Jeschke G., Ed. *Principes of pulse electron paramagnetic resonance* **2001** Oxford University Press, Oxford
- [56] Dikanov S., Tsvetkov Yu., *Electron spin echo envelope modulation ESEEM spectroscopy* **1992** CRC Press, Inc., Boca Raton
- [57] Kevan L., Bowman M., *Modern pulsed and continuous wave electron spin resonance* **1990** Wiley, New York
- [58] Mims W. B., *Phys. Rev. B* **1972** 5, 2409
- [59] Mims W., Peisach., *JCP* **1978** 69, 4921

- [60] Dikanov S., Shubin A., Parmon V., *JMR* **1981** 42, 474
- [61] Tyryshkin A., Dikanov S., Reijerse E., *JMR A* **1995** 116, 10
- [62] Tyryshkin A., Dikanov S., Reijerse E., *JMR A* **1995** 116, 10
- [63] Flanagan H., Singel D., *JCP* **1987** 87, 5606
- [64] Flanagan H., Singel D., *JCP* **1988** 89, 2585
- [65] Dikanov S., Tsvetkov Yu., Bowman M., Astashkin A., *Chem.Phys. Lett.* **1982** 90, 149
- [66] Ponti A., *JMR* **1997** 127, 87
- [67] Schweiger A., *Angew. Chem. Int. Ed.* **1991** 30, 265
- [68] Sebbach J., Hoffmann E., Schweiger A., *JMR A* **1995** 116, 221
- [69] Gemperle C., Aebli G., Schweiger A., Ernst R., *JMR A* **1995** 116, 221
- [70] Höfer P., Grupp A., Nebenführ H., Mehring M., *JMR* **1986** 132, 279
- [71] Höfer P., *JMR A* **1994** 111, 77
- [72] Shane J., Höfer P., Reijerse E., De Boer E., *JMR* **1992** 99, 596
- [73] Astashkin A., Raitsimring A., *JMR* **2001** 148, 379
- [74] Pöpl A., Böttcher R., Völkel G., *JMR A* **1996** 120, 214
- [75] Pöpl A., Böttcher R., *Chem. Phys.* **1997** 221, 53
- [76] Gutjar M., Böttcher R., Pöpl A., *Appl. Magn. Reson.* **2002** 122, 401
- [77] Pöpl A., Kevan L., *JPC* **1996** 100, 3387
- [78] Dikanov S., Bowman M., *JBIC* **1998** 3, 18
- [79] Shubin A., Dikanov S., *JMR* **2002** 155, 100
- [80] Dikanov S., Tyryshkin A., Bowman M., *JMR* **2000** 144, 228
- [81] Reijerse E., Tyryshkin A., Dikanov S., *JMR* **1998** 131, 295
- [82] Reijerse E., Dikanov S., *JCP* **1991** 95, 836
- [83] Reijerse E., Dikanov S., *JCP* **1991** 95, 836
- [84] Lai A., Flanagan H., Singel D., *JCP* **1988** 89, 7161
- [85] Carl P., Vaughan D., Goldfarb D., *JPC* **2002** 106, 5428
- [86] Gutjar M., Böttcher R., Pöpl A., *JPC B* **2002** 106, 1345
- [87] Gutjar M., Böttcher R., Pöpl A., *JPC B* **2003** ,
- [88] Deligiannakis Y., Astrakas L., Kordas G., Smith R., *Phys. Rev. B* **1998** 58, 11420
- [89] Astrakas L., Deligiannakis Y., Mitrikas G., Kordas G., *JCP* **1998** 109, 8612
- [90] Finazzo C., Harmer J., Bauer C., Jaun B., Duin E., Mahlert F., Goenrich M., Thauer R., Van Doorslaer S., Schweiger A., *JACS* **2003** 125, 4988
- [91] Bray R., Meriwether L., *Nature* **1966** 212, 467
- [92] Bennett B., Benson N., McEwan A., Bray R., *Eur. J. Biochem.* **1994** 225, 321
- [93] Bastian N., Kay C., Barber M., Rajagopalan K. V., *JBC* **1991** 266, 45
- [94] George G., Bray R., *Biochem. 27*, **1988** 3603
- [95] Wilson G., Greenwood R., Pilbrow J., Spence J., Wedd A., *JACS* **1991** 113, 6803
- [96] Balagopalakrishna C., Kimbrough J., Westmoreland T., *Inorg. Chem.* **1996** 35, 7758
- [97] Cramer S., Johnson J., Rajagopalan K.V., Sorrell T., *Biochem. Biophys.* **1979** 91, 434
- [98] Greenwood R., Wilson G., Pilbrow J., Wedd A., *JACS* **1993** 115, 5385
- [99] Hanson G., Brunette A., McDonell A., Murray K., Wedd A., *JACS* **1981** 103, 1953
- [100] Howes B., Bennett B., Koppenhöfer A., Lowe D., Bray R., *Biochem.* **1991** 30, 3969
- [101] Howes B., Bray R., Richards R., Turner N., Bennett B., Lowe D., *Biochem.* **1996** 35, 1432
- [102] Malthouse J., George G., Lowe D., Bray R., *Biochem. J.* **1981** 199, 629

- [103] Howes B., Pinhal N., Turner N., Bray R., Anger G., Ehrenberg A., Raynor J., Lowe D., *Biochem.* **1990** 29, 6120
- [104] Raitsimring A., Pacheco A., Enemark J., *JACS* **1998** 120, 11263
- [105] Astashkin A., Raitsimring A., Feng C., Johnson J., Rajagopalan K.V., Enemark J., *JACS* **2002** 124, 6109
- [106] Enemark J., Cooney J., Wang J., Holm R., *Chem. Rev.* **2004** 104, 1175
- [107] Enemark J., Young C., *Adv. Inorg. Chem.* **1993** 40, 1
- [108] Butler C., Charnoch., Bennet B., Lowe D., Thomson A., Berks B., Richardson D., *Biochem.* **1999** 38, 9000
- [109] Bray R., Adams B., Smith A., Richards R., Lowe D., Bailey S., *Biochem.* **2001** 40, 9810
- [110] George G., Hilton J., Temple C., Prince R., Rajagopalan K. V., *JACS* **1999** 121, 1256
- [111] George G., Hilton J., Rajagopalan K. V., *JACS* **1996** 118, 1113
- [112] Gladyshev V., Khangulov S., Axley M., Stadtman T., *PNAS* **1994** 91, 7708
- [113] Astashkin A., Raitsimring A., Feng C., Johnson J., Rajagopalan K., Enemark J., *Appl. Magn. Reson.* **2002** 22, 421
- [114] Astashkin A., Raitsimring A., Feng C., Johnson J., Rajagopalan K., Enemark J., *JACS* **2002** 124, 6109
- [115] Astashkin A., Pacheco A., Enemark J., *JACS* **1998** 120, 11263
- [116] Astashkin A., Mader M., Pacheco A., Enemark J., Raitsimring A., *JACS* **2000** 122, 5294
- [117] Pacheco A., Basu P., Borbat P., Raitsimring A., Enemark J., *Inorg. Chem.* **1996** 35, 7001
- [118] Astashkin A., Neese F., Raitsimring A., Cooney J., Bultman E., Enemark J., *JACS* **2005** 127, 16713
- [119] Astashkin A., Feng C., Raitsimring A., Enemark J., *JACS* **2005** 127, 502
- [120] Raitsimring A., Astashkin A., Feng C., Enemark J., Nelson K., Rajagopalan K., *JBIC* **2003** 8, 95
- [121] Barber M., Bray R., Lowe D., Coughlan M., *Biochem. J.* **1976** 153, 297
- [122] Gangeswaran R., Lowe D., Eady R., *Biochem. J.* **1993** 289, 335
- [123] Barber M., Siegel L., Schauer N., May H., Ferry J., *JBC* **1983** 258, 10839
- [124] Barber M., May H., Ferry J., *Biochem.* **1986** 25, 8150
- [125] Khangulov S., Gladyshev V., Dismukes G.C., Stadtman T., *Biochem.* **1998** 37, 3518
- [126] Cleland W., Barnhardt I., Yamanouchi K., Collison D., Mabbs F., Ortega R., Enemark J., *Inorg. Chem.* **1987** 26, 1017
- [127] Brauer G., Ed., *Handbook of preparative inorganic chemistry* Vol.1 1963, pp.358
- [128] Prisner T., Lyubenova S., Atabay Y., MacMillan F., Kröger A., Klimmek O., *JBIC* **2003** 8, 419
- [128] Prisner T., personal communications

B.7)

- [1] Mitchell P., *Nature* **1961** 191, 144
- [2] Trumpower B., Gennis R., *Annu. Rev. Biochem.* **1994** 63, 675
- [3] Schultz B., Chan S., *Annu. Rev. Biophys. Biomol. Struct.* **2001** 30, 23
- [4] Saraste M., *Science* **1999** 283, 1488
- [5] Nicholls D., Ferguson S., Eds. *Bioenergetics3* **2002** Academic press, London
- [6] Ostermeier C., Harrenga A., Ermler U., Michel H., *PNAS* **1997** 94, 10547
- [7] Iwata J., Ostermeier C., Ludwig B., Michel H., *Nature* **1995** 376, 660
- [8] Tsukihara T., Aoyama H., Yamashita E., Tomizaki T., et al., *Science* **1995** 269, 1069
- [9] Tsukihara T., Aoyama H., Yamashita E., Tomizaki T., et al., *Science* **1996** 272, 1136
- [10] Ludwig B., Bender E., Arnold S., Hüttermann M., Lee I., Kadenbach B., *Chembiochem* **2001** 2, 392
- [11] Michel H., Behr J., Harrenga A., Kannt A., *Annu. Rev. Biomol. Struct.* **1998** 27, 329
- [12] Richter O. M. H., Ludwig B., *Rev. Physiol. Biochem. Pharmacol.* **2003** 147, 47
- [13] Saraste M., *Q. Rev. Biophys.* **1990** 23, 331
- [14] Ferguson-Miller S. Babcock G. T., *Chem. Rev.* **1996** 96, 2889
- [15] Ramirez B., Malström B., Gray H. B., *PNAS* **1995** 92, 11949
- [16] Trumpower B., Gennis R., *Annu. Rev. Biochem.* **1994** 63, 675
- [17] Schultz B., Chan S., *Annu. Rev. Biophys. Biomol. Struct.* **2001** 30, 23
- [18] Capaldi R. A., *Annu. Rev. Biochem.* **1990** 59, 569
- [19] Babcock G. T., Wikström M., *Nature* **1992** 356, 301
- [20] Michel H., *Biochem.* **1999** 38, 15129
- [21] Michel H., *PNAS* **1998** 95, 12819
- [22] Abramson J., Svensson-ek M., Byrne B., Iwata S., *BBA* **2001** 1544, 1
- [23] Wikström M., *BBA* **2004** 1655, 241
- [24] Turba A. Jetzek M. Ludwig B., *Eur. J. Biochem.* **1995** 231, 259
- [25] Harrenga A., Reincke B., Rüterjans H., Ludwig B., Michel H., *JMB* **2000** 295, 667
- [26] Reincke B., Thöny-Meyer L., Dannehl C., Odenwald A., Aidim M., Witt H., Rüterjans H., Ludwig B., *BBA* **1999** 1411, 120
- [27] Reincke B., Pérez C., Pristovšek P., Lücke C., Ludwig C., Löhr F., Rogov V., Ludwig B., Rüterjans H., *Biochem.* **1999** 40, 12312
- [28] Ludwig B., Suba K., Cerletti N., *Eur. J. Biochem* **1983** 137, 597
- [29] Dickerson R. E., Takano T., Eisenberg D., Kalai O. B., Samson L., Cooper A., Margoliash E., *JBC* **1971** 246, 1511
- [30] Bushnell G. W., Louie G. V., Brayer G. D., *JMB* **1990** 214, 585
- [31] Hazzard J. T., Tollin G., *Arch. Biochem. Biophys.* **1991** 287, 1
- [32] Gray H. B., Winkler J. R., *Q. Rev. Biophys.* **2003** 36, 341
- [33] Gray H. B., Winkler J. R., *Annu. Rev.* **1996** 65, 537
- [34] Gray H. B., Winkler J. R., *PNAS* **2005** 102, 3534
- [35] McLendon., *Str. Bond.* **1991** 75, 159
- [36] McLendon., Hake. R., *Chem. Rev.* **1992** 92, 490
- [37] Axelrod H., Abresch E., Okamura M., yeh A., DouglasR., Feher G., *JMB* **2002** 319, 501
- [38] Kurisu G., Kusunoki M., Katoh., Yamazaki Y., Teshima K., Onda Y., Hase T., *Nature Str. Bio.* **2001** 8, 2001

- [39] Sevrioukova I., Li H., Zhang H., Peterson J., Poulos T., *PNAS* **1999** 96, 1863
- [40] Chen L., Durley B., Mathews S., Davidson V., *Science* **1994** 264, 86
- [41] Pelletier H., Kraut J., *Science* **1992** 258, 1748
- [42] Lange C., Hunte C., *PNAS* **2002** 99, 2800
- [43] Ubbink M., Ejdebäck M., Karlsson B., Bendall D., *Structure* **1998** 6, 323
- [44] Diaz-Moreno I., Diaz-Quintana., De la Rosa M., Ubbink M., *JBC* **2005** 280, 18908
- [45] Hunte C., Solmaz S., Lange C., *BBA* **2002** 1555, 21
- [46] Page C., Moser C., Chen X., Dutton L., *Nature* **1999** 402, 47
- [47] Prudêncio M., Ubbink M., *J. Mol. Rec.* **2004** 17, 524
- [48] Berry E., Trumpower B., *JBC* **1985** 260, 2458
- [49] Schägger H., *BBA* **2002** 1555, 154
- [50] Stroh A., Anderka O., Pfeiffer K., Yag T., Finel M., Ludwig B., Schägger H., *JBC* **2004** 279, 5000
- [51] Antalis T., Palmer G., *JBC* **1982** 257, 6194
- [52] Hill B. C., *JBC* **1994** 28, 2419
- [53] Hazzard J. T., Tollin G., *Arch. Biochem. Biophys.* **1991** 287, 1
- [54] Dethmers J.K., Ferguson-Miller S., Margoliash E., *JBC* **1979** 254, 11973
- [55] Ferguson-Miller S., Brautigan D. L., Margoliash E., *JBC* **1976** 251, 1104
- [56] Speck S. H., Dye D., Margoliash E., *PNAS* **1984** 81, 347
- [57] Michel B., Bossard R., *Biochem.* **1989** 28, 244
- [58] Lappalainen P., Watmough N. J., Greenwood C. Saraste M., *Biochemistry* **1995** 34, 5824
- [59] Zhen Y., Hoganson C. W., Babcock G. T., Ferguson-Miller S., *JBC* **1999** 274, 38032
- [60] Wang K., Zhen Y., Sadoski R., Grinell S., Geren L., Ferguson-Miller S., Durham B., Millett F., *JBC* **1999** 274, 38042
- [61] Bisson R., Steffens G. C. M., Capaldi R. A., Buse G., *FEBS Lett.* **1982** 144, 359
- [62] Witt H., Malatesa F., Nicoletti F., Brunori m., Ludwig B., *Eur. J. Biochem.* **1998** 251, 367
- [63] Witt H., Malatesa F., Nicoletti F., Brunori m., Ludwig B., *JBC* **1998** 273, 5132
- [64] Drosou V., Malatesa F., Ludwig B., *Eur. J. Biochem.* **2002** 269, 2980
- [65] Maneg O., Malatesa F., Ludwig B., Drosou V., *BBA* **2004** 1655, 247
- [66] Ferguson-Miller S., Brautigan D., Margoliash E., *JBC* **1978** 253, 149
- [67] Koppenol W., Margoliash E., *JBC* **1982** 257, 4426
- [68] Rieder R., Bosshard R., *JBC* **1980** 255, 4732
- [69] Capaldi R., Fuller S., Millett F., *FEBS Lett.* **1982** 138, 1
- [70] Drosou V., Reincke B., Scheider M., Ludwig B., *Bochem.* **2002** 41, 10629
- [71] Maneg O., Ludwig B., Malatesa F., *JBC* **2003** 278, 46734
- [72] Wienk H., Maneg O., Lücke C., Pristovšek P., Löhr F., Rüterjans H., Ludwig B., *Bochem.* **2003** 42, 6005
- [73] Roberts A. V., Pique M. F., *JBC* **1999** 274, 38051
- [74] Flöck D., Helms V., *Proteins* **2002** 47, 75
- [75] Bertini I., Cavallaro G., Rosato A., *JBIC* **2005** ,
- [76] Beinert H., *Eur. J. Biochem.* **1997** 245, 521
- [77] Kroneck P. M. H., Antholine W. E., Kastrau D. H. W., Buse G., Steffens G. C. M., Zumft W. G., *FEBS Letters* **1990** 268, 274
- [78] Antholine W. E., Kastrau D. H. W., Steffens G. C. M., Buse G., Zumft W. G., Kroneck P. M. H., *Eur. J. Biochem.* **1992** 209, 875

- [79] Farrar J. A., Neese F., Lappalainen P., Kroneck P. M. H., Saraste M., Zumft W. G., Thomson A. J., *JACS* **1996** 118, 11501
- [80] Neese F., Kappl R., Hüttermann J., Zumft W. G., Kroneck P. M. H., *JBIC* **1998** 3, 53
- [81] Neese F., Zumft W. G., Antholine W. E., Kroneck P. M. H., *JACS* **1996** 118, 8692
- [82] Kroneck P. M. H., Antholine W. E., Reister J., Zumft W. G., *FEBS Letters* **1988** 242, 70
- [83] Käss H. MacMillan F., Ludwig B., Prisner T. F., *JPC* **2000** 104, 5362
- [84] Farrar J. A., Lappalainen P., Zumft W. G., Saraste M., Thomson A. J., *Eur. J. Biochem.* **1995** 232, 294
- [85] Lappalainen P., Aasa R., Malmström., Saraste M., *JBC* **1993** 268, 26416
- [86] MacMillan F., Kannt A., Behr J., Prisner T. F., Michel H., *Biochem.* **1999** 38, 9179
- [87] Scholes C. P., Janakjraman R., Taylor H., *Biophys. J* **1984** 45, 1027
- [88] Stevens T. H., Brudvig G. W., Bocian D. F., Chan S. I., *PNAS* **1979** 76, 3320
- [89] Tweedle M. F., Wilson L. J., Babcock G. T., Palmer G., *JBC* **1978** 253, 8065
- [90] Poewrs L., Lauraeus M., Reddy K. S., Chance B., Wikström M., *BBA* **1994** 1183, 504
- [91] Fann Y. C., Ahmed I., Verkhovskaya J. S., Hoffman B. C., Wikström M., *Biochem.* **1995** 34, 10245
- [92] Walker F. A., *Coord. Chem. Rev.* **1999** 185-186, 471
- [93] Brautigan D. L., Feinberg B. A., Hoffman B. M., Margoliash E., Peisach J., Blumberg W. E., *JBC* **1977** 252, 574
- [94] Mailer C., Taylor C. P. S., *Can. J. Biochem.* **1972** 50, 1048
- [95] Gadsby P. M. A., Peterson J., Foote N., Greenwood C., Thomson A., *Biochem. J.* **1987** 246, 43
- [96] Lambeth D. O., Campbell K. L., Zand R., Palmer G., *JBC* **1973** 248, 8130
- [97] Poole P., Farach H., *Relaxation in magnetic resonance* **1971** Academic Press, New York
- [98] Milov A. D., Maryasov A. G., Tsvetkov Y. D., *Appl. Magn. Reson.* **1998** 15, 107
- [99] Milov A. D., Ponomarev A. B., Tsvetkov Y. D., *Chem. Phys. Lett.* **1984** 110, 67
- [100] Larsen R. G., Singel D. J., *J. Chem. Phys.* **1993** 98, 5134
- [101] Martin R., Pannier M., Diederich F., Gramlich V., Hubrich M., Spiess H., *Angew. Chem.* **1998** 110, 2994
- [102] Jeschke G., *Macromol. Rapid Commun.* **2002** 23, 227
- [103] Jeschke G., *ChemPhysChem.* **2002** 3, 927
- [104] Piton N., Schiemann O., Mu Y., Stock G., Prisner T. F., Engels J. W. *Nucleotides & Nucleic Acids* **2005** 24, 771
- [105] Bennati M., Robblee J. H., Mugnaini V., Stubbe J., Freed J. H., Borbat P. *JACS* **2005** 127, 15014
- [106] Schiemann O., Piton N., Mu Y., Stock G., Engels J. W., Prisner T. F. *JACS* **2004** 126, 5722
- [107] Bennati M., Weber A., Antonic J., Perlstein D. L., Robblee J., Stubbe J. *JACS* **2003** 125, 14988
- [108] Codd R., Astashkin A. V., Pacheco A., Raitsimring A. M., Enemark J. H., *JBIC* **2002** 7, 338
- [109] Elsaesser C., Brecht M., Bittl R., *JACS* **2002** 124, 12606
- [110] van Amsterdam I. M. C., Ubbink M., Canters G. W., Huber M. *Angew. Chem. Int. Ed.* **2003** 42, 62

- [111] Narr E., Godt A., Jeschke G *Angew. Chem. Int. Ed.* **2002** 41, 3907
- [112] Borbat P. P., Freed J. H., *Chem. Phys. Lett.* **1999** 313, 145
- [113] Freed J. H., *Annu. Rev. Phys. Chem.* **2000** 51, 655
- [114] Kevan L., Schwartz R., *Time domain electron spin resonance* **1979** Wiley-Interscience, New York
- [115] Salikhov K., Dzuba S., Raitsimring A., *JMR* **1981** 42, 255
- [116] Dzuba S., Raitsimring A., Tsvetkov Yu., *Chem.Phys.* **1979** 44, 357
- [117] Tsvetkov Yu., Dzuba S., *Appl. Magn. Reson.* **1990** 1, 179
- [118] Kulikov A., Likhtenstein., *Adv. Mol. Relax. Inter. Proc.* **1977** 10, 47
- [119] Kispert L., Bowman M., Norris J., Brown M., *JCP* **1982** 76, 26
- [120] Brudvig G., Blair D., Chan S., *JBC* **1984** 259, 11002
- [121] Goodman G., Leigh J., *Biochem.* **1985** 24, 2310
- [122] Ohnishi T., LoBrutto R., Salerno J., Bruckner R., Frey T., *JBC* **1982** 257, 14821
- [123] Mascarenhas R., Wei Y., Scholes C., King T., *JBC* **1983** 258, 5348
- [124] Hilczer W., Goslar J., Gramza M., Hoffmann S., Blicharski W., Osyczka A., Tyruna B., Froncisz W., *Chem. Phys. Lett.* **1995** 247, 601
- [125] Rakowsky M., More K., Kulikov A., Eaton G., Eaton S., *JACS* **1995** 117, 2049
- [126] Budker V., Du J., Seiter M., Eaton G., Eaton S., *Biophys. J.* **1995** 68, 2531
- [127] Rakowsky M., Zecevic A., Eaton G., Eaton S., *JMR* **1998** 131, 97
- [128] Seiter M., Budker, V., Du J., Eaton G., Eaton S., *Inorg. Chim. Acta* **1998** 273, 354
- [129] Zhou Y., Bowler B., Lynch K., Eaton G., Eaton S., *Biophys. J.* **2000** 79, 1039
- [130] Hirsh D., Beck W., Innes J., Brudvig G., *Biochem.* **1992** 31, 532
- [131] Hirsh D., Beck W., Lynch J., Que L., Brudvig G., *JACS* **1992** 114, 7475
- [132] Kulik L. V., Dzuba I. A., Grigoriev I. A., Tsvetkov Yu. D., *Chem. Phys. Lett.* **2001** 342, 315
- [133] Bloembergen N., Purcell E. M.; Pound R. V., *Phys. Rev.* **1948** 73, 679
- [134] Zhidomirov G., Salikhov K., *Sov. Phys. JETP* **1969** 29, 1037
- [135] Prisner T., personal communications

Acknowledgements

I would like to thank Prof. Dr. Thomas Prisner for providing me the opportunity to work in his group, besides his constant support and interest, suggestions and guidance. I am very grateful to him for his trust and for letting me try out my ideas. Also, for his patience and help in correcting my thesis.

This work is a result of teamwork so I wish to express my thanks to Prof. Dr. Bernd Ludwig and Khalid Siddiqui for many motivating discussions and for providing the cytochrome *c* and cytochrome *c* oxidase samples, without them this work would not be possible.

I would like to extend my thanks to Dr. Oliver Klimmek for providing me with the polysulfide reductase samples.

Special thanks to Dr. Olav Schiemann for his encouragement, advices and motivating discussions. He also helped me a lot correcting parts of this thesis.

My thanks to Dr. Thorsten Maly for many vivid discussions on any topic. Also, I extend my thanks to Dr. Stephane Grimaldi, Dr. Fraser MacMillan and Dr. Axel Weber for sharing their knowledge on pulsed spectroscopy experiments.

Very special thanks to Melanie Hertel and Marloes Penning de Vries who helped me to correct this thesis for language and technical errors on a short notice, of course *I* am responsible for any remaining errors.

I am very grateful to Jörg Fritscher and Sigrid Kämmerer for their patience and standing the mess I always manage to create in our office. I would like also specially to thank Jörg Fritscher for the German translation of my summary.

Thanks also to Bela Bode for lots of scientific discussions, small talks and computer related problems.

My sincere thanks to all my colleagues for their help, support, many discussions and advices. I wish to express my appreciation personally also to the ones not mention above: Dr. Marina Bennati, Adrian Cernescu, Dr. Vasyl Denysenkov, Dr. Burkhard Endeward, Natalie Kisseleva, Dominik Margraf, Hildegard Mathis, Astrid Noll, Dr. Jörn Plackmeyer, Stefanie Steinbrenner and Bernhard Thiem.

I thank also Dr. Lerner and Prof. Dr. Wagner, from our inorganic chemistry department, for the preparation of sodium sulfide for the isotope labeled experiments.

Finally, a warm thanks to Mel and Natalie for their encouragement, support as well as for the nice talks about anything and everything.

Curriculum Vitae

Personal Data

First Name: Sevdalina
Last Name: Lyubenova
Address: Bleichstr. 71
63065 Offenbach am Main
Germany
Date of birth: October 26th, 1973
Place of Birth: Veliko Tarnovo, Bulgaria
Family Status: Single

Education (School)

1980-1986: Primary School
“Vladimir Komarov”, Veliko Tarnovo
1986-1991: Secondary School of Mathematic and Natural Sciences
“Vasil Drumev”, Veliko Tarnovo

Education (University)

1991-1997: Sofia University “St. Kliment Ohridski”, Sofia, Bulgaria
Chemistry
1997: Diploma Thesis: “Chemical and Photochemical Properties of
Mixed-Ligand Dithiocarbamate Complexes of Cu(II)”
1997-2000: Bulgarian Academy of Science, Sofia, Bulgaria
Researcher in the group of Prof. N. D. Yordanov
Nov. 2000-2006: Johann Wolfgang Goethe University, Frankfurt am Main
Postgraduate student in the research group of Prof. T. F. Prisner

My academic teachers are: P. Bonchev, G. Lazarov, T. F. Prisner, T. Spasov, B. Toshev, N. D. Yordanov, B. Zeliaskova.